

Engineering Single Atom Catalysts to Tune Properties for Electrochemical Reduction and Evolution Reactions

Kakali Maiti, Sandip Maiti, Matthew T. Curnan, Hyung Jun Kim, and Jeong Woo Han*

Electrocatalysis is important to the conversion and storage of renewable energy resources, including fuel cells, water electrolyzers, and batteries. Engineering metal-based nano-architectures and their atomic-scale surfaces is a promising approach for designing electrocatalysts. Single metal atom interactions with substrates and reaction environments crucially modulate the surface electronic properties of active metal centers, yielding controllable scaling relationships and transitions between different reaction mechanisms that improve catalytic activity. Single-atom catalysts (SACs) allow activity and selectivity tuning while maintaining relatively consistent morphologies. SACs have well-defined configurations and active centers within homogeneous single-atom dispersions, producing exceptional selectivities, activities, and stabilities. Furthermore, SACs with high per-atom utilization efficiencies, well-controlled substrate compositions, and engineered surface structures develop single atom active sites for molecular reactions, enhancing mass activities. Recent developments in different metal-based SAC nanostructures are discussed to explain their remarkable bi-functional electrocatalytic activities and high mechanical flexibility, especially in the oxygen evolution reaction, oxygen reduction reaction, carbon dioxide reduction reaction, hydrogen evolution reaction, and in battery applications. Existing barriers to and future insights into improving SAC performance are addressed. This study develops practical and fundamental insights on single atom electrocatalysts directed towards tuning their electrocatalytic activities and enhancing their stabilities.

1. Introduction

Fuel cell and battery-based energy storage and conversion technologies strongly impact academic research and industrial initiatives.^[1–6] Currently, more focus is directed towards storage technologies involving electric vehicles and power stations,^[7–9] given their high efficiencies and low emissions. Hydrogen fuel cells, using renewable hydrogen gas for fuel and producing water as their sole byproduct, show significant potential as highly efficient devices for supplying clean

energy,^[10–12] especially for transportation. Fuel cell technology, which is projected to grow exponentially in the near future, has already entered global markets in the form of fuel cell electric vehicles (FCEVs),^[13–15] including the Hyundai Nexo and Toyota Mirai. With respect to other comparable vehicles, FCEVs are significantly advantaged relative to fuel storage cost, driving range, specific energy (W·h kg⁻¹ of cell), safety, and refueling time. Such improved attributes benefit FCEVs primarily in applications involving heavy trucks and long distance driving. Lithium battery electric vehicles (BEVs)^[8,16,17] also produce no direct emissions via transportation, positioning fuel cell energy technologies and BEVs as some of the best sustainable modes of transportation in the foreseeable future. Such energy technologies are strong prospective replacements for non-renewable fossil fuels, helping mitigate atmospheric pollution, climate change, and related environmental risks.

Catalysts are indispensable to chemical industries that necessitate environmentally safe power generation, for they facilitate chemical reactions such as carbon monoxide conversion into carbon dioxide during gaseous car exhaust treatment.

Catalysts increase the rates of chemical reactions, and are widely used in energy storage and conversion. They also influence emerging battery and fuel cell technologies, which are usually – thermally or electrically – energy-intensive.^[21–23] Thus, such technologies harness catalysis to reduce reaction temperatures, pressures, or electrochemical overpotentials. With regard to overcoming such technological limitations, single-atom catalysts (SACs) are highly promising, featuring active and isolated single metal atoms stabilized by supportive substrates or alloying.^[24–29] SACs are distinguished from nanoparticle (NP) catalysts through their lack of metal–metal bonds, usually yielding positively charged single metal atoms. Unique SAC geometric and electronic properties significantly alter reactant, intermediate, and product interactions, enhancing reaction activity to assist refined chemical manufacturing. Thus, SACs integrate benefits that include high catalytic activity, stability, selectivity, and reusability to sustainably synthesize fine chemicals.^[30–34]

Engineering supported NP surface areas and morphologies is extremely important to improve reaction activities and

K. Maiti, S. Maiti, M. T. Curnan, H. J. Kim, J. W. Han
Department of Chemical Engineering
Pohang University of Science and Technology (POSTECH)
Pohang, Gyeongbuk 37673, South Korea
E-mail: jwhan@postech.ac.kr

The ORCID identification number(s) for the author(s) of this article can be found under <https://doi.org/10.1002/aenm.202101670>.

DOI: 10.1002/aenm.202101670

selectivities,^[35,36] as most chemical transformations occur on NP surfaces. Given that reducing particle sizes increases available surface areas to produce more active sites, “single-atom” metal catalysts are the ultimate conclusion of size reduction.^[37–39] Such metals are no longer particles, but rather are individual atoms anchored to inexpensive supportive surfaces that are described by distinctive physics and chemistry. Given only environmentally exposed metal atoms react in chemical processes, greater proportions of smaller metal particles participate in catalytic reactions, compounding the cost efficiency of using inexpensive catalytic materials.^[40,41] At the extreme limit achieved by SACs, every single atom is chemically active, maximizing reactive and economic efficiencies. SACs demonstrate additional advantages over conventional catalytic materials, such as exposed single atom active sites with high surface energy that reduce associated chemical reaction activation barriers due to their undercoordinated environments.^[42] Also, reacting SACs observe quantum confinement effects, which impact energy level distributions and highest occupied versus lowest unoccupied molecular orbital (HOMO-LUMO) gaps.^[43] Strong metal-support SAC interfacial bonds additionally facilitate electrochemical charge transfer.^[44,45] Further, SACs can trap soluble electrochemical intermediates due to their high polarity, significantly reducing intermediate leaking between anodes and cathodes.^[46] These advantages highlight how SACs can be applied to advanced fuel cell and battery systems to simultaneously improve their energy densities and associated rates of reaction.

Strong electronic or covalent metal-support interactions thermodynamically stabilize SACs during reactions.^[47] Such interactions can be attributed to undercoordinated metal active sites, metal-support charge transfer, and quantum size effects impacting both HOMO-LUMO gaps and energy level discretization.^[48] SAC performance is largely determined by the former (HOMO-LUMO gaps) and latter (energy level discretization) attributes. Moreover, metallic agglomeration can be prevented by selecting electron rich elements for SACs, increasing their bonding strength with supportive substrates.^[49,50] Practically, SACs featuring no agglomeration would fully utilize metal atom surface area in reactions, which is particularly useful for catalysis involving noble metals such as Pd, Ir, Au, and Pt.^[47,48,50] Idealized isolation of these single metal atoms would additionally produce excellent model systems,^[51–54] which could be studied to better understand the sophisticated atomic-scale mechanisms undergirding heterogeneous catalysis.

Thus, selectively controlling SAC coordination environments and electronic states can help explain the structure-activity relationships of active sites and underlying reaction mechanisms, which is important to practically applying the electrocatalytic Oxygen Reduction Reaction (ORR),^[55,56] Oxygen Evolution Reaction (OER),^[57,58] Hydrogen Evolution Reaction (HER),^[59,60] and Carbon Dioxide Reduction Reaction (CO₂RR).^[61,62] While the development of metal-air battery cathodes and fuel cells is impeded by limitations from ORR kinetics, the sequential mechanisms inducing electron transfer via H atoms in rechargeable metal-air batteries and water splitting half-reactions necessitate corresponding improvement of OER rates. In addition, electrochemical water splitting directed towards molecular H₂ generation in HER is similarly kinetically restricted by currently

available catalysts. Resolving any or all of these limitations would help mitigate global renewable energy issues. Therefore, engineering atomically dispersed SAC active sites can most effectively accelerate OER, ORR, and HER reaction kinetics. In tandem with this predominant methodology, a complementary approach for optimizing metal air batteries exists – minimizing reaction overpotential to maximize catalytic efficiency. Moreover, applying CO₂RR can reduce CO₂ emissions and mitigate global energy concerns. SACs have demonstrated outstanding activity and selectivity during CO₂RR, namely when converting CO₂ into CO, formic acid, C₂ products, and other chemicals. SACs have also been implemented as Nitrogen Reduction Reaction (NRR) electrocatalysts^[63,64] for ammonia (NH₃) production and nitrogen (N₂) fixation. Further, thermally stable and active SACs have been synthesized at high temperatures via ultrafast, facile, and universal shockwave techniques.^[65,66] Such high temperature synthesis reduces activation energies for SAC dispersion via encouraging thermodynamically favorable defect-metal bonding and improving substrate stability, providing a new effective approach for SAC production. Further, a recently formed versatile strategy integrates differently composed single metal sites within one system to allow continuous and easy synthesis of complex compounds for various challenging reactions,^[67] constituting a breakthrough in technological progress involving SAC development.

In this review, we have closely discussed the most recent developments concerning SACs, focusing on their atomic coordination, electronic structure, and crucial impacts on energy storage and conversion technologies. These significant aspects of SACs are emphasized based on current literature, providing novel value to a broad readership seeking to contribute future research towards such topics. The underlying atomistic mechanisms responsible for SAC activity are also highlighted to encourage further exploration of SAC attributes, namely through using the latest theoretical and computational approaches. Such approaches consider surface science techniques, electronic spin moments, Frontier Orbitals (FOs), charge capacity, and hydrogen bonding to uniquely explain many unsolved problems entailed by SACs. Further, this review confirms that almost all noble metals, transition metals, and even a few rare earth metals can comprise SACs through discussed synthesis procedures, underscoring the successful formation of SACs across material compositions. This study details how composition impacts experimental characterization involving SAC bonding, charge transfer, and property tuning in a devoted section, improving such explanations via correlation with theoretical approaches. In a complementary context, this review also assesses the importance of different support nanoarchitectures for SACs, encompassing nanosheets, nanorods, hollow nanospheres, 1D/2D nanostructures, core-shell nanospheres and nanofibers, faceted nanoparticles, nanofoams, nanofibers-in-tubes, and other structures. How support morphology contributes to catalytic activity and stability enhancement was developed distinctly in this study, as particular emphasis was given to fuel cell, water electrolyzer, and battery applications when explaining this relationship. The breadth of applications described in this review – encompassing HER, CO₂RR, NRR, ORR, OER, Zn-air batteries (ZABs), and Li-batteries – and how SACs distinctly augment catalytic activity and

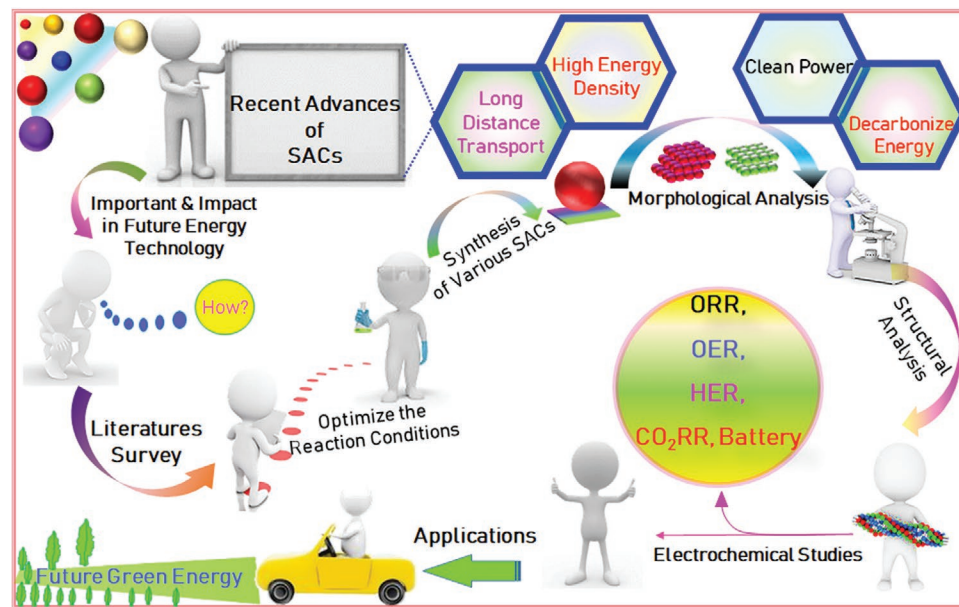


Figure 1. The design, construction, optimization, testing, and learning cycle for developing different metal based SACs. SACs are robustly tested through this heuristic already, though sequential iterations of screening, optimization, and engineering might follow in future electrocatalysis investigations.

durability in each of those reactions further distinguishes this study, importantly highlighting how SACs serve as an “all-in-one” approach in future energy harvesting technologies. Finally, existing challenges and future perspectives pertinent to SAC performance improvement are addressed. Overall, our study details how practical and fundamental experimental insights on SACs, accompanied by complementary theoretical analyses, help design effective nanostructures and enhance electrocatalytic performances significantly. How our review accomplishes this goal is outlined in the heuristic process schematically shown in **Figure 1**.

2. Guiding Experiment with Simulation: Coordination and Electronic Structure

Correlative *d*-band models, which were originally constructed to link CO-metal orbital overlap and coupling to corresponding CO adsorption energy contributions on extended metal surfaces, are frequently implemented to investigate oxide-supported metal NP catalyst reactivity.^[51,52] However, such models characterize Co-metal bonding over hybridized orbitals with integer, ionic formal charges.^[68–71] Such characterization does not treat SACs effectively, as isolated metal atoms are bonded to supports and frequently have non-zero partial charges.^[72,73] These partial charges evolve from the coordination of SACs forming ligand complexes in homogeneous solutions, given that SAC ligand modification can tune properties such as the effective charges of particular bonding sites. Through combined bonding site modulation and stabilized metal center undercoordination, SACs integrate the advantages of reaction selectivity and reactivity characteristic of homogenous and heterogeneous catalysis, respectively.^[74] By including or excluding different ligands over the stages of catalytic reactions, SACs can accommodate wide varieties of reactants, intermediates, and desorbed

products with fewer reaction rate limiting processes while stabilizing catalysts via anchoring them to – frequently metal oxide – supports. Despite possible SAC ligand bonding to metal oxide supports, homogeneous catalytic complexes with O²⁻ ligands are uncommon,^[75] while SAC-support chemical environments are difficult to characterize and engineer. Nevertheless, inexpensive metal oxides – which can synergistically contribute to strong catalytic performances – are frequently selected for SAC substrates. Therefore, further research aspiring to understand how SAC metal site coordination affects adsorption and catalytic activity is important in both theoretical and practical contexts. Pertinent SAC surface chemical properties, which have been characterized in previous literature,^[76] consist of *d*-band centers, *d*-band centers of mass, and *d*-band filling descriptors. All of these electronic structure characteristics correlate with CO adsorption energies on transition metal surfaces.^[52,77] However, such correlations are localized relative to *d*-band filling (composition) and atomic structure, while their character is determined by orbital theory. For metals with fully – or nearly fully – occupied valence *d*-shells, CO binding is generally determined by *d*→2*p** electronic transitions. In contrast, 5*s*→*d* electron donation more extensively contributes to metal-CO bonding when metal *d*-shells are partially empty.^[78] Metal atom *d*-state symmetry and *d*-band filling are also impacted by bonding with metal oxide supports, affecting CO adsorption energies based on site geometries, structures, and SAC/support compositions. The relationships between SACs and CO adsorption energies were broadly evaluated for single metal atoms (M₁ = Ni, Ag, Ir) on Fe₃O₄(001) surfaces via DFT calculations, comparing such energetics with those of CO adsorbed on M(111) surface top sites and metal oxide (MO) surface cation sites of studied favorable facets. Though metal adsorptive reactivity was overwhelmingly correlated with electronic structure, CO induced structural distortions and composition did impact corresponding adsorbate energies, especially when

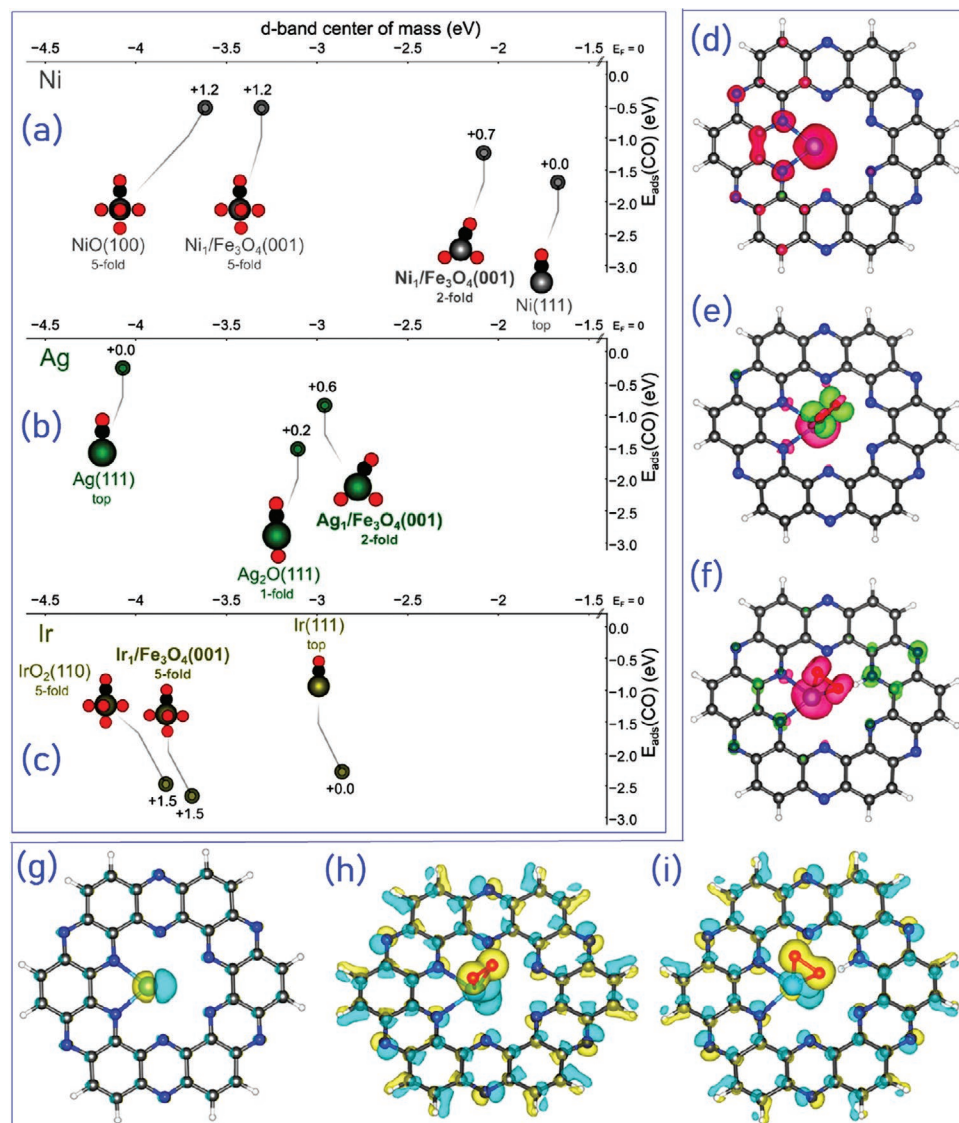


Figure 2. M₁/Fe₃O₄(001) SAC versus M(111) and MO_x surface CO adsorption energies plotted versus d-band centers of mass, illustrating first coordination spheres of configurations featuring oxygen (red) and carbon (black) with corresponding Bader charges. a) As Ni oxidation state improves, CO binding energy lowers and d-band centers of mass move from E_F . Fe₃O₄(001) embedded with five-fold Ni sites and NiO(100) have similar d-band centers of mass due to their analogous bonding. b) Oxidized Ag shift d-band centers of mass toward E_F , producing stronger CO binding energies versus corresponding metal surfaces. Ag atoms on top of Ag₂O(111) have strong E_{ads} for CO due to their linear CO–Ag–O_{surface} bonding. c) Five-fold coordinate Ir₁ on Fe₃O₄(001) have more favorable CO E_{ads} than Ir(111) due to strong cation oxidation, improving 5s→d electron transfer. Ir cations on five-fold sites act similarly to cations on IrO₂(110) surfaces. Adapted with permission from ref. [51]. Copyright 2021, AAAS publishing group. Spin densities of d) C₂N-Fe, e) C₂N-Fe-O₂, and f) C₂N-Fe-O₂-H with isosurface values of $5 \times 10^{-3} \text{ e } \text{\AA}^{-3}$, with respective electron density differences g-i) that have isosurface values of $0.1 \text{ e } \text{\AA}^{-3}$. Electron accumulation and depletion are respectively highlighted in yellow and blue. Adapted with permission.^[85] Copyright 2021, American Chemical Society.

SAC bonding was sparser. Consistent with Ir based results, Ni SACs supported on Fe₃O₄ in various coordination environments have Bader charges ranging between those of Ni(111) surfaces (+0.01 e) and five-fold coordinated Ni cations on NiO surfaces (+1.19 e). Ni cations in NiO and Ni₁ on Ni₁/Fe₃O₄(001) have respective stoichiometric and coordination anticipated oxidation states of 2+ and 1+, partially explaining this gradation in effective charge relative to Ni⁰ metal surfaces.

Figure 2a plots CO adsorption energy [$E_{\text{ads}}(\text{CO})$] versus d-band center of mass for Ni, Ag, and Ir SACs, revealing how

Ni d-band centers of mass shift away from the Fermi energy (E_F), while CO adsorbate bonding weakens with oxidation and metal active site Bader charges increase. Five-fold coordinated Fe substitution with Ni on an Fe₃O₄(001) surface mirrors NiO(100) with respect to charge and $E_{\text{ads}}(\text{CO})$ results, given their similar local coordination environments.^[79] Also, CO–Ni bonds on Ni₁/Fe₃O₄(001) are primarily electrostatic, as the large distances between E_F and their d-band centers of mass inhibit d→2p* electron donation.^[80] Figure 2b indicates CO binding on Ag₁/Fe₃O₄(001) is stronger than that of Ag(111), coinciding

with the transition from top (one-fold) to two-fold CO coordination and the shift of *d*-band center of mass towards E_F by 1.1 eV. Given the nearly filled *d*-shell of Ag, CO bonds are substantially strengthened by $d \rightarrow 2p^*$ electron donation to the extent of relatively weakening SAC-support binding, producing a distorted albeit more favorable CO geometry that is not observed in $\text{Ni}_1/\text{Fe}_3\text{O}_4(001)$ or on pristine $\text{Fe}_3\text{O}_4(001)$ surfaces. Structural relaxation balances the energetic contributions increasing $M_1\text{-CO}$ and decreasing $M_1\text{-O}$ bond strengths, thereby modifying adsorption energies beyond predictions made solely with adatom electronic structure. The coupled effects of local structural distortions and adsorption energy tuning have been broadly demonstrated in metals with nearly filled *d*-shells.^[51] However, the strong CO binding on Ir surfaces, shown in Figure 2c, was apparently determined by electrostatic bonding consistent with studied Ni based systems. While initially two-fold coordinate, Ir_1 bonds to subsurface O after binding to single CO molecules, forming a pseudo-square-planar Ir geometry.^[81] Upon binding Ir_1 to another CO, stable Ir square-planar coordination is fully realized through the formation of a $\text{Ir}(\text{CO})_2$ dicarbonyl doubly bonded to surface O.^[81] However, Ir substitutes a five-fold coordinated Fe cation from $\text{Fe}_3\text{O}_4(001)$ to stabilize $\text{Ir}_1/\text{Fe}_3\text{O}_4(001)$ at ≈ 450 K during temperature-programmed desorption, thus Ir_1 ultimately assumes a matching coordination environment. Given $5s \rightarrow d$ electron donation primarily contributes to Ir-CO bonding,^[78] high Ir atom oxidation states (Bader charge = 1.5 e) with five-fold coordination improve CO adsorption energies. Despite lessened $d \rightarrow 2p^*$ electron donation resulting from decreases in *d*-band center of mass, $\text{Ir}_1/\text{Fe}_3\text{O}_4(001)$ SAC-CO bond strength is counterbalanced by improved $5s\text{-}d$ orbital overlap. The Bader charges, *d*-band centers of mass, and $E_{\text{ads}}(\text{CO})$ of five-fold coordinated Ir in $\text{Ir}_1/\text{Fe}_3\text{O}_4(001)$ SACs mirror those of Ir cations forming rutile $\text{IrO}_2(110)$ surfaces, suggesting isolated and low concentration Ir can affordably replace expensive IrO_2 electrocatalysts in water-splitting reactions.

Successful SAC embedding into Fe_3O_4 substrates depends on oxygen affinity and preferential coordination with O, such that incorporation fails for group 11 metals that have lower oxidation states – such as Ag and Cu – when forming bulk metal oxides. In contrast, the stable four-fold coordination observed by group 10 metals, such as Pd and Pt, in their bulk oxides energetically improves their ability to adapt five-fold coordination environments.^[51] However, incorporation of four-fold coordinated SACs still fails when metal aggregation is sufficiently induced through processes such as sintering. Nevertheless, Ni and group 9 metals that can assume octahedral oxide coordination environments have higher oxygen affinities, which can avoid such aggregation to facilitate incorporation into lattices. This trade-off between oxygen affinity and O coordination during SAC selection for catalytic reactions can be characterized by the Sabatier principle, in which catalysts are optimized by being sufficiently reactive to adsorb or activate reactants, while also being sufficiently inert so as to not impede product desorption. Such catalyst optimization forms an effective “volcano plot” balancing adsorption and desorption kinetics, encouraging SACs as affordable alternatives to expensive Pt catalysts that typically optimize these kinetic considerations.

Metal–oxygen bonding modulates metal oxide electronic structure, such that observed two-fold coordination shifts

d-band centers of mass towards E_F to resultantly increase metal–CO bond strength.^[51] Under the approximation that relative adsorption energies can generally estimate activation barrier orders,^[82,83] metal adatoms were found to be more reactive than their pristine metal and oxide analogues, shifting relatively unreactive metals, and oxides closer to “volcano plot” optima. Consistent with computational screening literature,^[84] such improvements in metal adatom reactivity imply Pd, Rh, Ru, Ti, and Co SACs supported on Fe-O interfaces act like Pt SACs during CO oxidation. Such conclusions underscore the importance of fundamentally understanding two-fold coordination environment transformations during adsorption to supported SACs, in order to generalize the principles undergirding such transformations across broader ranges of oxide supports such as zeolites. While multiple metals demonstrated that transitioning to more coordinated environments was generally favorable, they also showed how low oxide coordination could be stabilized via ligand complex formation with reactants, OH, and water during reactions. Given stable SAC geometries can be formed and active site control can be realized in large-scale industrial settings, SACs can “heterogenize” homogenous catalysis in solution.

Zhong et al.^[85] completed DFT calculations modeling Fe SACs supported on C_2N ($\text{C}_2\text{N}\text{-Fe}$) for ORR applications to link electronic structure with catalytic activity. Changes in Fe and O_2 electronic spin moments during molecular-catalyst adsorption correlate with Fe- O_2 electron transfer, contributing to $\text{C}_2\text{N}\text{-Fe}$ ORR activity. This nearly linear, directly proportional relationship between activity and spin moment encourages the use of electronic spin moment as a catalytic descriptor for Fe based SACs. Figure 2d illustrates spin density analyses that confirm $\text{C}_2\text{N}\text{-Fe}$ spin is primarily found on not only Fe but also adjacent N and C atoms, while complementary densities featuring O_2 and $\text{O}_2\text{+H}$ adsorbates in Figures 2e,f depict spin as localized on Fe and O_2 . Differences in such electronic densities portrayed in Figures 2h,i verify strong electron transfer from Fe to O_2 , while Figure 2g demonstrates complementary weak electron transfer between N and Fe. Applying these results, ORR $\text{C}_2\text{N}\text{-Fe}$ is resolved to occur via three pathways, namely sequential O_2 dissociation, O_2 hydrogenation to OOH , and OOH hydrogenation to H_2O_2 . Each of these pathways has characteristic Fe spin moments, which can be linked to the Fe- O_2 electron transfer promoting $\text{C}_2\text{N}\text{-Fe}$ ORR catalytic activity. In conjunction with their correlations involving ORR rate-determining energy barriers and O_2 charge differences, electronic spin moments are validated as Fe SAC catalytic descriptors, aiding in the development of SAC design strategies.

Fu et al.^[86] evaluated Au SACs on C_3N supports (Au/ C_3N SACs) during CO oxidation via Frontier Orbitals (FOs), or the HOMO and LUMO closest to the Fermi level. Adsorbates only react with SAC active metal centers when both their orbitals observe similar energies and FO hybridization is significant, thus modulating SAC-support-adsorbate orbital overlap can control bond strength even when “volcano plot” adsorption energetics are unfavorable. Maximally localized Wannier functions (MLWFs)^[87] – in conjunction with ligand field theory – can resolve FO related properties controlling SAC binding and catalytic activity, such as frontier *d*-orbital spatial structure. For example, the C deficiency

and O modification of C₃N supports favor different CO-SAC bonding, namely respective d_{xz} or d_{z2} SAC FOs. Such surface composition controlled bonding can selectively forbid SAC reaction with different co-adsorbing O₂ and CO excited states, preventing particular (for example, Langmuir-Hinshelwood) mechanisms from occurring by controlling SAC-adsorbate wave function overlap. Generalization of these principles allows preclusion of particular adsorption, desorption, or co-adsorption events from occurring invariant of reaction conditions, relaxing the conventional restrictions of catalyst optimization via FO hybridization.

Zhao et al.^[88] studied Ni SACs adsorbed on N-doped graphene (Ni/NC SACs) during CO₂RR, applying ab initio molecular dynamics (AIMD) and “slow-growth” sampling to connect CO₂RR reaction barriers to active site excess charge capacity and H-intermediate bonding, resultantly resolving an explanation for SAC catalytic activity. High charge capacity, which defines the extent to which active sites can carry charge for electrochemical reactions, lowers associated reaction barriers. Relative to selectively engineering CO₂RR to occur over HER, H bonding stabilizes polar CO-based reaction intermediates via H transfer from H₂O. For CO₂RR, heterogeneous ligand complexes with only a few N ligands – such as those comprised of 1 N and 3 C – encompassing Ni SACs were the most active and selective studied. This was ultimately connected to the accumulation of excess charge on relatively isolated N or lower valence sites, which facilitated CO₂ binding with Ni SACs, charge transfer across their ligand complexes, and ultimately lower CO₂ adsorption barriers to those sites. Balancing decreases in CO₂ adsorption barriers to maintain CO₂RR activity, corresponding desorption barriers are lowered by modulating the extent to which CO-based intermediates are solvated with H₂O or stabilized via H bonding. Such an optimization is ultimately responsible for tuning CO₂RR activity.

By integrating considerations of orbital theory, adsorption kinetics optimization, and coordination complexes via DFT simulations as described in this section, the most stable configurations of supported SACs and the reaction mechanisms forming them are corroborated. This provides perspective on how to determine SAC atomic structure and bonding character in order to explain catalytic property variations on an atomic size scale. Overall, advanced theoretical characterization techniques enable us to articulate the important relationships between SAC electronic structure and related electrochemical properties. From such characterization, the fundamental mechanisms responsible for experimental outcomes can be distinctly justified, mitigating many unsolved issues and revealing further insights on how coordination and electronic structure impact SAC-support interactions across different nanostructures.

Nevertheless, understanding how nanostructures can be designed to tune SAC properties is highly important to optimizing relevant catalytic activities and stabilities. By elucidating which characteristics of experimental synthesis affect nanostructure morphology to influence SAC atomic interactions, SAC catalytic performance can be optimized from the macroscopic perspective of an experimentalist through a fundamental analysis proffered by atomic scale theories.

3. Engineering Morphology to Tune Catalytic Properties

Engineering the morphology of nanostructures undoubtedly contributes to enhancing catalytic activity and stability.^[89–99] Nanostructure control through synthesis methods motivates the design of different types^[100–105] of SAC support nanoarchitectures. Structural heterogeneity contributes greatly to enhancing catalyst activity and durability for possible applications in fuel cells, water electrolyzers, and battery applications.^[105] The ability to engineer active site availability, multifunctionality, electron transfer, conductivity, and catalyst durability justifies centralized consideration of nanostructure and morphology driven design, as SACs engineered under such considerations can be implemented in industrial applications to be discussed later.

3.1. Nanosheets and Nanorods

Gan et al.^[89] synthesized ultrathin 2D SACs – which were comprised of Fe single metal active sites, multiple (x) N ligands, and carbon nanosheet supports (Fe–N_x–Cns) – by first polymerizing dopamine (DA) hydrochloride on crystalline iron(III) chloride hexahydrate (FeCl₃·6H₂O) salt templates, then freeze-drying and pyrolyzing the resulting samples.^[90,91] As shown in Figure 3a, excessive layered 2D FeCl₃·6H₂O templates induced transverse DA polymer formation via intercalation reactions and chemical complexation. Simultaneously, Fe³⁺ oxidation promotes DA polymerization, such that maintaining coexisting Fe²⁺/Fe³⁺ ratios while inhibiting Fe⁰ formation ensures a complete reaction. Freeze-drying reduces surface tension to sublime the FeCl₃·6H₂O-DA solvent, yielding a hybridized inorganic–organic layered structure. Isolated Fe was deposited on N-doped carbon nanosheets during pyrolysis (700–900 °C, Ar atmosphere) to yield 2D Fe–N_x–Cns SACs, while residual Fe was removed via leaching with 0.05 M H₂SO₄. Fe–N_x–Cns prepared at different calcination temperatures (x in °C) are labelled Fe–N_x–Cns–x. As-prepared Fe–N_x–Cns have uniform 2D nanosheet-like structures according to Scanning Electron Microscopy (SEM) and Transmission Electron Microscopy (TEM) measurements (Figure 3b,c). Such structural characteristics were further confirmed by Atomic Force Microscopy (AFM), which measured the thicknesses of Fe–N_x–Cns–700, Fe–N_x–Cns–800, and Fe–N_x–Cns–900 substrates as 9.36, 3.59, and 7.46 nm, respectively. When compared to the arithmetic mean ($R_a = 0.18$ nm) and root-mean-squared (quadratic, $R_q = 0.15$ nm) deviation surface roughness measurements of Fe–N_x–Cns–800, the ultrathin 2D character of studied nanosheets was confirmed (Figure 3d,e). Consistent with SEM and TEM images, higher calcination temperatures further increased surfaces roughness, exposing abundant active sites for electrocatalytic reactions.^[90] Hierarchically layered porous nanosheets benefit Fe–N_x site formation,^[91] which are reactive sites for the dichloroethylene dechlorination reaction (DCEDR). Overall, the relatively isolated coordination of dispersed Fe active centers enables charge transfer across SAC complexes – namely from supports (Cns) to ligands (N_x) and active single Fe – to lower ethylene formation activation barriers and catalyze DCEDR.^[89] Thus, uniform and ultrathin 2D nanosheets with hierarchical pore structures

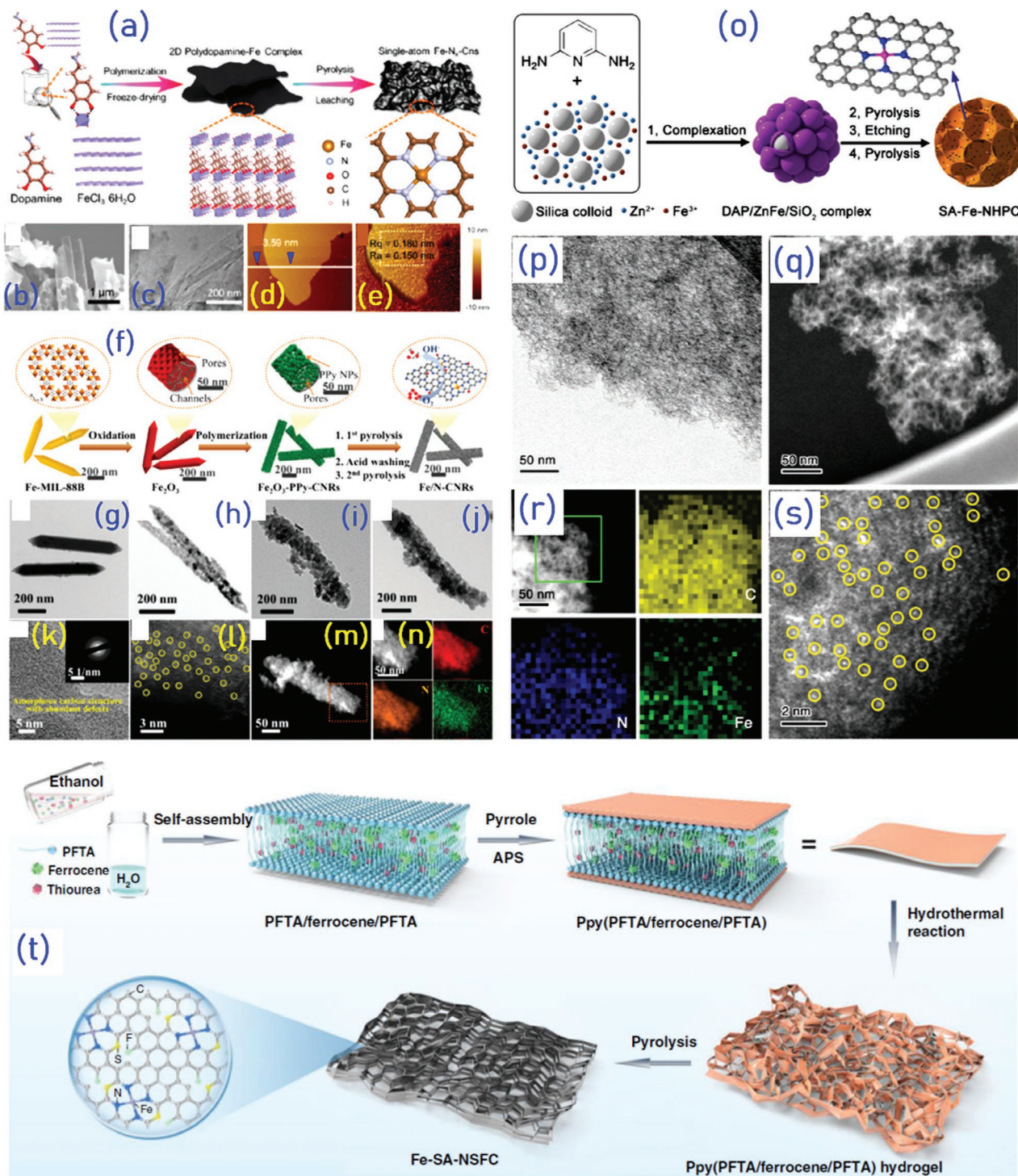


Figure 3. a) Heuristic depiction of $\text{Fe}-\text{N}_x-\text{C}_{\text{ns}}$ synthesis yielding experimentally resolved b) SEM, c) TEM, d) 2D AFM (accompanied by thickness profile), and e) 3D AFM images, the last of which features arithmetic and quadratic averaged surface roughness measures (R_a and R_q) of $\text{Fe}-\text{N}_x-\text{C}_{\text{ns}}$ at 800°C . Adapted with permission.^[89] Copyright 2020, American Chemical Society.

(f) Visual portrayal of a Fe/N -CNR synthesis process, with Fe, C, O, H, and N atoms colored in orange, grey, red, white, and blue, respectively.

(g-j) TEM imaging of **g**) Fe-MIL-88B , **h**) Fe_2O_3 , **i**) Fe_2O_3 -PPy-NRs, and **j**) Fe/N -CNRs.

(k) HRTEM imaging of Fe/N -CNRs, with an amorphous C substrate featuring abundant defects, and its SAED pattern (inset).

(l) AC HAADF-STEM imaging of Fe/N -CNRs (Fe atoms are bright dots within yellow circles).

(m) HAADF-STEM imaging and **n**) related C (red), N (orange), and Fe (green) elemental distributions for Fe/N -CNRs. Adapted with permission.^[92] Copyright 2020, Wiley-VCH Verlag GmbH & Co. KGaA, Weinheim

(o) Schematic depicting SA-Fe-NHPC synthesis.

(p) TEM, **(q)** HAADF-STEM, and **r**) elemental distributions of C (yellow), N (blue), and Fe (green) corresponding to **(q)** (green outline in **(r)**). **s**) Atomic resolution HAADF-STEM imaging of SA-Fe-NHP highlighting isolated Fe atoms (yellow circles). Adapted with permission.^[96] Copyright 2020, Wiley-VCH Verlag GmbH & Co. KGaA, Weinheim

(t) Heuristic illustrating Fe-SA-NSFC preparation. Adapted with permission.^[98] Copyright 2020, Springer Nature.

and rough surfaces can deliver abundant exposed active Fe–N_x sites for electrochemical catalytic processes, greatly enhancing catalytic activities and stabilities.

As displayed in Figure 3f, Gong et al.^[92] demonstrates 1D porous Fe and N-doped carbon nanorod (Fe/N-CNR) synthesis from rod-shaped Fe₂O₃ templates. Templates are first obtained by oxidizing Fe-MIL-88B in air.^[92] Note that Fe-MIL-88B, with its hexagonally-oriented Fe coordination centers and BDC (1,4-benzenedicarboxylate) ligands, is a 3D Fe₃O(BDC)₃X (X = OH, Cl) metal-organic framework (MOF) from the Material Institut Lavoisier (MIL).^[93,94] For Fe₂O₃ template synthesis, the Fe-MIL-88B precursor benefits from its 1D rod-like structure, both large and highly ordered porosity, and homogeneous Fe dispersion.^[95] Fe₂O₃ templates were then dispersed in ethanol solution and subsequently introduced to pyrrole monomers, which evenly fill Fe₂O₃ template pores via polymerization to yield 1D Fe₂O₃ nanorods. Such uniform pore distributions, maintaining the hierarchical structure of Fe-MIL-88B, developed interconnected channels through which electrochemical reactions could occur. After adding hydrochloric acid, Fe³⁺ ions were gradually released from nanorod surfaces and thereby dissolved. This formed partially undissolved Fe₂O₃ that yielded Fe₂O₃-embedded polypyrrole nanorods (Fe₂O₃-PPy-NRs), in conjunction with polymerization. As-prepared Fe₂O₃-PPy-NRs were pyrolyzed under high temperatures and an Ar atmosphere, then acid washed and pyrolyzed again to produce Fe/N-CNR catalysts. Fe/N-CNRs were also prepared without acid washing, while N-doped C nanorods (N-CNRs) were achieved by pyrolyzing Fe-free polypyrrole nanorods (PPy-NRs) yielded via Fe₂O₃-PPy-NR acid washing.^[92]

The morphology and microstructure of Fe/N-CNR catalysts were investigated with TEM, which indicated rod-like Fe-MIL-88B (Figure 3g) have uniform lengths ($\sim 1.2 \mu\text{m}$) and diameters ($\sim 170 \text{ nm}$). Figure 3h indicates Fe₂O₃ samples yielded from Fe-MIL-88B retained rod-like shapes, albeit with decreased lengths ($\sim 1 \mu\text{m}$) and diameters ($\sim 70 \text{ nm}$). Figure 3i portrays how polymerized Fe₂O₃-PPy-NRs adapt rod-like shapes from Fe₂O₃ templates, though with wider diameters ($\sim 160 \text{ nm}$) and rougher surfaces than structures preceding polymerization, and were enriched by uniformly distributed polypyrrole nanoparticles (PPy-NPs). Subsequent Fe/N-CNRs in Figure 3j had rod-like shapes comparable to those of Fe₂O₃-PPy-NR precursors (diameter $\approx 160 \text{ nm}$), but with no visible metal aggregation. By maintaining their rod-like shapes over synthesis, Fe/N-CNRs kept fast ORR diffusion kinetics ($\sim 4e^-$ transfer pathway, current density = 22.04 mA cm⁻² at 0.85 V, Tafel slope = 69.05 mV dec⁻¹) between active Fe centers and both electrochemical reactants and products. High-Resolution Transmission Electron Microscopy (HRTEM) imaging (Figure 3k) and Selected Area Diffraction (SAED) analysis (inset in Figure 3k) revealed Fe/N-CNRs consisted of amorphous C substrates with ample defects and no crystalline Fe compounds. Such carbonized substrates favored heteroatom doping and accommodated more defects, developing abundant Fe-N_x active sites. These defects not only tuned localized C electronic structure to incur O=O bond breaking, but also increased substrate specific surface area (666.7 m² g⁻¹) towards enhancing ORR performance (half-wave potential, $E_{1/2}$, equals 0.90 V). Such surface area improvements raised the density of active sites available to electrochemical reactions. Aberration-Corrected (AC) High-Angle Annular Dark-Field Scanning

Tunneling Electron Microscopy (HAADF-STEM) imaging in Figure 3l reveals numerous isolated Fe atoms (circled bright spots) on supported Fe/N-CNRs, while Figures 3m,n confirm the uniformity of N, C, and Fe distributed on the Fe/N-CNR substrate system via HAADF-STEM and matching elemental image mapping. Such evenly distributed Fe-N₄ ligand complexes, which served as SAC ligand complexes when supported on carbon nanorod (CNR) active sites, observed uneven charge distributions that facilitated e⁻ transfer and further improved ORR catalytic activity. Overall, previously described structural features encompassing rod-like 1D morphology, hierarchically assembled supportive CNR pores, high substrate surface area, and both uniformly dispersed Fe and N were responsible for the strong performance of Fe/N-CNR SACs.^[92] Thus, unique 1D rod-shaped Fe/N-CNRs exhibit hierarchical porous supports with large Brunauer–Emmett–Teller (BET) surface areas, formidable porosities, and efficient Fe/N doping. All of these properties favor the exposure of active sites and improvement of ORR mass transport capabilities. Furthermore, these nanorod architectures prevent pores from collapsing and prevent Fe aggregation, yielding atomic Fe-N₄ moieties during carbonization.

Chen et al.^[96] synthesized single atom Fe (catalysts) with N_x ligands on hierarchically porous carbon (SA-Fe-NHPC) using Zn-mediated (Zn/Fe = 8/1 molar ratio) pyrolysis (schematic in Figure 3o). Hierarchical MOFs readily formed between Zn/Fe ions and 6-diaminopyridine (DAP) molecules on silica supports, thus Zn sites efficiently separated adjacent Fe atoms. Thermal treatment of these MOFs (900 °C, 2 h, N₂ atmosphere) quickly vaporized Zn, leaving many carbonized micropores.^[97] The resulting sample was etched with HF solution (10 wt%) to remove both silica templates and less favorable Fe-composed structures, such as Fe-C based NPs. SA-Fe-NHPC electrocatalyst composites were finally yielded after performing pyrolysis again under the same conditions. DAP/ZnFe/SiO₂ layered composites with different Zn compositions (Zn/Fe molar ratios: 4/1, 6/1, 8/1, 10/1, and 12/1) were synthesized, then compared to Fe-composed NPs on hierarchically porous carbon decorated by N_x ligands (NP-Fe-NHPC, 3.85 wt% Fe) synthesized with neither Zn(NO₃)₂·6H₂O precursors for NHPCs nor silica templates for Fe-composed structures. Testing varied Zn compositions demonstrated interconnected MOF networks consistent with that of the primarily tested 8/1 case. Figures 3p,q evaluate SA-Fe-NHPC morphologies via TEM and HAADF-STEM, revealing abundant pores on SA-Fe-NHPCs sized consistently with their silica templates (average diameter $\approx 12 \text{ nm}$) and no NPs. Matching elemental mapping images in Figure 3r indicate homogeneous C, N, and Fe distributions over SA-Fe-NHPC surfaces. Figure 3s additionally confirms uniform Fe atom dispersion on carbon supports via AC HAADF-STEM. Combinations of Zn molar ratio testing and homogenous elemental distributions confirmed that Zn consistently prevented Fe-C NP formation, enabling silica templates to form hierarchical, interconnected networks of pores. Such networks improved the availability of Fe-N_x active sites and ligands to electrochemical reactants and products, facilitating high ORR activities evidenced by SA-Fe-NHPC and Pt/C half-wave potential comparisons ($E_{1/2} = 0.93$ vs 0.85 V).^[96] Thus, a novel strategy can be deduced from these results for improving the ORR activity of Fe-N-C electrocatalysts, namely constructing densely accessible Fe-N_x active

sites in SA-Fe-NHPCs. Benefiting from the high density and superb accessibility of $\text{Fe}-\text{N}_x$ active sites, SA-Fe-NHPC electrocatalysts demonstrably provide exceptional ORR performance.

Zhou et al.^[98] synthesized Fe single atom catalysts supported by N, S, and F co-doped porous graphitized carbon (Fe-SA-NSFC), using the process schematically depicted in Figure 3t that describes how multiple hierarchically stacked polymer layers can stabilize metal SACs during fabrication. Typical experimental setups first dissolved PFTA (perfluorotetradecanoic acid, 0.07 mmol), ferrocene (0.2 mmol), and thiourea (0.7 mmol) in ethanol (2 mL), then added water (10 mL) to induce lamellar PFTA bilayer self-assembly with respective hydrophilic and hydrophobic outer surfaces and interlayers.^[99] Resulting PFTA bilayers observed sheet-like morphologies up to $\approx 4 \mu\text{m}$ in effective diameter.^[99,100] Subsequently, ferrocene was confined to highly hydrophobic PFTA interlayers to yield layered PFTA/ferrocene/PFTA, then the PFTA outer surfaces were decorated with polypyrrole (PPy) via pyrrole (124 μL) addition to further stabilize ferrocene in the resulting PFTA/ferrocene/PFTA bilayers. After pyrrole was adsorbed via hydrogen bonding,^[100] the subsequently yielded PPy(PFTA/ferrocene/PFTA) was heated (150 °C, 8 h) to form a flattened hydrogel via PPy polymerization. Finally, samples were freeze-dried and pyrolyzed (1000 °C, 1 h, Ar atmosphere), then cooled to yield the final Fe-SA-NSFC products.^[98] Therefore, the engineering of hierarchical, porous, layered nanosheets and nanorods for previously described electrochemical applications can broadly be generalized to a common synthesis procedure, which sequentially consists of dissolving precursors in solution, inducing them to form hierarchical layers with added solvents, applying layered structures to polymerization, freeze-drying yielded solutions, and pyrolyzing final products. Thus, the nanosheet-like morphologies of Fe-SA-NSFCs provided coexisting micropores, mesopores, and macropores with high specific surface areas. These hierarchies of variably sized pores may be ascribed to improved porosity in N, S, and F co-doped Fe SACs, resulting in high catalytic activity and durability.

3.2. Janus Hollow Nanospheres

Chen et al.^[101] synthesized Janus-interfaced graphene hollow nanospheres (GHSs), with $\text{Ni}-\text{N}_4$ and $\text{Fe}-\text{N}_4$ ligand complexes distributed on different sides of the interface ($\text{Ni}-\text{N}_4/\text{GHSs}/\text{Fe}-\text{N}_4$). Separate $\text{Ni}-\text{N}_4/\text{GHS}$ (interior surface) and $\text{GHS}/\text{Fe}-\text{N}_4$ (exterior surface) samples were also synthesized as controls, as identifying individual $\text{Ni}-\text{N}_4$ and $\text{Fe}-\text{N}_4$ sites on $\text{Ni}-\text{N}_4/\text{GHSs}/\text{Fe}-\text{N}_4$ is difficult. Figure 4a depicts how $\text{Ni}-\text{N}_4/\text{GHSs}$ were formed through pyrolysis of core-shell $\text{SiO}_2@[Ni(CN)_4]_2@GO$ (graphene oxide) NPs and subsequent SiO_2 dissolution, while TEM images in Figure 4b depict the hollow spherical morphologies of as-prepared $\text{Ni}-\text{N}_4/\text{GHSs}$. AC STEM results from Figure 4c confirm Ni atoms are dispersed on the interior GHS surfaces of $\text{Ni}-\text{N}_4/\text{GHS}$ layered structures (highlighted in orange circles), as schematically illustrated in Figure 4d. Similarly albeit distinctly, $\text{SiO}_2@GO@FePc$ (Fe^{2+} phthalocyanine) pyrolysis and subsequent dissolution in SiO_2 (Figure 4e) yields layered GHSs/ $\text{Fe}-\text{N}_4$ samples with hollow nanospheres clearly defined via TEM imaging (Figure 4f). Uniform single Fe atom distributions on exterior GHSs/ $\text{Fe}-\text{N}_4$ surfaces can be analog-

ously confirmed in Figure 4g (bright dots highlighted with yellow circles) using AC Scanning Tunneling Microscopy (STEM) and heuristically portrayed in Figure 4h. In separate samples, adsorbed $\text{Fe}-\text{N}_4$ and $\text{Ni}-\text{N}_4$ ligand complexes respectively observe solely high ORR and OER activity. Nevertheless, when layered morphologies are engineered to yield $\text{Ni}-\text{N}_4/\text{GHSs}/\text{Fe}-\text{N}_4$ Janus interfaces, a bifunctional catalyst with high activities in both reactions is produced. Thus, the design of Janus nanospheres controls their efficacy as bifunctional catalysts with enhanced catalytic performance. Janus hollow nanospheres – which are formed from Ni and Fe SACs on their respective inner and outer surfaces – have high surface areas, and are capable of offering large effective active sites that favor electrolyte accessibility. Such coupled interfaces of Janus materials can provide general principles for electrocatalyst design, such as the incorporation of coupled components responsible for bifunctional properties and the manipulation of promoted catalytic properties via interfacial electronic coupling at Janus component interfaces. Evidently, constructing one Janus catalyst that improves both ORR and OER can simplify metal-air battery designs to reduce their complexity, namely compared with constructing two air-cathode compartments.

Zhou et al.^[102] designed Ni SACs anchored on N-doped hollow C nanospheres (Ni SACs/N-C) with large surface areas and strong electrical conductivities. Figure 4i portrays Ni SAC/NC synthesis, starting with dispersing spherical SiO_2 templates in mixed dopamine hydrochloride and $\text{Ni}(\text{acac})_2$ solution. Upon stirring, SiO_2 surfaces were coated with polydopamine and $\text{Ni}(\text{acac})_2$ to produce core-shell $\text{SiO}_2@\text{polydopamine}/\text{Ni}(\text{acac})_2$, which were then pyrolyzed under high temperatures and inert atmospheres to be subsequently etched with NaOH that removes SiO_2 templates. Careful control of Ni wt% and pyrolysis temperatures yields Ni SACs/N-C nanospheres. Figure 4j,k displays spherical AC STEM images of as-synthesized Ni atoms (bright dots) in Ni SACs/N-C that are highlighted by red circles, while Figure 4l confirms the uniform dispersion of C, N, and Ni over whole Ni SACs/N-C samples via elemental mapping with Energy Dispersive X-ray Spectroscopy (EDX). Isolating Ni by engineering SAC morphology both greatly improves NO adsorption energetic favorability to facilitate high electrocatalytic activity and forms a sensor for healthcare applications such as cancer detection.^[102] Thus, designed hollow carbon sphere Ni SACs/N-C catalysts provide large surface areas and good electrical conductivities, contributing to the superior electrocatalytic performance of Ni SACs/N-C by reducing their Gibbs free interfacial energies.

3.3. Porous Nanospheres and Nanofibers

Zhang et al.^[103] synthesized Co single atom, N and S co-doped hollow core-shell carbon sphere (CoSA/N,S-HCS) electrocatalysts. Figure 5a heuristically depicts how Co and dopamine (DA) monomer precursors polymerize on SiO_2 surfaces, producing core-shell $\text{SiO}_2@\text{polydopamine}$ nanospheres with chelated Co surface ions ($\text{SiO}_2@\text{PDA-Co}$). These nanospheres were pyrolyzed with S at 900 °C in an Ar atmosphere, then their SiO_2 cores were removed using NaOH etching to yield CoSA/N,S-HCS with controlled Co wt% and pyrolysis temperature. Samples not doped by S were synthesized as references (CoSA/N-HCS) with reduced catalytic activity, an observation

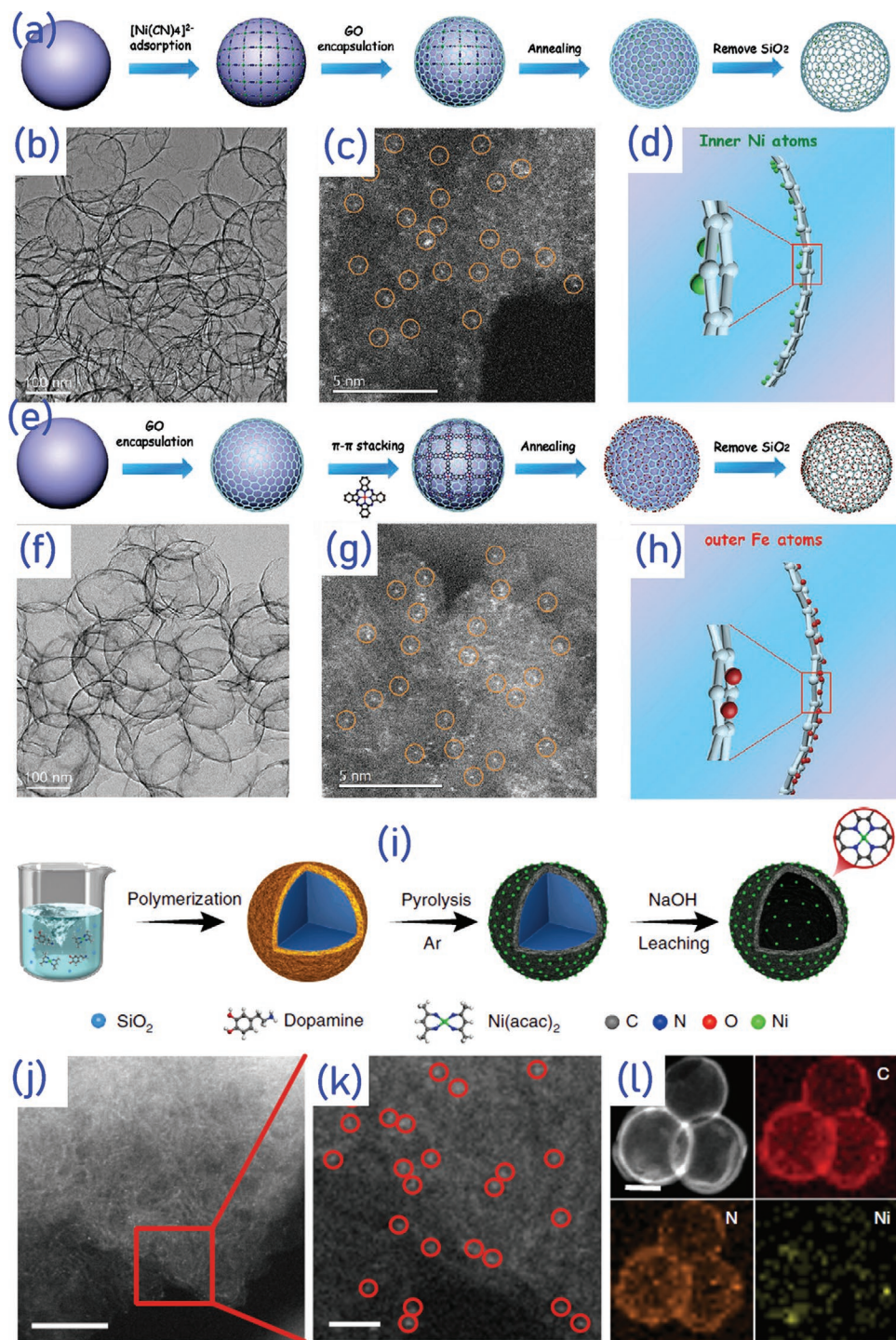


Figure 4. a) Heuristic depiction of Ni-N₄/GHS layer synthesis with matching b) TEM, c) AC STEM (isolated Ni in orange circles), and d) interior surface schematic images. e) Heuristic depiction of GHS/Fe-N₄ layer synthesis with matching f) TEM, g) AC STEM (isolated Fe in orange circles), and h) exterior surface schematic images. Adapted with permission.^[101] Copyright 2020, Wiley-VCH Verlag GmbH & Co. KGaA, Weinheim i) Heuristic depiction of Ni SAC/N-C synthesis and matching j,k) AC STEM images, highlighting single Ni atoms (red circles) and using scale bars of j) 5 and k) 1 nm. l) HAADF-STEM image (scale bar: 100 nm) and matching EDX elemental mappings of C (red), N (orange), and Ni (yellow). Adapted with permission.^[102] Copyright 2020, Springer Nature.

justified by comparative theoretical calculations confirming S improved electron transfer to Co 3d orbitals near their Fermi level. Figure 5b,c substantiate claims of uniform C, N, S, and

Co dispersions on HCS surfaces via EDX elemental mapping images, while Figure 5d more closely discerns Co SACs as well-dispersed bright dots (average size = 1.48 Å) via HAADF-STEM

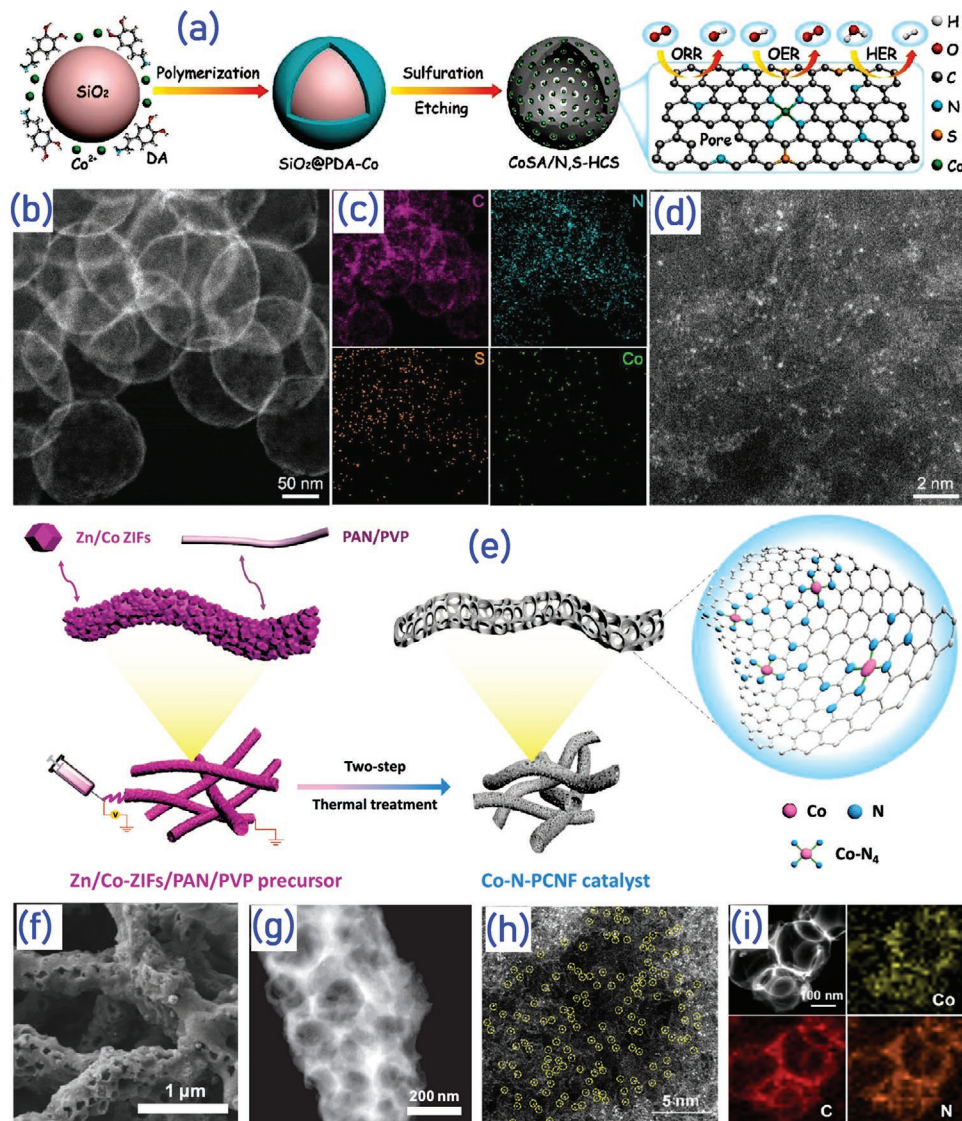


Figure 5. a) Heuristic depiction of CoSA/N,S-HCS synthesis with b) HAADF-STEM imaging (scale bar: 50 nm), and c) matching EDX elemental mappings for C (magenta), N (cyan), S (orange), and Co (green). d) HAADF-STEM imaging of CoSA/N,S-HCS (scale bar: 2 nm). Adapted with permission.^[103] Copyright 2020, Wiley-VCH Verlag GmbH & Co. KGaA, Weinheim. e) Heuristic depicting Co-N-PCNF catalyst preparation first through Zn/Co-ZIF co-electrospinning and polymerization, then by two-stage thermal activation. f) Secondary-electron (SE) and g) HAADF-STEM imaging of Co-N-PCNFs catalyst. Adapted with permission.^[105] Copyright 2020, Wiley-VCH Verlag GmbH & Co. KGaA, Weinheim. h) HAADF-STEM imaging of Co-N₄/C with single highlighted Co atoms (yellow circles), and matching i) EDX elemental mappings for C (red), N (orange), and Co (yellow). Adapted with permission.^[42] Copyright 2020, American Chemical Society.

with sub-angstrom resolution.^[104] The well-coordinated dispersions of related Co-N₄ ligand complexes over HCS supports, in conjunction with electron transfer from S, was ultimately attributed to the reduction in simulated O^{*}, OH^{*}, and OOH^{*} reaction intermediate activation barriers responsible for the trifunctional efficiency of CoSA/N,S-HCS catalysts over OER, ORR, and HER. Thus, hollow porous carbon spheres of CoSA/N,S-HCS provided large specific surface areas with high porosity to further expose abundant active sites and facilitate efficient mass transport. Further, ring-like patterns within graphitized carbon shells were beneficial to promoting conductivity and corrosion resistance. In addition, hollow carbon spheres with strong chemical stability and high conductivity

can effectively serve as excellent supports, which anchor fully dispersed SACs with tailored coordination environments. Further, different SACs – such as Fe, Ni, Cu, and Mn – or combinations of them with different dopants, including B and P, were synthesized using similar synthetic routes for various applications.

He et al.^[105] synthesized porous carbon nano-fiber based Co (Co-N-PCNF) catalysts, which consist of N-coordinated Co active sites wrapped in carbon fibers with hierarchically porous supports, through the electrospinning procedure depicted in Figure 5e. Zn and Co co-doped Zeolitic Imidazolate Framework (Zn/Co-ZIF) nanocrystals, accompanied by polyacrylonitrile (PAN) and poly(vinylpyrrolidone) (PVP) polymer precursors,

were first electrospun into Zn/Co-ZIFs/PAN/PVP fibers with lengths of $\approx 100\text{-}6$ m, then subsequently pyrolyzed in two stages to yield Co-N-PCNF SACs. During pyrolytic thermal activation, PVP is sacrificed to form pores, providing more sites for under-coordinated N to anchor Co. Increasing PVP/PAN composition improves fiber decomposition during pyrolysis, shortening fibers, or even inducing the collapse of their hierarchical morphologies. Thus, sufficient – but not excessive – pore formation from introducing PVP improves SAC durability by enabling Co-N₄ ligand complex anchoring, forming a trade-off between active site stability and availability. Similarly, Zn/Co ratios in ZIFs affect fiber morphologies due to the relatively low boiling point of Zn (907 °C), as Zn evaporation throughout pyrolysis produces hollow nanofibers. Upon sufficient Zn evaporation, excessive Co dopant proportions induce SAC agglomeration, yielding metallic Co clusters. Such clusters catalyze the excessive transformation of carbon fibers into graphite, destroying hierarchical fiber morphologies. Nevertheless, moderately graphitic N dopants linking Co SACs to carbon nano-fibers (CNFs) promoted charge transfer and lowered OOH* reaction intermediate adsorption energetics, thus partial graphitization adjacent to ligand complexes was responsible for increases in ORR catalytic activity. Therefore, to achieve active Co-N-PCNF catalysts with the hierarchical, interconnected 3D porous networks shown in Figure 5f, PVP/PAN and Zn/Co ratios must be optimized. Further, HAADF-STEM images in Figure 5g depict the porous, interconnected networks found inside each Co-N-PCNF catalyst fiber, which are adapted from Zn/Co-ZIF precursors directly rather than amorphous carbonized sources without hierarchical morphologies. Given thermal treatment does not significantly change morphology and such networks – with multimodal pore size distributions – facilitate electrochemical reactant and product mass transfer, the multifunctional optimization of ORR reactivity with catalyst stability and durability also constrains precursor origin. Here, distinct porous nano-fibers (NFs) and hierarchical morphologies significantly enhance electrode performance, namely by exposing active sites and readily inducing electronic conductivity by facilitating reactant mass transport. Intrinsic activity enhancement is ascribed to the additional graphitic N dopants adjacent the CoN₄ moieties. The more graphitized carbon catalyst support matrix advantageously increases the corrosion resistance of carbon, thus boosting durability of the catalyst. Hence, improvements in catalytic activities result from advanced design of the electrode with tailored macro, meso-, and microporosity, which maximize the effective pore densities and promote charge and mass transport. The CNF nanostructure achieved from this synthetic method is primarily responsible for achieving more macroporosity in the designed catalyst layers. Thus, thermal annealing can create CNFs with increasingly uniform dispersions of macroporous carbon nanostructures to diminish agglomeration of the NPs, while also maintaining adequate microporosity in individual NFs for hosting CoN₄ active sites. Therefore, highly porous and hierarchical carbon nanostructures remarkably boost electrode performance via exposing more available active sites. This enables ligand coverage uniformly around catalysts, which greatly facilitates electron, proton, and mass transport. Besides, primary macropores in individual fibers guide reactants to active sites, while com-

plementary secondary micrometer-scale pores – which exist between conjoined fiber backbones – enable gaseous molecules to diffuse through catalyst layers. Such diffusion results from gas flows inducing large pressure drops, forming networks of pathways for electron transfer.

Further, such distributional uniformity is also confirmed for Co-N₄ complexes over HCS surfaces with no S during ORR in Wu et al.^[42] Figure 5h applies AC HAADF-STEM to depict Co distributional uniformity per SAC (yellow circles) over an individual HCS, while Figure 5i uses EDX to highlight relatively uniform Co, C, and N distributions over larger structures consisting of multiple HCSs. Therefore, single Co atom confinement within N-doped hollow carbon spheres supporting Co-N₄/C catalysts can efficiently promote a four-electron ORR, namely with an onset potential of 0.68 V (vs RHE) under neutral conditions.

3.4. Isolating SACs: Oxygen Vacancies and Clustering

Yin et al.^[106] synthesized Ir-NiCo₂O₄ nanosheets (NSs), reviewing the chemical environments of their Ir-O_x ligand complex bonds. Figure 6a visualizes oxygen vacancy (V_O) coupled spinel structures simulated using DFT in past literature, which connected surface V_O formation to catalytic activity via electron delocalization of O 2p orbitals neighboring vacancies.^[107] HAADF-STEM shown in Figure 6b experimentally confirmed the Ir-NiCo₂O₄ NS structure, resolving NiCo₂O₄ substrate unit cells along the (111) plane. Figure 6c employs AC HAADF-STEM to directly discern Ir distributions as bright dots (yellow circles), verifying the uniform isolation of Ir SACs in studied Ir-NiCo₂O₄ NS samples. Thus, developed Ir-NiCo₂O₄ NSs with highly porous ultrathin morphologies favor exposed high surface areas and defects to couple with Ir SACs. Surface-exposed Ir SACs coupled with V_O show improved OER activity and stability in acidic media. Atomic Ir sites substantially elevate the electronic activity of less coordinated Co sites near V_O, which strongly facilitate surface electronic exchange-and-transfer capabilities. Through this trend, preferred H₂O activation and stabilized *O are attained at competitively low overpotentials. Such an achievement is generally key to optimized OER performance enhancement. Density Functional Theory (DFT) calculations reveal^[106] that such excellent OER performance arises from the high activities of electron exchange-and-transfer via atomic Ir anchoring on lesser coordinated Co sites near V_O. Such sites possess lower valence states, allowing efficient electron transfer in conjunction with hybridized ligand complex orbital overlap at the Fermi level. In particular, anchored Ir-O_x sites prevent variation in Co valence states. Meanwhile, Ir-O_x sites also redistribute bonded O and H species to reduce Ir SAC deactivation, namely by over-binding O and H species on Co sites. This strategy provided a promising way to prepare 2D metal porous NSs using unsaturated metallic surfaces, which greatly enhanced the intrinsic activity/selectivity of Ir SACs.

Li et al.^[108] synthesized Ir single atoms on nitrogen-doped carbon (Ir₁/CN) as an efficient catalyst using a general host-guest strategy. Via HAADF-STEM images, Figure 6d illustrates that yielded substrate CN morphologies were characteristically concave rhombododecahedrons with no Ir NP clusters.

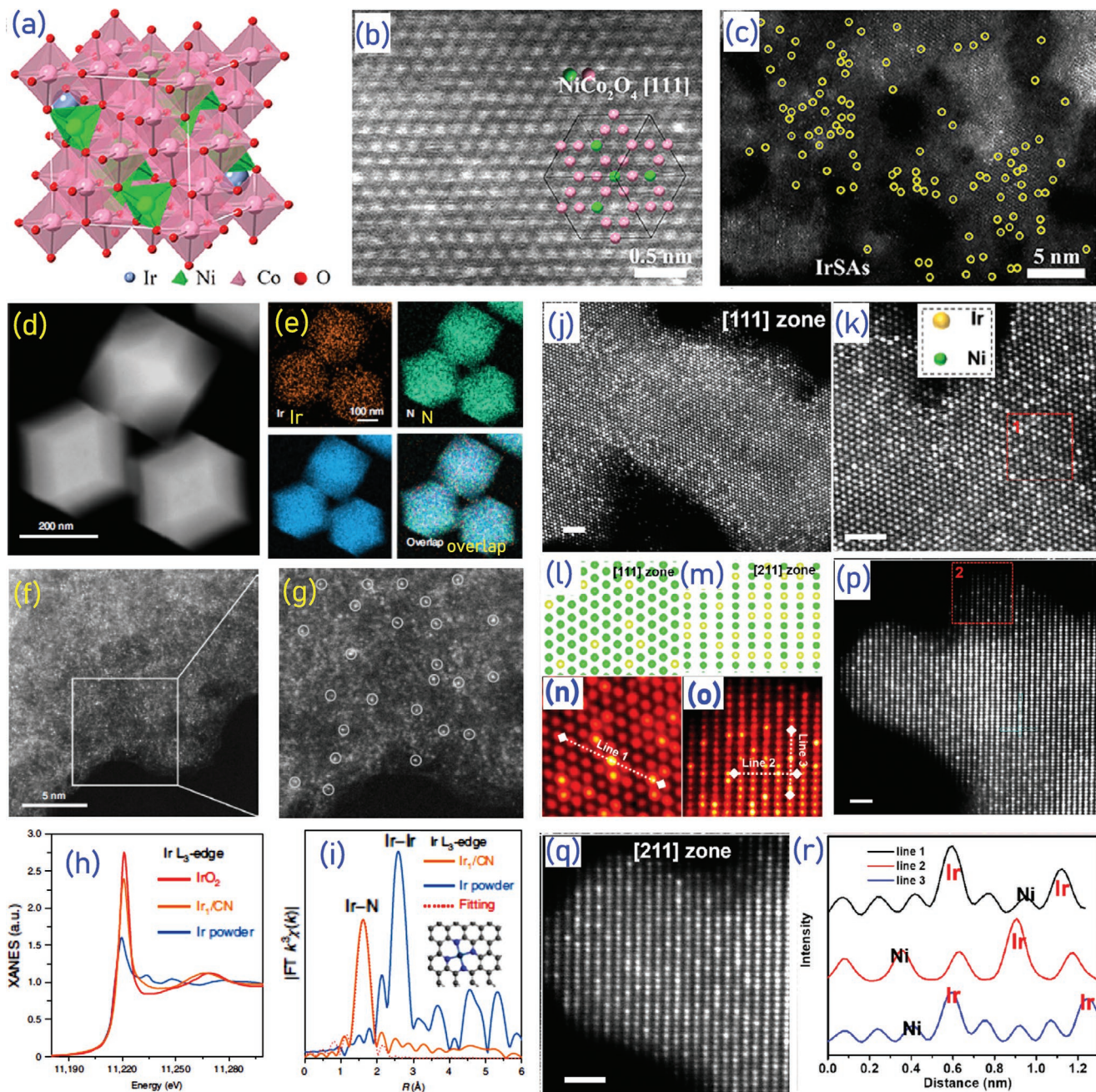


Figure 6. a) Visualized simulated Ir–NiCo₂O₄ NS with matching b) smaller scale HAADF-STEM image, corresponding NiCo₂O₄ unit cell along [111] (inset), and c) larger scale HAADF-STEM image highlighting Ir-SAs (yellow circles). Adapted with permission.^[106] Copyright 2020, American Chemical Society. d) HAADF-STEM imaging and e) EDX elemental mapping of an Ir₁/CN rhombododecahedron, suggesting Ir, N, and C are homogeneously distributed across Ir₁/CN surfaces. f,g) High-resolution and enlarged HAADF-STEM images of Ir₁/CN highlighting dispersed Ir positions (white circles). h) XANES and i) FT-EXAFS spectra of Ir₁/CN, Ir powder, and IrO₂ at the Ir L₃-edge, with radial distribution functions (*R*) indicating Ir–Ir and Ir–N bond distances for the schematic Ir₁/CN model (inset) visualizing Ir (turquoise), C (grey), and N (blue). Adapted with permission.^[108] Copyright 2020, Springer Nature. Representative atomic-scale STEM imaging along j,k) [111] and p,q) [211] zone axes, with respective [111] and [211] l,m) atomic models and n,o) atomic line profiles highlighting Ir with bright contrast from sampled image sections (respective red outlines in (k) and (p)). r) HAADF intensity analysis of labeled lines in atomic profiles from (n) and (o). All scale bars: 1 nm. Adapted with permission.^[110] Copyright 2020, American Chemical Society.

Figure 6e demonstrates matching EDX elemental mappings manifest uniform Ir, N, and C distributions over CN substrates, while corresponding high-resolution HAADF-STEM Ir₁/CN images in Figure 6f,g depict Ir SACs as bright dots highlighted with white circles. Ir₁/CN X-ray Adsorption Near Edge Structure

(XANES) spectra in Figure 6h produce their first high intensity Ir L₃-edge adsorption peaks between those of Ir powder and IrO₂ references. Thus, Ir₁/CN (Ir 4f) peak positions shift towards binding energies higher than those of Ir/C, but between those of Ir⁰ and Ir⁴⁺. The area integrated underneath the first fitted

peak of Ir₁/CN resolves an average Ir oxidation state of 2.42, consistent with past work.^[109] Figure 6i depicts Extended X-ray Absorption Fine Structure (EXAFS) analysis to further validate Ir SAC dispersion uniformity over Ir₁/CN. Corresponding Fourier-transformed EXAFS (FT-EXAFS) analysis resolves a notable peak (\approx 1.6 Å) correlated with Ir–N scattering paths. However, Ir–Ir bond peaks (\approx 2.6 Å) characteristic of Ir foil were not detected in Ir₁/CN, validating the isolation of Ir SACs in Ir₁/CN. Least-squares FT-EXAFS fits (Figure 6i) calculate structural parameters for Ir in Ir₁/CN that infer four-fold Ir–N ligand complex coordination. Here, a general host–guest strategy is developed to fabricate various metal SACs on N-doped carbon (Ir₁/CN). Catalytic activity was greatly influenced by attributes of the nanostructures, control of their shapes, exposed facets, and modification of their electronic structures with doping elements. DFT reveals Ir₁/CN properties^[108] stem from the spatial isolation of Ir sites, as well as the support-modified electronic structures of Ir SACs relative to those of conventional nanoparticle catalysts.

Wang et al.^[110] synthesized NiO supports with highly concentrated (\approx 18 wt%) Ir SACs to be applied to OER. Figure 6j,k,n respectively depict STEM images and atomic line profiles of Ir-NiO projected along the [111] zone axis, revealing Ir SACs directly overlap with Ni columns and thus occupy Ni sites in the outermost Ni surface planes of NiO orthogonal to [111]. Such Ir substitution of Ni is correspondingly illustrated via the atomic model illustrated in Figure 6l. Additional STEM images and atomic line profiles in Figure 6o–q depict a matching [211] zone projection of Ir-NiO, once again indicating Ir atomic coincidence with Ni atoms that develops the atomic model shown in Figure 6m. Figure 6r shows the HAADF intensities of the atomic line profiles resolved in Figure 6n,o, which measure Ir atomic contrast brightness with peak intensities over different zone axis conditions. The positions of Ir and Ni along lines 1–3 in Figure 6n,o are identified over the outermost Ni planes of NiO to yield correspondingly labeled peaks. Across all of these tests, Ir loadings between 2–11 wt% yielded similar structures, indicating the generality of the conclusions derived above. Thus, a facile approach was adopted here to synthesize single Ir atom catalysts with unprecedented high Ir atom loadings of up to \approx 18 wt% on NiO nanosheets (NSs). Their constituent NiO NSs are ultrathin and stacked vertically to form macroporous morphologies. All Ir single atoms likely stay on the outermost NiO surfaces. Thus, interactions between catalyst atoms and supports impact the stability and activity of catalysts. Supports deliver a platform on which catalytic reactions occur, while also determining local atomic configurations and electronic structures. In this regard, the maximization of metal atom catalytic activity via anchoring single atoms at stable support sites is essential to the rational design of SACs.

3.5. Metal-Support Synergistic Interactions and Confinement

Hu et al.^[111] synthesized Single Atom Ru catalysts stabilized by hybrid Amorphous/Crystalline FeCoNi (Ru SAs/AC-FeCoNi) Layered Double Hydroxide (LDH) nanoboxes for OER. Figure 7a depicts how Zeolitic Imidazolate Framework 67 (ZIF-67) nanocube precursors were first formed into Amorphous/Crystalline FeCoNi (AC-FeCoNi) LDH hollow

nanoboxes through Ni and Fe ionic exchange, then Ru SACs were inserted into AC-FeCoNi via in situ cation-exchange reactions to yield Ru catalysts. Figure 7b visualizes uniformly distributed, isolated Ru SACs as distinct bright spots on AC-FeCoNi surfaces via AC HAADF-STEM analysis, while 3D atom-overlapping Gaussian-function fitting (AOGF) mappings (Figure 7c), accompanied by 3D isoline (Figure 7d) and intensity profile (Figure 7e) analyses, confirm such dispersions. Figure 7f generalizes such conclusions over entire catalyst surfaces and all (Fe, Co, Ni, O, Ru) elemental mappings. Combined with these homogeneous distributions, the amorphous exterior and crystalline interior of AC-FeCoNi substrates respectively provided unsaturated coordination environments for Ru-support bond stabilization and long-term stability. The synergistic benefit of this hybrid AC substrate was demonstrated via investigations on solely crystalline supports (Ru SAs/C-FeCoNi), which observed distinctly lower Ru SAC activity and stability than Ru SAs/AC-FeCoNi. Thus, the hybrid amorphous/crystalline hollow nanobox structures of FeCoNi LDH-supported single Ru atoms (Ru SAs/AC-FeCoNi) are developed for enabling highly efficient electrocatalytic OER. The amorphous outer layers of Ru SAs/AC-FeCoNi are composed of multitudinous defect and other unsaturated coordination sites, which can actively serve as anchors to stabilize single Ru atoms. Their crystalline inner layers have highly symmetric and rigid structures, thereby strengthening support stability for OER longevity. The synergistic effects from single Ru atoms and hybrid amorphous/crystalline structures endow such catalysts with robust stability and superb electrocatalytic activity.

Hu et al.^[112] developed single atom Ru catalysts of varying coverage (x) on N-doped carbon (Rux SAs-NC) via spatial confinement within the micropores of MOFs. Figure 7g,h depicts Ru_{0.3} SAs-NC atomic structure via AC HAADF-STEM, finding isolated Ru atoms were uniformly dispersed across several NC pores and coordinated with N and N/O ligands. EDX mapping in Figure 7i confirms the uniform distribution of Ru and N over entire NC substrates. Here, MOF-assisted spatial confinement and ionic substitution strategies are employed to synthesize porous and binder-free SACs for highly-efficient cathodes, namely Ru single atoms distributed over N-doped porous carbon (Ru SAs-NC, including Ru_{0.1} SAs-NC and Ru_{0.3} SAs-NC) on carbon cloth (CC). Crucially, single active sites can maximize cathode catalyst redox activity, while N-doped porous carbon can provide a low impedance charge transfer pathway and offer specific regions for excess discharge products and mass transfer.

Lee et al.^[113] synthesized Ru single atom catalysts on Co-Fe bimetallic alloy substrates encompassed by graphitic carbon (Ru_{SA}CoFe₂/G) via a sol-gel micelle encapsulation method done in two steps. Such confinement of Ru SACs and Co-Fe supports within graphitic carbon largely yielded uniformly dispersed Ru SACs visualized by HADDF-STEM (Figure 7j), marked via bright spots (sites 1 and 2, red circles, Figure 7k) quantitatively evidenced to represent single Ru atoms (sizes \approx 2 Å, Figure 7l). Thus, the designed highly porous graphitic carbon substrates with partially covered defective layers in Ru_{SA}CoFe₂/G nanostructures expose active metal surfaces, possibly facilitating reactant and product mass diffusion during catalysis processes to and from active sites. Further, such porous structures imply

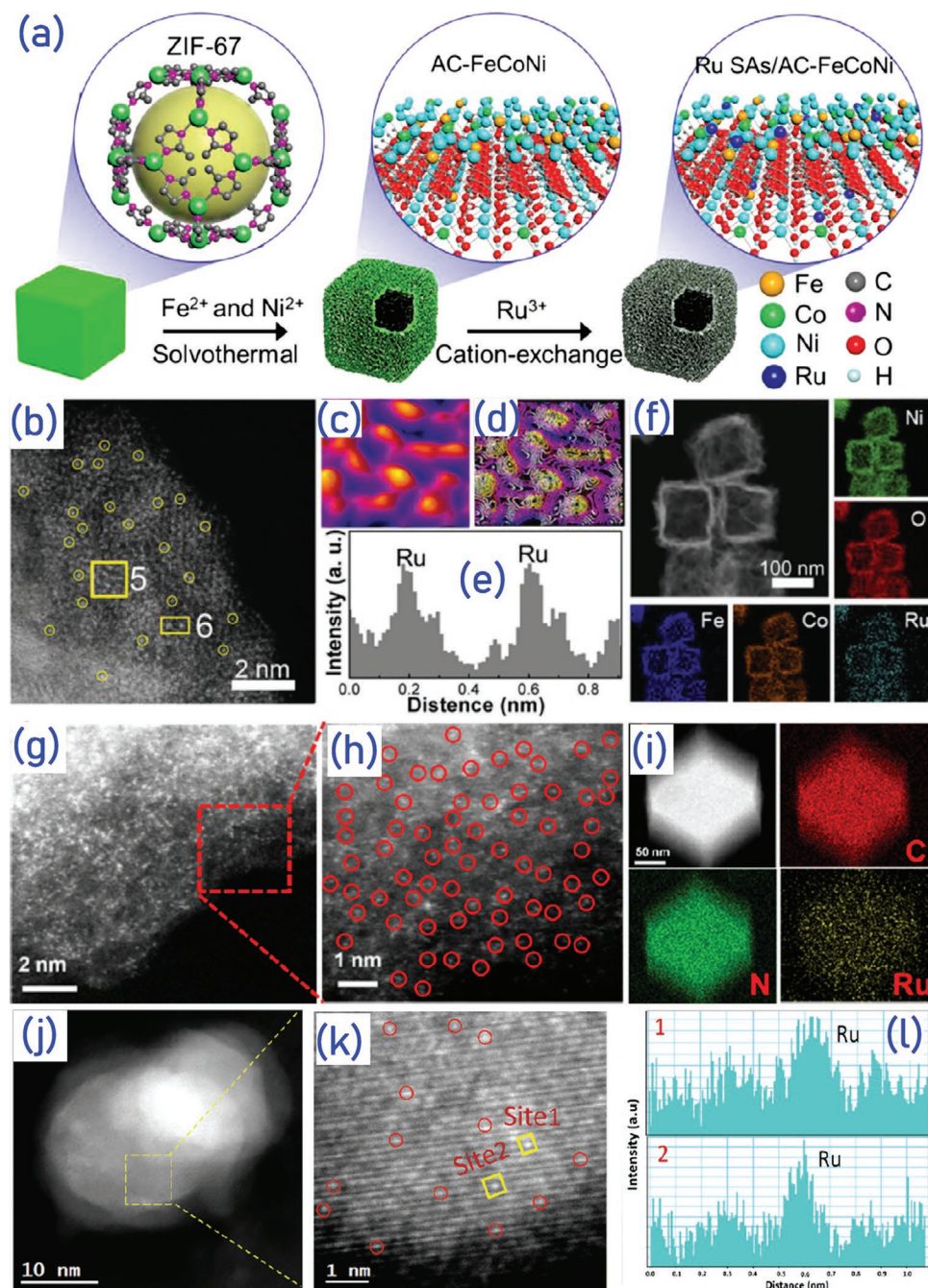


Figure 7. a) Schematic of Ru SAs/AC-FeCoNi synthesis. Ru SAs/AC-FeCoNi b) AC HAADF-STEM image, c) 3D AOGF mapping with d) 3D isolines from (b) (outline "5"), and e) intensity profile along outlined section "6" from (b). f) Ru SAs/AC-FeCoNi HAADF-STEM imaging with accompanying EDX mapping of Fe (dark blue), Co (orange), Ru (cyan), O (red), and Ni (green). Adapted with permission.^[111] Copyright 2020, Wiley-VCH Verlag GmbH & Co. KGaA, Weinheim. g,h) HAADF-STEM images of Ru_{0.3} SAs-NC (red circles mark Ru SACs) with matching i) EDX maps verifying uniform Ru and N distributions over NC supports. Adapted with permission.^[112] Copyright 2020, American Chemical Society. j,k) HAADF-STEM images of Ru_{SA}-CoFe/G with l) line-scanning intensity profiles over site 1 and 2 areas (yellow outlines) in (k). Adapted with permission.^[113] Copyright 2020, Royal Society of Chemistry.

fast electron transfer kinetics due to their metallic character, given graphitic carbon comprises electron transport layers. Such claims are substantiated by considering that high electrical conductivity is necessary for faster electron transfer during OER processes.

3.6. Faceted Nanoparticles

As shown in Figure 8a, Yang et al.^[114] synthesized Mn Isolated Single Atom catalysts anchored to N-doped carbon (Mn-ISAs@CN) through dispersing combinations of Mn(acac)₃ (Mn³⁺

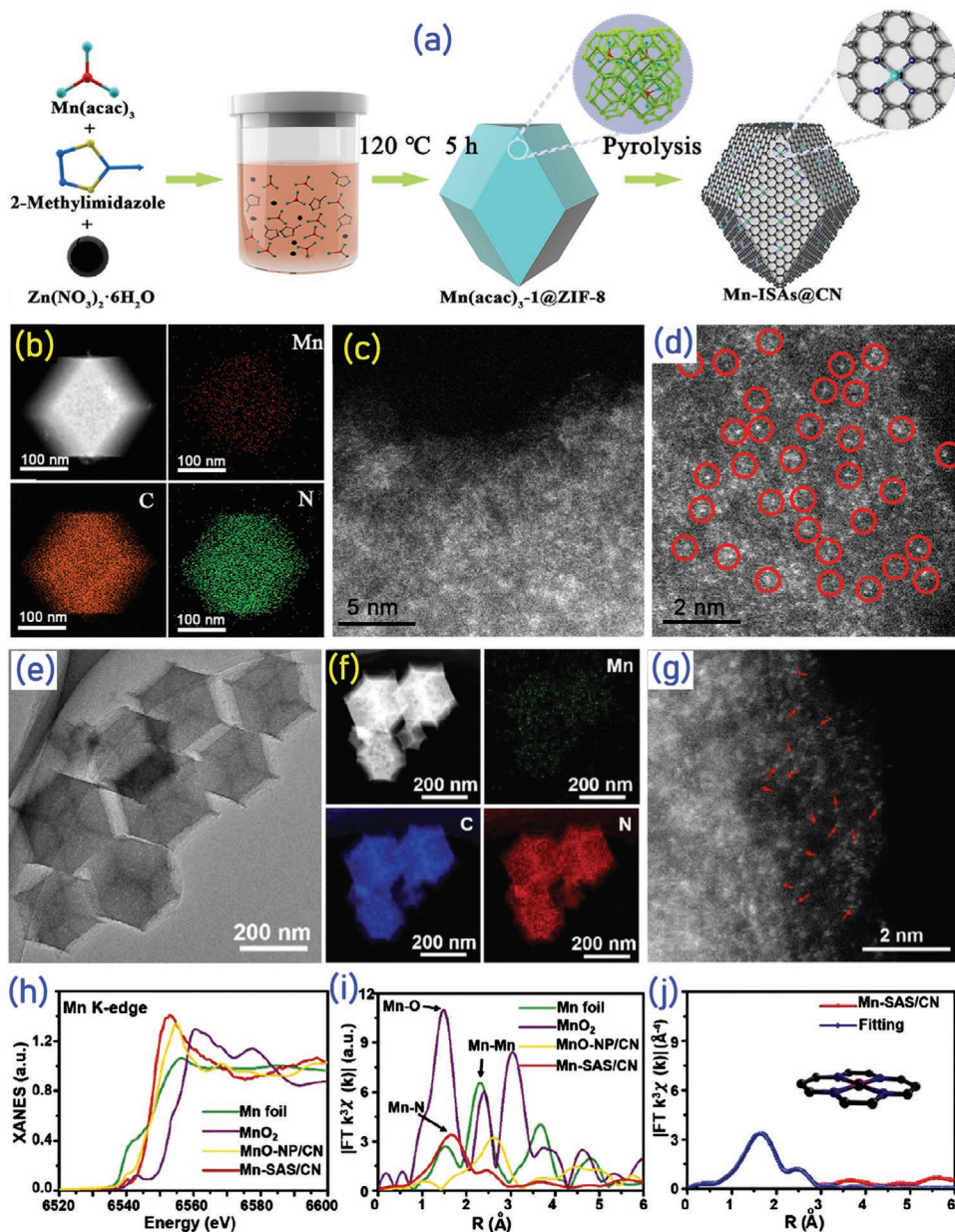


Figure 8. a) Heuristic depiction of Mn-ISAs@CN synthesis via MOF-based, cage-encapsulated precursor pyrolysis, with matching b) EDX and c,d) HAADF-STEM images. Adapted with permission.^[114] Copyright 2020, Elsevier. e) TEM, f) EDX, and g) enlarged AC HAADF-STEM imaging of Mn-SAS/CN, with red arrows directed to representative Mn SASs. Mn K-edge h) XANES and i) FT EXAFS spectra of Mn-SAS/CN, Mn foil, MnO₂, and MnO-NP/CN, with matching Mn-SAS/CN. j) EXAFS fitting curve in real space accompanied by a schematic model. Adapted with permission.^[29] Copyright 2020, Wiley-VCH Verlag GmbH & Co. KGaA, Weinheim.

acetylacetone), 2-methylimidazole, and Zn(NO₃)₂·6H₂O in methanol, then encapsulating reacted precursors in ZIF-8 cavities via a micropore confinement strategy to yield ZIF-8, Mn(acac)₃-1@ZIF-8 (0.8 mmol Mn(acac)₃ encapsulated in a ZIF-8 cage), and Mn(acac)₃-2@ZIF-8 (2.4 mmol Mn(acac)₃ within a ZIF-8 cage). Pyrolyzing these samples in Ar respectively produces CN, Mn NPs encapsulated in N-doped porous C (Mn-NPs@CN), and Mn-ISAs@CN. CN and Mn-NPs@CN controls were respectively produced with no and tripled Mn(acac)₃ concentration. EDX mappings from Figure 8b indicate uniform Mn (red), C (orange), and N (green) distributions over Mn-ISAs@CN surfaces, while HAADF-STEM images in Figure 8c depict no

agglomerated Mn clusters. Per SAC evidence of homogeneous Mn dispersions is given in Figure 8d as isolated bright dots highlighted in red circles. Evaluation of Bisphenol A (BPA) degradation over Mn-ISAs@CNs revealed not only that isolated, homogeneously distributed Mn SACs control such degradation via Mn-N₄ ligand complex formation, but also that under-coordinated sites on faceted NPs help anchor such complexes to stabilize catalytic structures. Thus, developed Mn-ISAs@CN nanostructures provided much larger specific surface areas, which are highly conducive and stable to adsorption.

Han et al.^[28] developed Mn Single Atom Site catalysts on N-doped Carbon supports (Mn-SAS/CN) via single stage

pyrolysis, yielding NPs with dodecahedral morphologies (Figure 8e). EDX mappings in Figure 8f illustrate uniform Mn (green), C (blue), and N (red) distributions over whole Mn-SAS/CN surfaces, while AC HAADF-STEM confirm Mn isolation via circled (red) bright dots (Figure 8g). Inductively Coupled Plasma Optical Emission Spectrometry (ICP-OES) resolved the Mn concentration (1.68 wt%) of Mn-SAS/CN, while Mn K-edge XANES spectra (Figure 8h) calculated its Mn valence state (2+). Figure 8i show Mn-SAS/CN FT EXAFS spectra with only one primary peak ($\approx 1.7 \text{ \AA}$) are inconsistent with the expectation Mn–Mn peaks ($\approx 2.3 \text{ \AA}$), further validating Mn atomic isolation on Mn-SAS/CN. Figure 8j displays EXAFS fitting resolving a Mn SAC coordination number (4.1) and mean bond length (1.97 \AA) consistent with Mn-N₄ ligand complexes resembling porphyrins. Combined lower valence state and higher coordination Mn active sites – which were associated with faceted NP morphology – facilitated both OH* adsorption on and electronic charge transfer towards Mn-N₄ complexes, tuning Mn-SAS/CN activity for ORR. Therefore, carbon matrix supported dodecahedral morphologies such as Mn-SAS/CN are important to high ORR performance, which may increase the conductivity – as well as charge and mass transfer – of catalytic materials during ORR processes due to their high concentrations of graphitic N.

3.7. Nanofoams and Nanofibers-in-Tubes

Shin et al.^[115] developed Pt SACs stabilized on 1D Melamine-derived Carbon Nitride/SnO₂ nano-heterostructure supports (Pt-MCN-SnO₂) via atomic trapping at heterojunctions in electrospun nanofibers (NF), yielding nanofiber-in-tube (FIT) catalytic structures (Pt-MCN-SnO₂ FIT) upon calcination.^[116] Figure 9a schematically depicts the synthesis of these catalysts, visualizing how electrospinning Pt-MCN solutions homogeneously distributes them over FITs. Figure 9b characterizes such FIT structures via brightness contrast in dark-field (DF) STEM images, resolving NFs (diameter $\approx 70 \text{ nm}$) inside larger nanotubes (diameter $\approx 250 \text{ nm}$). FIT structures have rough exterior nanotube surface morphologies attributable to the uniformly dispersed Pt-MCNs within them. Given 2D nanosheets crumple upon high-voltage electrospinning,^[117] Pt-MCNs produce electronegative surface charges binding Sn²⁺ ions onto FIT surfaces. This binding is responsible for roughening FIT surfaces upon Sn²⁺ ion oxidation during the calcination of crumpled Pt-MCNs. SnO₂ grain growth restraint during this process reduces Pt-MCN-SnO₂ grain sizes, consistent with previous literature.^[118] Further, electronegatively charged Pt-MCN surface sites adsorb uniform, thin layers of Sn precursors during Pt-MCN-SnO₂ formation (Figure 9a), likely due to spatial confinement of Pt SACs on Pt-MCNs that inhibits Pt aggregation during calcination. Figure 9c,d displays HAADF-STEM images of finalized Pt-MCN-SnO₂ FIT catalysts, probing Pt physical states via their z-contrast with Sn. Electrospun and calcinated SnO₂ grains feature bright spots (Pt) mismatched with SnO₂ lattices, indicating Pt atoms are generally anchored to SnO₂ FITs (red circles) as SACs with some exceptional Pt clusters (yellow circle). The stabilization of Pt SACs from heterojunction-induced spatial confinement and uniform Pt dispersion, combined with multifunctional activity and sensor selectivity

resulting from Pt-MCN complex bonding, yield effective catalysts due to the engineering of nanofiber structures. Thus, an effective approach for stabilizing a Pt SAC on a controllable 1D metal oxide nano-heterostructure support is demonstrated by trapping such single atoms at heterojunctions of carbon nitride/SnO₂ heterostructures. Given the ultrahigh specific surface areas of such nanostructures, such heterojunctions have maximized densities of catalytic active sites, as well as further enhanced catalysis at heterojunctions between carbon nitride and SnO₂. FIT structures are advantaged, as both the interior and exterior surfaces of their nanotubes – as well as the NFs inside these nanotubes – feature strongly increased catalytic reaction site densities, therefore incurring higher catalytic performance. Further, studied nanostructures helped to increase Pt content on Pt-MCNs. Pore size distributions of Pt-MCN-SnO₂ show highly increased mesopore densities and markedly increased surface areas.

Li et al.^[119] synthesized single atom Pt catalysts stabilized on PtCo alloyed nanosheets using trapped interstitial fluorine (SA-PtCoF) via the procedure depicted in Figure 9e. Atomic models also shown in Figure 9e indicate how interstitial F trapped in PtCoF matrices form lattice distortions, resulting in Pt–Co bond weakening and subsequent Pt atomization. This occurs by first fabricating PtCo via electrodeposition with Ni foam substrates in an aqueous plating solution of fixed CoS and variable H₂PtCl₆ concentration, as Ni foams feature 3D porous microstructures with high surface areas for Pt SAC loading.^[120] X-ray Fluorescence (XRF) confirms that developed PtCo alloys do not have stoichiometric (1:1) Pt/Co ratios, but rather have lower Pt compositions governed by variable H₂PtCl₆ concentrations. Formed PtCo nanosheets were etched by F plasma, improving nanosheet surface roughness while trapping F atoms in PtCo interstitial sites. Such trapping modulates interfacial free energy so as to weaken Pt–Co bonding, inducing Pt diffusion towards and stabilization on PtCoF nanosheet edges to ultimately yield SA-PtCoF. Figure 9f displays SEM images of SA-PtCoF nanosheets, visualizing a morphology characterized by exposed edges and rough surfaces grown vertically from Ni foam. Simultaneous and explicit observation of relatively light (F) and heavy (Co, Pt) atoms within SA-PtCoF was afforded through atomic-resolution AC Annular Bright-Field (ABF) STEM in Figure 9g, which discerns interstitial F atoms (yellow circles) from PtCo lattice fringes. Figure 9h illustrates corresponding HAADF-STEM images resolving lattice fringe spacings along the (101) (1.98 \AA) and (100) (2.28 \AA) planes of SA-PtCoF nanosheets alloyed with trace Pt concentrations, confirming lattice distortions due to interstitial F via lattice spacing differences. HAADF-STEM images in Figure 9i verify Pt SAC isolation (red circles) on nanosheet edges encompassed by lattice distortions ("T"), such that the PtCoF matrix of SA-PtCoF is distorted by F point defects.^[119] Given the presence of lattice distortions, mesoscale SA-PtCoF morphology characteristics, and Pt SAC location, interstitial F atom confinement appears to initially produce metastable SA-PtCoF that become stable via interfacial free energy reduction through Pt diffusion. This atomic separation process produces bifunctional catalysts with strong ORR and OER activities, given Pt SACs are isolated to particular support locations. Thus, the 3D porous microstructures of SA-PtCoF NSs with rough surfaces

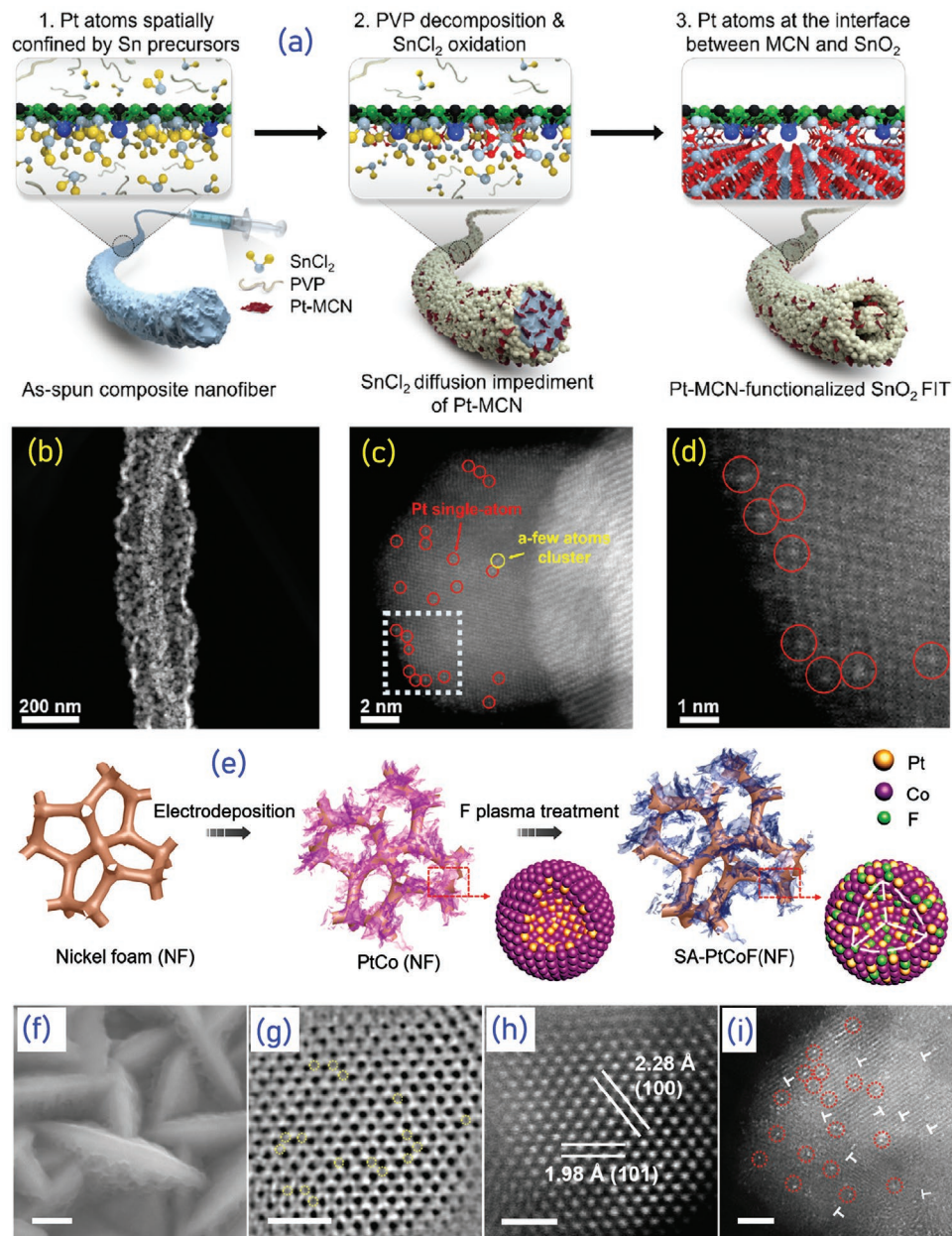


Figure 9. a) Heuristic depiction of Pt SAC and nanofiber-in-tube (FIT) formation with matching b) dark-field STEM and c,d) HAADF-STEM imaging of Pt-MCN-functionalized SnO₂ FIT (Pt-MCN-SnO₂) ((d) is white-dotted region from (c)). Adapted with permission.^[115] Copyright 2020, American Chemical Society. e) Heuristic visualization of SA-PtCoF nanosheet fabrication with corresponding f) SEM, g) ABF-STEM (yellow circles resolve interstitial F atoms), and h) HAADF-STEM images of SA-PtCoF nanosheets grown vertically from nickel foam (Scale bars: 200 nm (f), 1 nm (g,h)). i) HAADF-STEM SA-PtCoF image incorporating lattice distortions with isolated Pt atoms (red circles) and distortions ("T") (Scale bar: 2 nm). Adapted with permission.^[119] Copyright 2020, Royal Society of Chemistry.

constitute additive-free catalysts with high surface areas and plentiful active sites, demonstrating remarkable benefits for ZABs over powder catalysts because of their inhibited catalyst deactivation. In addition, designed SA-PtCoF electrocatalysts deliver high electronic conductivity via tuning the spin and charge densities of atoms, which greatly contribute to their improved catalytic activities. Further, F-plasma etching treatment of PtCo remarkably improves the surface roughnesses of NSs. During this process, the F atoms were incorporated in

the interstitial sites of the crystalline PtCo nanostructures and greatly influenced their interfacial free energies. Thus, Pt–Co bonds become weakened by the thermodynamically driven trapped F atoms in the interstitial sites, subsequently leading to the stabilization and diffusion of Pt atoms on the nanosheet edges of PtCoF.

In summary, both dark-field (DF) and bright-field (BF) Aberration Corrected (AC) TEM modes are extensively applied to detect the individual atomic structures of of SACs and their

aggregated nanostructure distributions. When combined with element mapping techniques, HAADF-STEM can directly locate SACs and determine their distributions over surfaces. Additionally, HAADF-STEM can study interfacial interactions at an atomic-scale between SACs and the anchoring sites of their supports. From such characterization, the link between experimental synthesis techniques that develop different SAC-support nanostructure designs^[121–127] and how resulting atomic coordination influences the bonding responsible for advantageous catalytic activity and durability is valuably developed.

4. The Impact of Composition on Experimental Characterization

Supported SAC characterization is essential to understanding their microstructures, as microstructure is strongly related to electrochemistry. Thus, identifying isolated SACs and confirming their homogeneous, isolated spatial distributions is important. Currently, characterization techniques used to identify SACs encompass EXAFS, XANES, X-ray Photoelectron Spectroscopy (XPS), and X-ray Absorption Spectroscopy (XAS). XANES spectra arise from electronic transitions in the –20–50 eV range relative to the absorption edge, and are applied to assess SAC oxidation states, geometries, and electronic structures. In contrast, EXAFS evaluates such transitions within a 50–1000 eV range from the absorption edge, providing valuable information on radial distribution functions, interatomic distances, coordination numbers, and bond lengths. EXAFS has been implemented to study SACs in *in situ* and *ex situ* modes. XPS is highly sensitive to elemental composition and surface conditions, studying surface elemental oxidation states, thermal stabilities, and SAC compositions under realistic conditions. Directly or indirectly, such considerations of oxidation states, electronic structures, and related properties rely on characterizing the impact of SAC composition on SAC-support interactions and ultimately catalytic properties. In this section, both *ex situ* and *in situ* characterization methods are introduced to explain the connection between characterized support microstructures and corresponding SAC chemical environments. Moreover, DFT calculations offer deep insights on stable active centers, how composition affects them, and the reaction mechanisms through which they catalyze chemical reactions. Theoretical calculations assessing more complex reaction systems are required to confirm and support experimental conclusions, identifying how SAC composition and support structure independently and synergistically contribute to improving catalytic reaction mechanisms.

4.1. Performance of Fe-Based SACs with Structurally Engineered Supports

Fe K-edge XANES spectra (**Figure 10a**) of Single-Atom Fe-N_x-C Nanosheets^[89] review the Fe coordination environments of Fe-N_x-Cns-800, or Fe SACs encompassed by N ligands supported by carbon nanosheets heated at 800 °C, with Fe foil, FeO, Fe₂O₃, and phthalocyanine iron (FePc) controls. Given the onset of the Fe-N_x-Cns-800 XANES peak at 7113 eV and its

corresponding adsorption edge location between those of FeO and Fe₂O₃, the Fe-N₄ ligand complex is likely non-planar and features a Fe oxidation state between 2+ (FeO) and 3+ (Fe₂O₃). FT k^3 -weighted EXAFS spectra in *R* space from Figure 10b resolve Fe-N/Fe-O bonding peaks at ≈1.48 Å for all structures but Fe foil, while the absence of Fe-Fe peaks in Fe-N_x-Cns-800 referenced using Fe foil verifies such SACs feature isolated metal active centers. Figure 10c simulates fitted FT-EXAFS spectra relative to a referenced FeN₄O₂ experimental model in *R* space, confirming that the isolated Fe sites of Fe-N_x-Cns-800 are coordinated in ligand complexes with 4 N and 2 O atoms. The reaction of such ligand complexes with thiocyanate ions (SCN[–]) established Fe-N_x sites as the cause of Fe-N_x-Cns-800 catalytic activity during dichloroethane dehydrogenation, as confirmed by ethylene yield rates, faradaic efficiencies, and current density measurements. XRD analysis (Figure 10d) of Fe SACs comprising atomic Fe-N₄ embedded on hierarchically porous carbon nanorods^[92] (Fe/N-CNRs) further confirms reliable metal site isolation, given the respective presence and absence of XRD peaks for graphitic C-C and crystalline Fe-Fe bonding. Synthesis procedures, including template generation and acid washing, improved support porosity towards eliminating metal Fe aggregation and Fe₂O₃ formation, as seen in structural comparisons between SACs with (Fe/N-CNRs) and without (Fe/N-CNRs-NW) acid washing and the absence of pertinent peaks in Fe/N-CNRs XRD spectra. Increased Fe/N-CNR porosity was further vindicated via N₂ temperature adsorption-desorption experiments shown in Figure 10e, illustrating high Fe/N-CNR BET surface area (666.7 m² g^{–1}), formidable total pore volume (1.3 cm³ g^{–1}), and hierarchies of coexisting variably sized pores. Figure 10f pore diameter distribution curves validate such Fe/N-CNR micropore and mesopore hierarchies through a measured pore diameter domain of 0.7–40 nm. More specifically, Figure 10e quantifiably attributes Fe/N-CNRs surface area improvements over Fe/N-CNRs-NW to improved porosity, which is linked to metal and Fe₂O₃ nanoparticle aggregation prevention. Given acid washing does not destroy nanorod morphology, the procedure ultimately helps expose active sites and facilitates adsorbate transport during ORR.

Fe SACs encompassed^[96] by N_x moieties supported by hierarchical porous carbon (SA-Fe-NHPC) formed low valence oxidation states, as demonstrated from the Fe K-edge XANES spectra in Figure 10g. FT k_3 -weighted EXAFS spectra peaks from Figure 10h substantiate Fe-N first coordination shells (~1.5 Å) and preclude Fe-Fe bonding (~2.2 Å) in SA-Fe-NHPCs relative to Fe foil and analogous nanoparticle electrocatalyst (NP-Fe-NHPC) references, verifying Fe isolation excluding strong Fe-N ligand complex bonds in SA-Fe-NHPCs. Figure 10i depicts thermodynamic (barometric) N₂ adsorption-desorption analyses for SA-Fe-NHPCs, NP-Fe-NHPCs, and Fe-N₄ complexes supported on carbon without hierarchical porosity (FeNCs), confirming significant increases in adsorbed N₂ volume (V_{ads}) and hysteresis loops at respective lower ($P/P_0 = 0–0.015$) and higher ($P/P_0 = 0.4–0.95$) N₂ partial pressures for both SA-Fe-NHPC and NP-Fe-NHPC. Further evidence that SA-Fe-NHPC supports are comprised of hierarchically interconnected micropores and macropores was provided^[96] by strong BET surface areas (1327 m² g^{–1}) and total pore volumes (2.7 cm³ g^{–1}), which also imply that dense and exposed Fe-N_x complexes

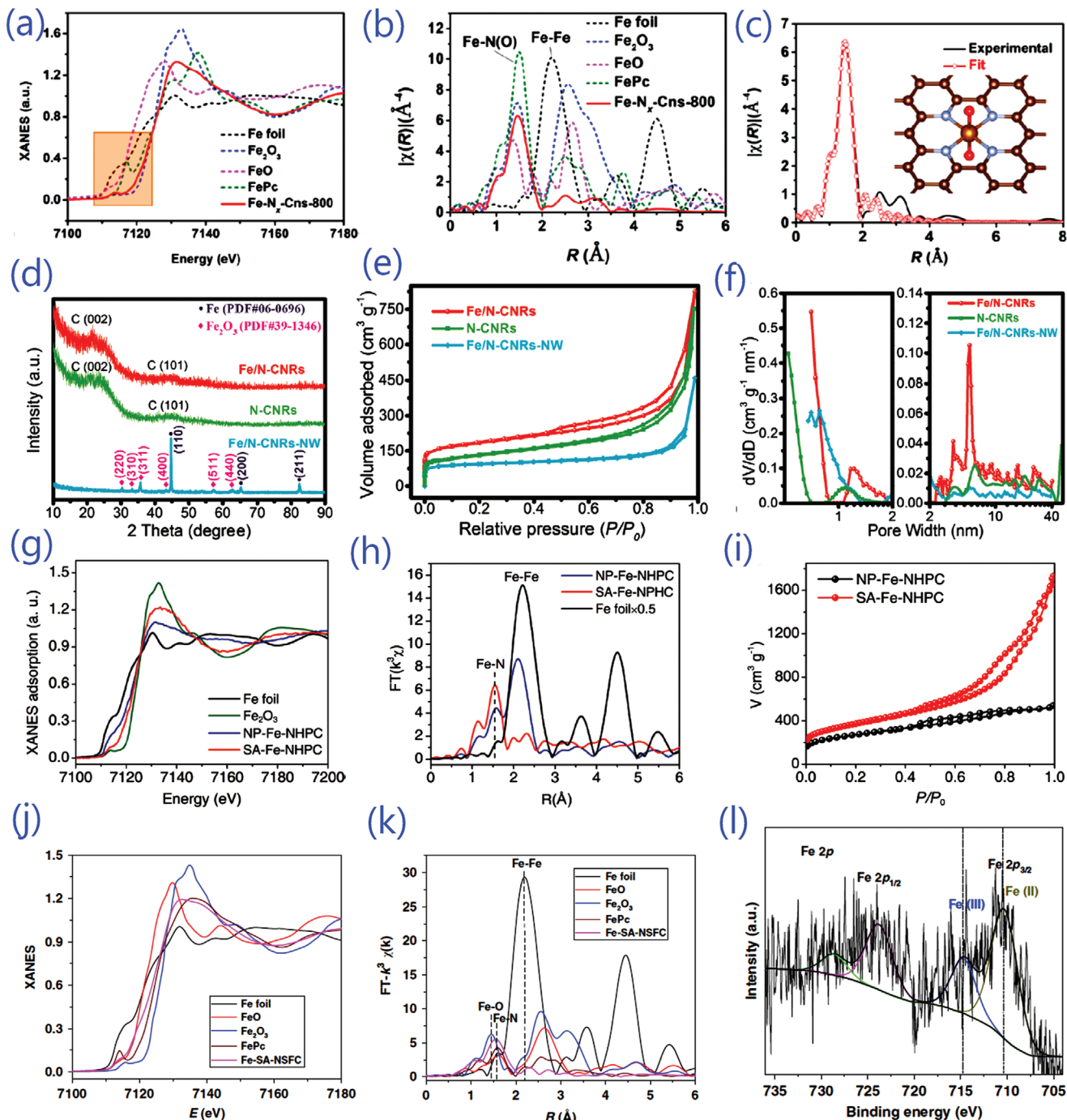


Figure 10. Fe foil, Fe_2O_3 , FeO , FePc , and $\text{Fe-N}_x\text{-Cns-800}$ a) Fe K-edge XANES and b) FT-EXAFS spectra in R space. c) Experimental versus fitted FT-EXAFS results of $\text{Fe-N}_x\text{-Cns-800}$ in R space. Adapted with permission.^[89] Copyright 2020, American Chemical Society. Fe/N-CNRs, N-CNRs, and Fe/N-CNRs-NW d) XRD patterns, e) N_2 adsorption-desorption proportions, and f) pore diameter distributions. Adapted with permission.^[92] Copyright 2021, Wiley-VCH Verlag GmbH & Co. KGaA, Weinheim. SA-Fe-NHPC and reference g) Fe K-edge XANES spectra, h) Fe K-edge FT EXAFS spectra, and i) N_2 adsorption-desorption isotherms. Adapted with permission.^[96] Copyright 2020, Wiley-VCH Verlag GmbH & Co. KGaA, Weinheim. Fe-SA-NSFC, Fe foil, FeO , Fe_2O_3 , and FePc j) Fe K-edge XANES spectra and k) k^3 -weighted $\chi(k)$ -function FT EXAFS spectra, with Fe-SA-NSFC l) Fe 2p XPS spectra. Adapted with permission.^[98] Copyright 2020, Springer Nature.

are available to electrocatalytic reactions such as ORR using SA-NHPCs. Further, compositional generalization of Fe-based SAC supports^[98] to incorporate N, S, and F dopants in porous graphitized carbon (Fe-SA-NSFCs) was investigated via XANES spectra in Figure 10j, revealing Fe SAC oxidation states of 2+

via comparisons of the onsets of Fe K-edge adsorption peak locations to FeO (2+) and Fe_2O_3 (3+) references. Figure 10k depicts how Fe-SA-NSFC FT k^3 -weighted EXAFS spectra only feature peaks at $\approx 1.57 \text{ \AA}$ albeit not 2.20, 1.45, or 1.80 \AA , respectively evidencing the presence of Fe-N first coordination shells

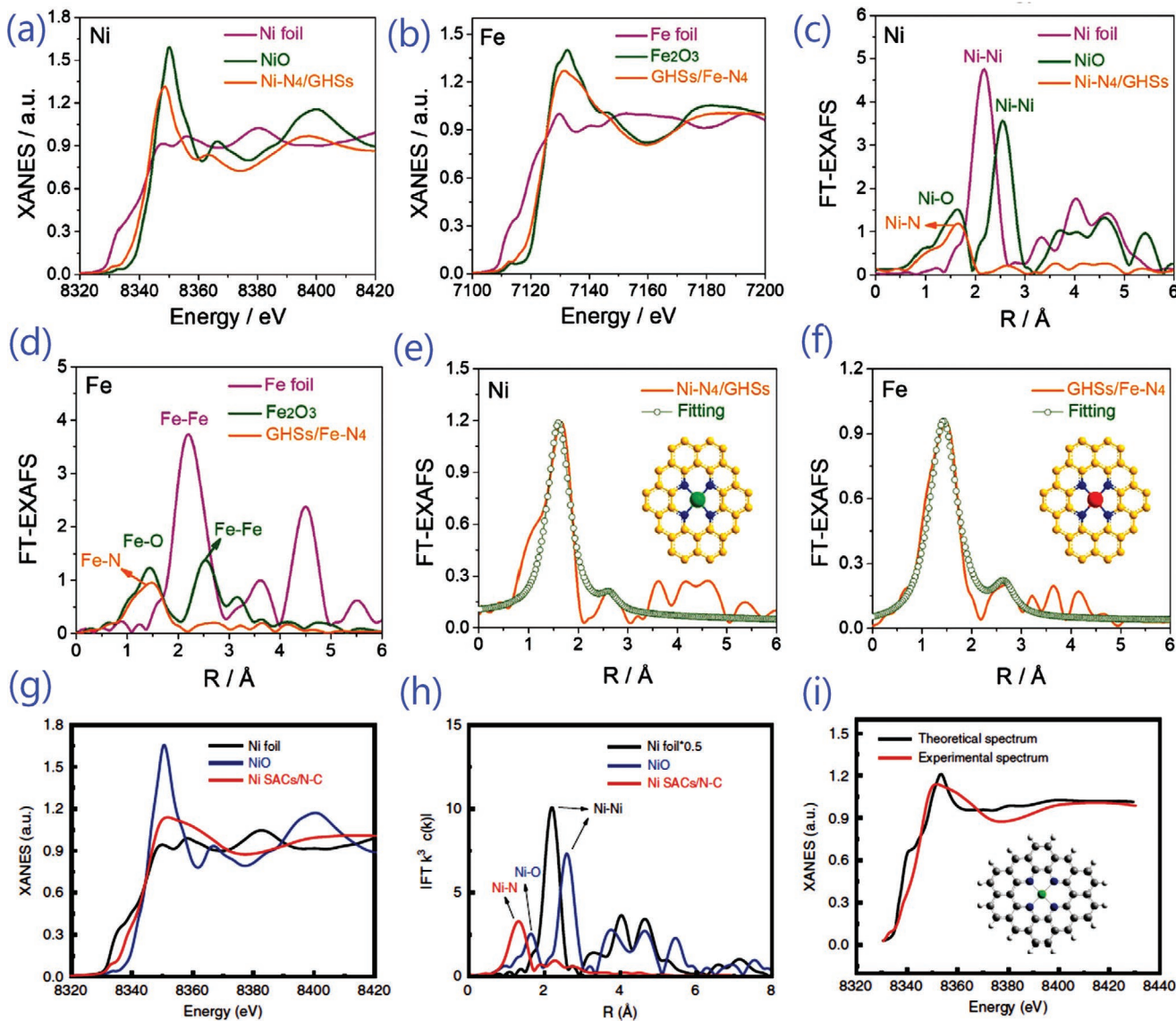


Figure 11. a) Ni and b) Fe K-edge XANES spectra. c) Ni and d) Fe K-edge FT EXAFS spectra. e) Ni-N₄/GHSs and f) GHSs/Fe-N₄ EXAFS fitted curves in R space with respective atomic structural models (insets). Adapted with permission.^[101] Copyright 2020, Wiley-VCH Verlag GmbH & Co. KGaA, Weinheim. Ni SACs/N-C, NiO, and Ni foil g) XANES spectra and h) FT EXAFS spectra of Ni K-edge. i) Ni SACs/N-C XANES spectra at Ni K-edge comparing experiment (red curve) and theory (black curve) with simulated graphene/Ni-N₄ structure (inset). Adapted with permission.^[102] Copyright 2020, Springer Nature.

and absence of Fe-Fe, Fe-O, and Fe-S bonding referenced to Fe foil, FeO/Fe₂O₃, and FeS₂. This confirms Fe active centers are isolated from one another, which was further substantiated by Fe 2p XPS spectrum portraying the absence of metal Fe agglomeration and dominance of Fe²⁺ in Fe-SA-NSFC through Figure 10l.

4.2. Characterizing Fe and Ni Hollow Nanosphere Ligand Coordinated Complexes

Chen et al.^[101] designed Janus structures based on dual single-atomic Ni-N₄ and Fe-N₄ sites for selective oxygen electrocatalysis. Ni K-edge (Figure 11a) and Fe K-edge (Figure 11b) XANES spectra of layered graphene hollow spheres – with interior

Ni (Ni-N₄/GHSs) and exterior Fe (GHSs/Fe-N₄) N-bonded ligand complexes – observe their respective onsets of absorption energy peaks between those of Ni/Fe foil and NiO/Fe₂O₃, indicating respective Ni and Fe active center oxidation states between 0–2+ and 0–3+. Differences in Ni and Fe valences from one another, and their proposed crystalline references, can be attributed to N ligand complex bonding affecting their partial charges. Figure 11c,d displays the k^2 -weighted FT EXAFS of Ni and Fe K-edges from Ni-N₄/GHSs and GHSs/Fe-N₄, depicting primary respective peaks at 1.63 and 1.47 Å linked to Ni-N and Fe-N bonding. Further, such plots depict evidence neither for Ni-Ni nor Fe-Fe crystalline bonding, implying that Fe and Ni SACs are homogeneously distributed without metal aggregation over graphene. Fitted EXAFS curves for Ni-N₄/GHSs (Figure 11e) and GHSs/Fe-N₄ (Figure 11f) verify Ni and Fe SAC

coordination numbers of ≈4, as well as respective Ni-N and Fe-N ligand bond lengths of 2.09 and 1.98 Å. All of these results substantiate the Ni-N₄ and Fe-N₄ ligand complex bonding environments of corresponding SACs depicted in the insets of given plots. The reliable construction of respective Ni and Fe ligand complexes enables strong bifunctional OER and ORR activities due to balancing the adsorption-desorption kinetics of their reaction intermediates, which occurs by reducing the orbital hybridization between metal active center *d*-orbitals and coordinated N 2p orbitals.

Further confirmation of such ligand-related contributions^[102] to SAC electrocatalytic activity is offered by investigating Ni SACs on N-doped hollow carbon spheres (Ni SACs/N-C), starting with their Ni K-edge XANES curves versus NiO and Ni foil controls. Figure 11g indicates that the onset of the Ni SACs/N-C absorption edge lies between Ni foil and NiO references, resolving a Ni SAC valence state between 0 and 2+. Corresponding FT EXAFS depicted in Figure 11h calculate a single dominant Ni SACs/N-C peak (≈1.32 Å) induced by Ni-N bonding, in contrast with Ni-Ni crystalline bonding in referenced structures or otherwise observed Ni aggregation. Further analysis deduces a Ni active center coordination number of 4 and an average Ni-N bond length of 1.92 Å, confirming that Ni-N₄ ligand complexes bonded to supports comprise studied SACs. Further investigation of XANES spectra in Figure 11i, which compare simulated models versus experimental structures, corroborate the graphene simulated atomic model depicted in the inset. Overall, Ni-N₄ complex bonding precluded further bonding with N during NO oxidation, rendering the most favorable mechanism for such oxidation across electrocatalysts proportionally more favorable in Ni SACs/N-C than analogous studied nanoparticle (Ni NPs/N-C) controls.

4.3. Coupled Defects and Coverage Effects: Oxygen Vacancies and Clustering in Ir-Based SACs

Ir SACs were coupled with oxygen vacancies (V_O) on NiCo₂O₄ nanosheets (Ir-NiCo₂O₄ NSs) to form electrocatalysts,^[106] fostering charge transfer and thus catalyzing OER activity. Figure 12a depicts a XANES spectra comparison between Ir-NiCo₂O₄ NSs and commercial IrO₂, displaying de-intensified and downward shifted Ir-NiCo₂O₄ NSs peaks that indicate their lower Ir valence states. Complementary FT EXAFS in *R* space from Figure 12b feature single primary peaks (≈1.5 Å) for both Ir-NiCo₂O₄ NSs and IrO₂ attributable to Ir-O bonding. Further, second Ir-Ir and third nearest neighbor Ir-Ir bonding are respectively present and absent in IrO₂ and Ir-NiCo₂O₄, verifying the lack of metal aggregation in SACs. However, such bonding was referenced to the Ir-O₆ octahedron (≈2.0 Å) without correcting for coordination, and multiply composed atoms are available for Ir SAC bonding. Thus, Figure 12c illustrates wavelet transformed (WT) EXAFS analysis to resolve SAC bonded atoms by composition and *k* space resolution rather than just radial distance, resolving a single Ir-NiCo₂O₄ NSs peak (≈78 Å⁻¹) resembling that of Ir-O bonding in IrO₂. After confirming bonded compositions, full Ir-NiCo₂O₄ NS ligand complex coordination was deduced quantitatively via fitted EXAFS curves in Figures 12d,e, linking the primary Ir-O bonding peak (≈1.5 Å) to a coordination number of 4.05 relative to IrO₂ referenced Ir-O

(4.71) and Ir-Ir (5.46) bonding. Computational electronic structure characterization finds V_O weaken *d-d* coupling between bonded Ni and Co within supports to relatively strengthen orbital hybridization with surface O 2p orbitals, ultimately facilitating Co binding to intermediate O-based adsorbates given the maintenance of a relatively constant valence state. Given the general flexibility of Co valence states, consistent Ir-O₄ ligand complex bonding to such Co is required to maintain their charge while accommodating adsorbing H₂O and H reactants and intermediates. This complicated charge transfer arrangement is ultimately needed to simultaneously handle multiple OER intermediates in sequence, balancing the relative stabilities of all reactions within the entire process.

Highly concentrated Ir SACs on a NiO matrix support^[110] have controllable oxidation states depending on their support bonding and their aggregation, which is evidenced by detailed experimental electronic structure analysis. Figure 12f links an IrO₂ XPS spectra with two doublet peaks – which are centered at paired (62.1, 65.0) and (63.1, 66.0) eV binding energies – primarily to Ir⁴⁺, while complementary Ir 4f spectra of Ir-NiO produce doublet peaks that mirror (62.3, 65.1 eV) or differ (61.9, 63.8 eV) from their IrO₂ analogues. Though the majority of Ir SACs on NiO supports still have a 4+ valence state, the differing peaks indicate that a mixture of Ir⁴⁺ and Ir³⁺ comprise Ir-NiO electrocatalysts. Both Ir 4f spectra feature peaks (66.7, 68.3 eV) attributable to the impact of Ir on Ni 3p related bonding, which Figure 12g more directly visualizes via shared Ni 2p_{3/2} XPS Ni and Ir-NiO “multiplets” at 853.7 and 855.6 eV. As Ir surface coverage increases, the ratio between these “multiplet” intensities varies, implying averaged surface Ir valence state is tunable with Ir surface loading. Figure 12h confirms slight deviation of the Ir oxidation state in Ir-NiO from 4+ by tracking near-edge adsorption peak (white line) position in Ir L₃-edge XANES, corroborating previous XPS findings. Further, white line peak intensity is generally inversely proportional to *d* orbital PDOS filling, and is thus sensitive to valence state and electronic configuration changes. Figure 12i demonstrates how Ni oxidation state slightly improves with Ir loading via Ni K-edge XANES spectra, while complementary Ir L-edge FT EXAFS from Figure 12j subtly resolve Ir-Ni peaks (≈2.5 Å) from Ir-Ni-O bonding encompassing the SAC with no Ir-Ir metal aggregation. Extending FT EXAFS curve fitting to the Ni K-edge (Figures 12k) not only corroborates Ir-Ni bonding, but also indicates reduced Ni-O bond distance in Ir-NiO (versus pristine NiO) with improved Ir loading. Therefore, increasing Ir surface coverage strengthens Ni-O interactions and in turn modulates Ni oxidation states near adsorbed SAC ligand complexes.

4.4. Structural Implantation and Confinement in Ru SACs

Hu et al.^[111] designed Ru SACs on hybrid amorphous/crystalline FeCoNi (Ru SAs/AC-FeCoNi) layered double hydroxide (LDH) substrates feature synergistic effects enhancing OER that ultimately result from differences between internal support-support and external support-ligand bonding character. Initial Ru K-edge energy XANES characterization in Figure 13a compares SAC spectra with those of Ru foil and RuCl₃ controls, resolving an averaged Ru valence state of 2.8+. Complementary FT *k*³-weighted EXAFS spectra from Figure 13b confirm the sole

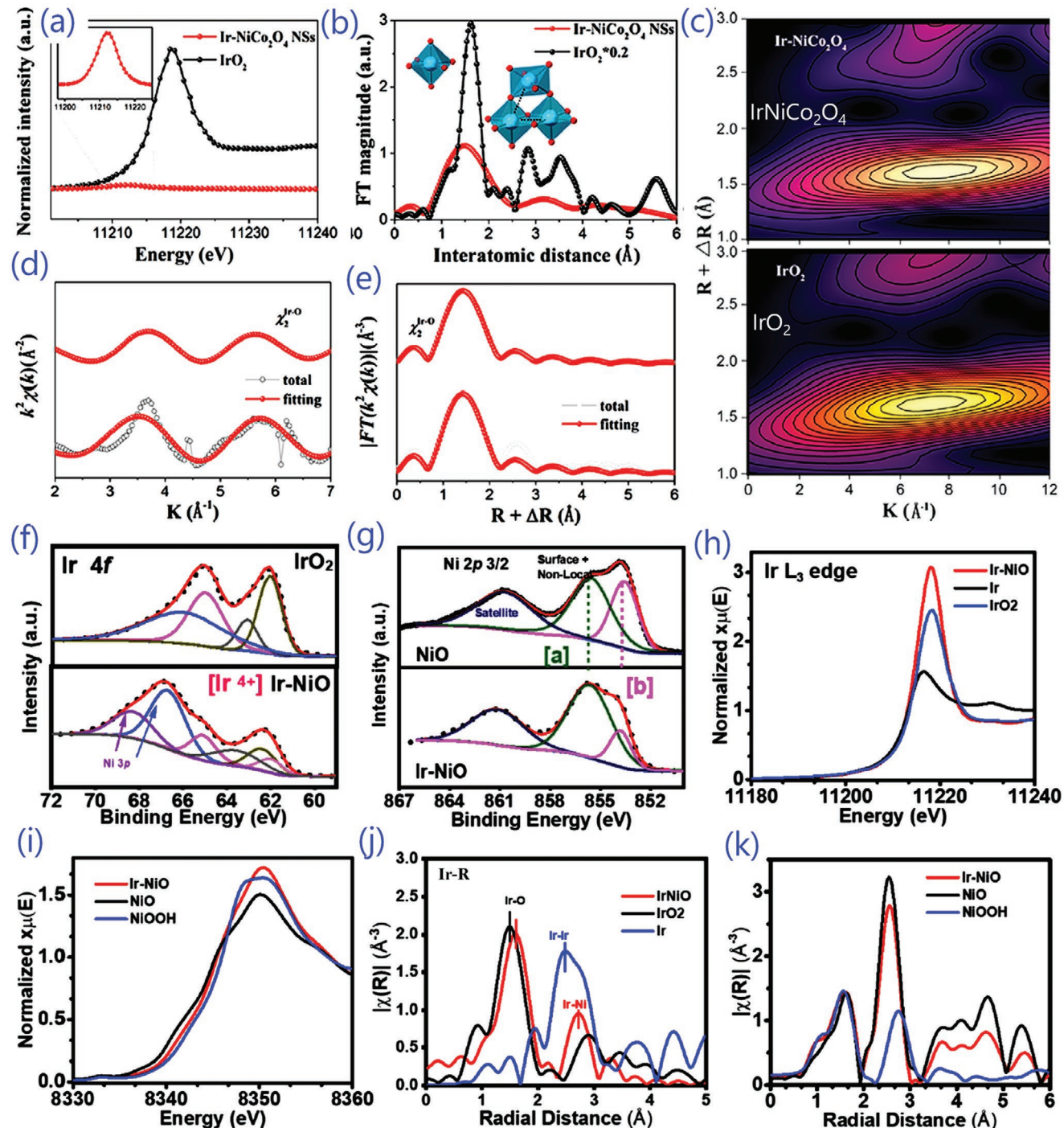


Figure 12. IrO_2 and $\text{Ir}-\text{NiCo}_2\text{O}_4$ NSs a) XANES and b) EXAFS spectra, with c) EXAFS signals of k^3 -weighted Ir L_3 -edge wavelet transforms. $\text{Ir}-\text{NiCo}_2\text{O}_4$ NSs L_3 -edge EXAFS of Ir in d) k and e) R spaces, including Ir–O backscattering signals (χ^2) from fitted (red line) and experimental (black line) data. Adapted with permission.^[106] Copyright 2020, American Chemical Society. IrO_2 , Ir-NiO , and NiO curve-resolved XPS of f) Ir 4f and g) Ni 2p regions, with matching h) Ir L_3 -edge synchrotron-based XANES spectra also referenced to Ir foil. Ir-NiO , NiO , and NiOOH i) K-edge synchrotron-based XANES spectra of Ni, with Ir-NiO and additional reference FT EXAFS spectra at the j) Ir L -edge and k) Ni K -edge. Adapted with permission.^[110] Copyright 2020, American Chemical Society.

salience of Ru–O bonding in Ru SAs/AC-FeCoNi samples, as well as the absence of Ru–Ru and Ru–Cl bonding indicating metal aggregation or incomplete RuCl_3 conversion. Additional evidence favoring Ru site isolation proceeds from Ru SAs/AC-FeCoNi

EXAFS spectra curves fitted in R space, which confirm fourfold Ru SAC coordination with likely O ligands in Figure 13c. Ru K -edge WT EXAFS measurements in Figure 13d depict a primary peak ($\approx 4.3 \text{ \AA}^{-1}$) to distinguish coordination by composition,

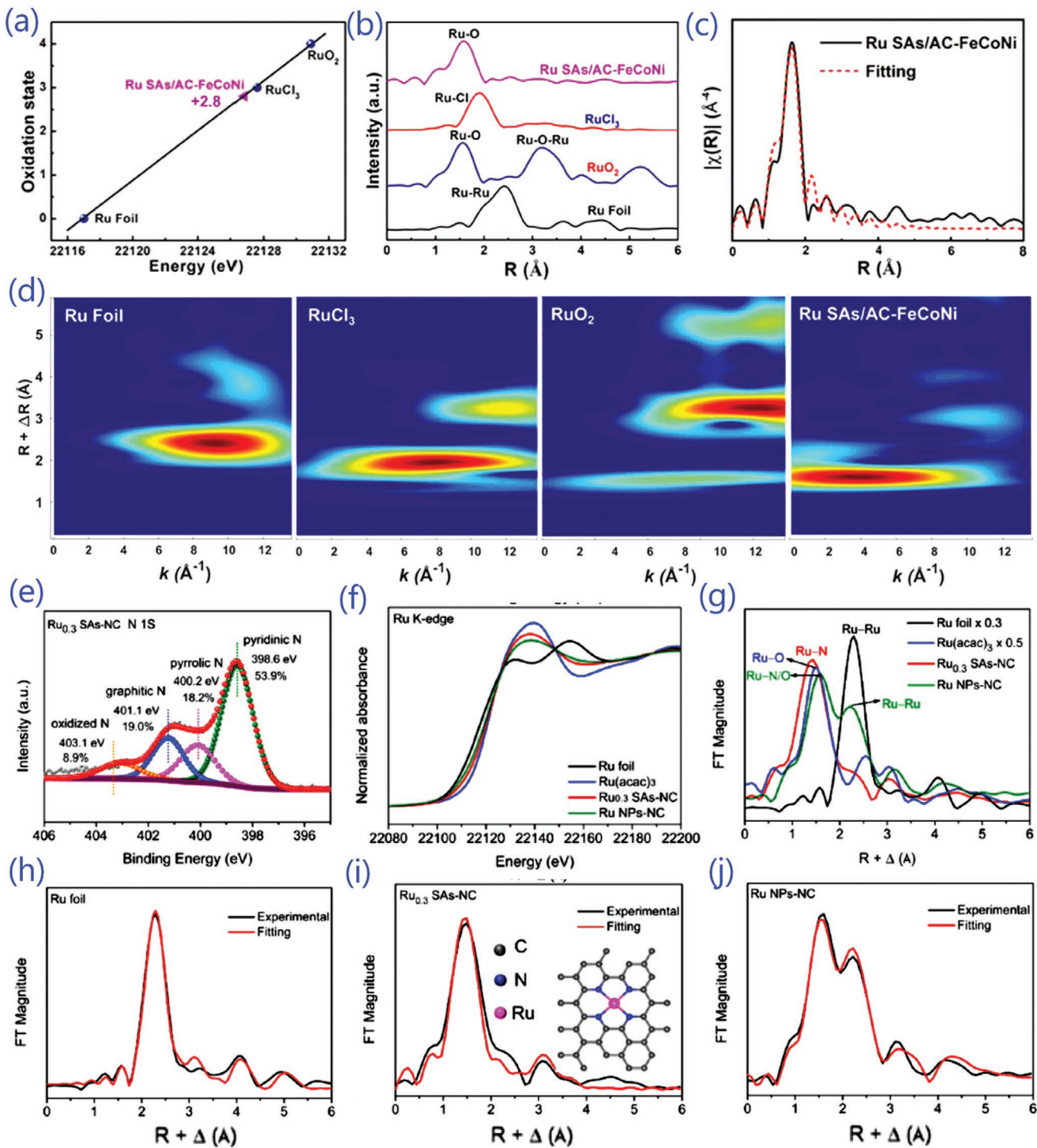


Figure 13. a) K-edge XANES derived Ru oxidation states of studied structures, b) Ru K-edge EXAFS spectra and c) fitted EXAFS curves in R space, and d) WT EXAFS signals. Adapted with permission.^[111] Copyright 2021, Wiley-VCH Verlag GmbH & Co. KGaA, Weinheim. e) Ru_{0.3} SAs-NC high resolution N 1s XPS spectra, with matching Ru_{0.3} SAs-NC, Ru foil, Ru(acac)₃, and Ru NPs-NC f) normalized XANES and g) FT-EXAFS spectra in R space. h) Ru foil, i) Ru_{0.3} SAs-NC, and j) Ru NPs-NC fitted EXAFS curves in R space, showing schematic structure as inset in (i) with Ru (purple), N (blue), and C (gray) atoms. Adapted with permission.^[112] Copyright 2020, American Chemical Society.

confirming that this fourfold ligand coordination is comprised of exclusively Ru-O complex bonding. Unlike other SAC-support structures, Ru SACs are embedded within amorphous/

crystalline supports, such that the fourfold coordinated Ru were able to reversibly maintain relatively stable valence states over OER cycles via flexible electronic charge transfer between

their ligands and neighboring Fe, Co, and Ni support atoms. While these interactions contributed to catalytic activity and the stability thereof, the LDH matrix in which Ru SACs were implanted remained rigid, ensuring structural durability and thus the synergistic effects of activity and durability during OER via differential ligand support and support-support bonding.

Further, Ru SACs anchored^[112] via ligands to N-doped porous carbon supports ($\text{Ru}_{0.3}$ SAs-NC) extend from the stable implantation of Ru within support matrices to their metastable spatial confinement adsorbed within an N-doped porous graphitic carbon substrate. The high-resolution N 1s XPS spectra of $\text{Ru}_{0.3}$ SAs-NCs from Figure 13e depict four fitted peaks, with magnitudes proportional to the prevalence of particular N bond types that have known binding energies. Such peaks can be connected to pyridinic N (398.6 eV, 53.9%), pyrrolic N (400.2 eV, 18.2%), graphitic N (401.1 eV, 19%), and oxidized N (403.1 eV, 8.9%) bonding.^[112] Figure 13f portrays the Ru K-edge XANES spectra of $\text{Ru}_{0.3}$ SAs-NCs referenced to analogous nanoparticle (Ru NPs-NCs), Ru foil, and $\text{Ru}(\text{acac})_3$ (Ru^{+3} acetylacetone) controls, confirming a $\text{Ru}_{0.3}$ SAs-NC oxidation state between that of Ru foil (0) and $\text{Ru}(\text{acac})_3$ (3+). Corresponding FT-EXAFS spectra in Figure 13g of these samples resolve a single dominant $\text{Ru}_{0.3}$ SAs-NC peak ($\approx 1.5 \text{ \AA}$) connected to Ru-N ligand bonding, in contrast to the Ru-Ru bonding peak ($\approx 2.3 \text{ \AA}$) prevailing in Ru foil and Ru NPs-NCs. Simulated fitted EXAFS curves of Ru foil (Figure 13h), $\text{Ru}_{0.3}$ SAs-NC (Figure 13i), and Ru NPs-NCs (Figure 13j) models in R space are compared to experimental signals, confirming strong peaks at larger bond distances signifying Ru-Ru bonding are exclusive to Ru foil and Ru NPs-NCs. In contrast, the idiosyncratic first Ru coordination shell of $\text{Ru}_{0.3}$ SAs-NC is demarcated by an isolated, low distance peak, consistently modeling Ru-N bonding and verifying the Ru-N ligand complex constituting SACs. Given that such Ru- N_4 complexes are spatially confined within graphitic support defect sites rather than adsorbed on top of them, their bonding to additional adsorbates – such as Li_2O_2 – is not only preferentially favored but also metallic in character. Such metallic bonding enables the large, uniform transfer of electronic charge across the entire ligand complex and surrounding C, facilitating activity over a relatively delocalized set of sites encompassing SACs. Such sites may be flexibly active during the different intermediate stages of various electrochemical and catalytic reactions.

4.5. Switching Active Sites with Adaptable Mn Valence States

Yang et al.^[114] developed single Mn atoms anchored on N-doped porous carbon. Prior to evaluating the mechanistic transitions affordable to Mn-based SACs, the structure of isolated single Mn atoms on N-doped porous carbon matrices (Mn-ISAs@CN) is evaluated with respect to Mn foil and Mn_2O_3 references. Comparative Mn K-edge XANES spectra from Figure 14a infer a Mn-ISAs@CN valence state between those of Mn foil (0) and Mn_2O_3 (3+), initially implying the flexibility of Mn SAC bonding. Corresponding FT-EXAFS spectra in Figure 14b depict a strong, isolated, lower bond distance Mn-ISAs@CN peak ($\approx 1.3 \text{ \AA}$) implying Mn-N bonding. This contrasts with the additional, larger bond distance linked peaks present in Mn

foil and Mn_2O_3 , indicating the lack of Mn-Mn aggregation in such SACs that is already consistent with similar HAADF-STEM and XRD results. Figure 14c displays experimental and fitted Mn-ISAs@CN EXAFS curves with a primary peak (1.3 \AA) correlated with the first coordination shell of Mn-N bonding, resolving a Mn active center coordination of 4 and implying an Mn- N_4 composed ligand complex. To verify the compositions of studied bonds in multi-component systems, Figure 14d-f portray WT EXAFS analyses in both k and R spaces for all studied systems. Such analyses resolve a single Mn-ISAs@CN peak (4.0 \AA^{-1}) that can be more directly linked to Mn-N coordination, establishing the Mn-ISAs@CN structural model illustrated in Figure 14g. Nevertheless, for Mn-ISAs@CN reactions requiring both peroxyomonosulfate (HSO_5^-) and hydroxyl (OH^-) ions, Mn active centers embedded in CN supports and pyrrolic adjacent N ligand sites are respectively more favorable for adsorption. Distance reduction between such adsorbates catalyzes such reaction processes significantly, and is facilitated by facile charge transfer between adjacent ligand complex Mn and N.

Further, Han et al.^[28] studied the active sites of Mn- N_4 for oxygen reduction. More directly, dynamic and reversible modulation of Mn active center valences from higher ($\text{Mn}^{\text{H}+}\text{-N}_4$) to lower ($\text{Mn}^{\text{L}+}\text{-N}_4$) charges can responsively tune OH coverage in ORR and related reactions. In operando, Mn K-edge XANES testing of Mn single-atom-site electrocatalysts on N-doped carbon supports (Mn-SAS/CN) was completed over potentials varying between 0.3 and 0.9 V. Such incremental potential testing gradated between open circuit and ex situ extremes in Figure 14h, producing contrasting respective adsorption edge (6544 vs 6548 eV) and white line peak (6554 vs 6561 eV) result domains. Relative to MnO and Mn_2O_3 references, Mn-SAS/CN Mn K-edge energies indicated Mn valence states increased from 2+ to 3+ when situated within electrolytes in operando. As demonstrated in Figure 14h,j, XANES spectra binding energies shifted down with lower applied potentials (0.9–0.3 V) and higher ORR overpotentials (0.3–0.9 V), while reversing the applied potential produced an inverse trend. As overpotential increased, Mn valence states decreased, OH adsorption lowered, OH desorption improved, and ultimately $\text{Mn}^{\text{L}+}\text{-N}_4$ ligand complexes formed. Figure 14i,k indirectly portrays relative Mn coverage by adsorbed OH via surface-sensitive $\Delta\mu$ -XANES, referencing no OH coverage relative to an applied potential of 0.3 V due to the negligible XANES binding energy shifting below this threshold. Differencing XANES shifting at each studied potential relative to corresponding spectra at 0.3 V, $\Delta\mu$ -XANES can resolve OH coverage on Mn sites over potential domains. Treating open-circuit $\text{Mn}^{\text{L}+}\text{-N}_4$ sites as completely covered by OH, OH coverage at an applied potential can be calculated by setting the applied potential versus open-circuit $\Delta\mu$ ratio proportional to the corresponding OH coverage ratio. This proportion can be applied to Mn-SAS/CN catalyzed interfacial ORR, as OH desorbs from $\text{Mn}^{\text{L}+}\text{-N}_4$ sites incrementally with potential. Ultimately, the active site of $\text{Mn}^{\text{H}+}\text{-N}_4$ ($\text{H}^+\approx 3+$) initially adsorbs OH during ORR, while dynamic SAC reduction to $\text{Mn}^{\text{L}+}\text{-N}_4$ ($\text{L}^+\approx 2+$) tuned OH desorption – and thus final catalytic reactivity – via charge transfer facilitated by applied potential and the ability of Mn to readily accommodate different valence states.

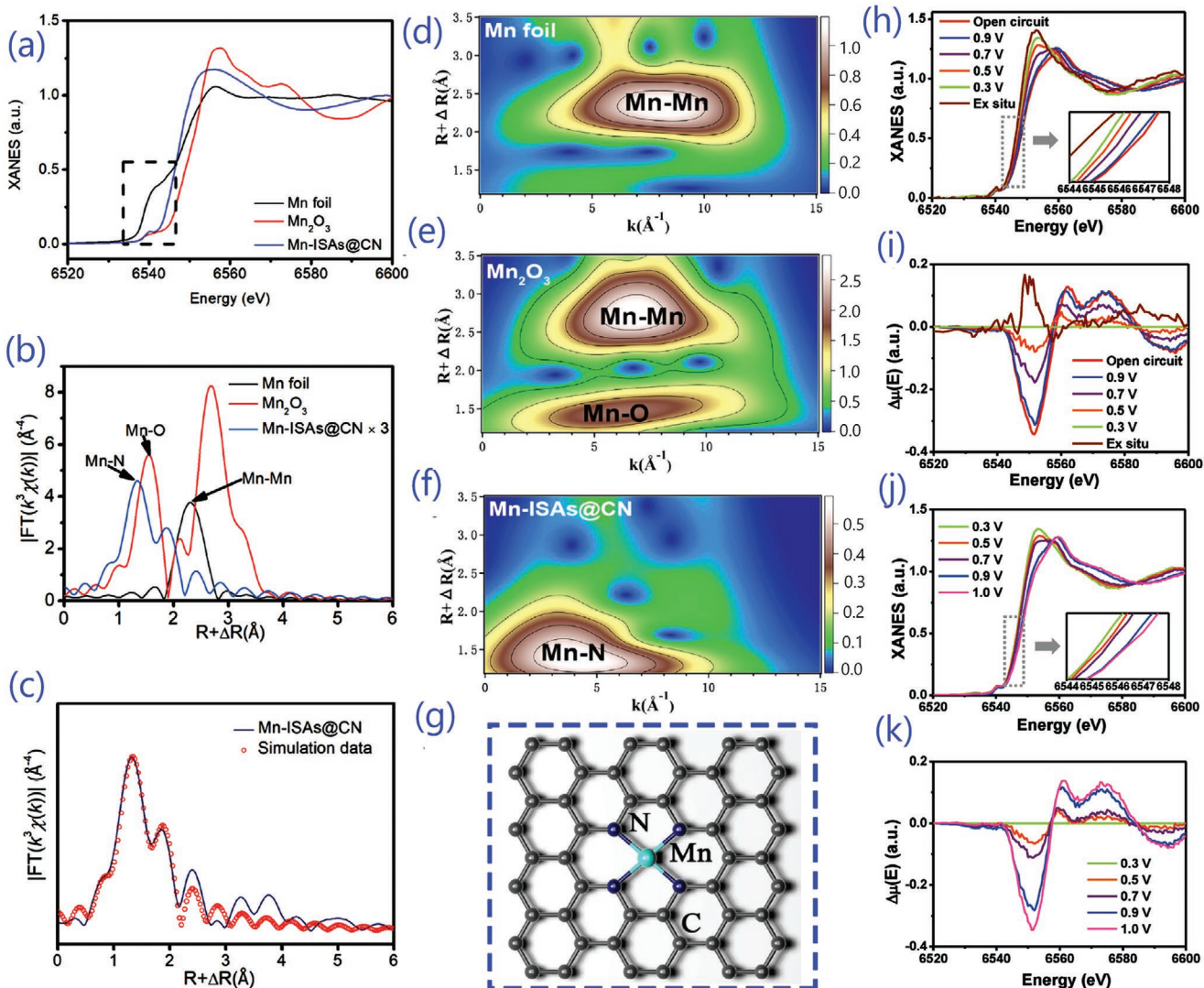


Figure 14. Mn foil, Mn_2O_3 , and Mn-ISAs@CN Mn K-edge a) normalized XANES spectra, b) FT k^3 -weighted $\chi(k)$ -function of EXAFS spectra, c) fitted EXAFS curves, and d-f) WTs of EXAFS spectra. g) Mn-ISAs@CN schematic structure with Mn (dark blue), N (blue), and C (gray) atoms. Adapted with permission.^[14] Copyright 2020, Elsevier. Ex situ Mn-SAS/CN h,j) operando XANES and i,k) $\Delta\mu$ -XANES ($\mu_E - \mu_{0.3V}$) over open circuit h,i) 0.9–0.3 V and j,k) 0.3–0.9 V potential ranges in O_2 -saturated KOH. Adapted with permission.^[28] Copyright 2021, Wiley-VCH Verlag GmbH & Co. KGaA, Weinheim.

4.6. Pt-Based SAC Trapping towards Improving Electrocatalyst Multifunctionality

Kim et al.^[115] designed Pt SACs, which are anchored on melamine-derived carbon nitride nanosheet functionalized SnO_2 (Pt-MCN-SnO₂) nanofibers within tubes (FIT) comprised of polyvinylpyrrolidone (PVP), simultaneously feature Pt and MCN-SnO₂ heterojunction active sites for catalyzed gas sensing, while also stabilizing SACs at such heterojunctions. Morphologically, FIT structures can anchor Pt SACs on the interior and exterior surfaces of PVP nanotubes, as well as their encased SnO₂ nanofibers, to maximize the amount of electrocatalyst surface area available to active sites. Figure 15a quantifies this increased Pt-MCN-SnO₂ specific surface area ($54.29 \text{ m}^2 \text{ g}^{-1}$) relative to that of pristine SnO₂ nanofibers ($13.15 \text{ m}^2 \text{ g}^{-1}$) via BET analysis, albeit not while confirming which component of

such surface area primarily features Pt SAC active sites. Referenced to Pt foil, Pt-MCNs, and Pt-doped SnO₂ (Pt-SnO₂), the Pt L₃-edge XANES spectra of Pt-MCN-SnO₂ in Figure 15b resolve Pt oxidation states between those of metallic Pt foil and Pt in Pt-SnO₂. Adsorption near edge peak intensity and position are both higher in Pt-SnO₂ than Pt-MCN-SnO₂, evidencing the lower oxidation states of Pt in Pt-MCN-SnO₂ and precluding favorable Pt-Sn place exchange substitution mechanisms. In moderate contrast, Pt-MCN-SnO₂ and Pt-MCN observe similar Pt XANES peak positions ($\approx 11574 \text{ eV}$) albeit disparate peak intensities favoring the latter, further reducing Pt oxidation state estimates in Pt-MCN-SnO₂ and implying Pt SACs are anchored by morphologies allowing strong Pt-Sn charge transfer. Figure 15c compares FT-EXAFS of Pt-MCN-SnO₂ to formerly described references, resolving a primary peak ($\approx 1.6 \text{ \AA}$) connected to Pt-N/C bonding that confirms

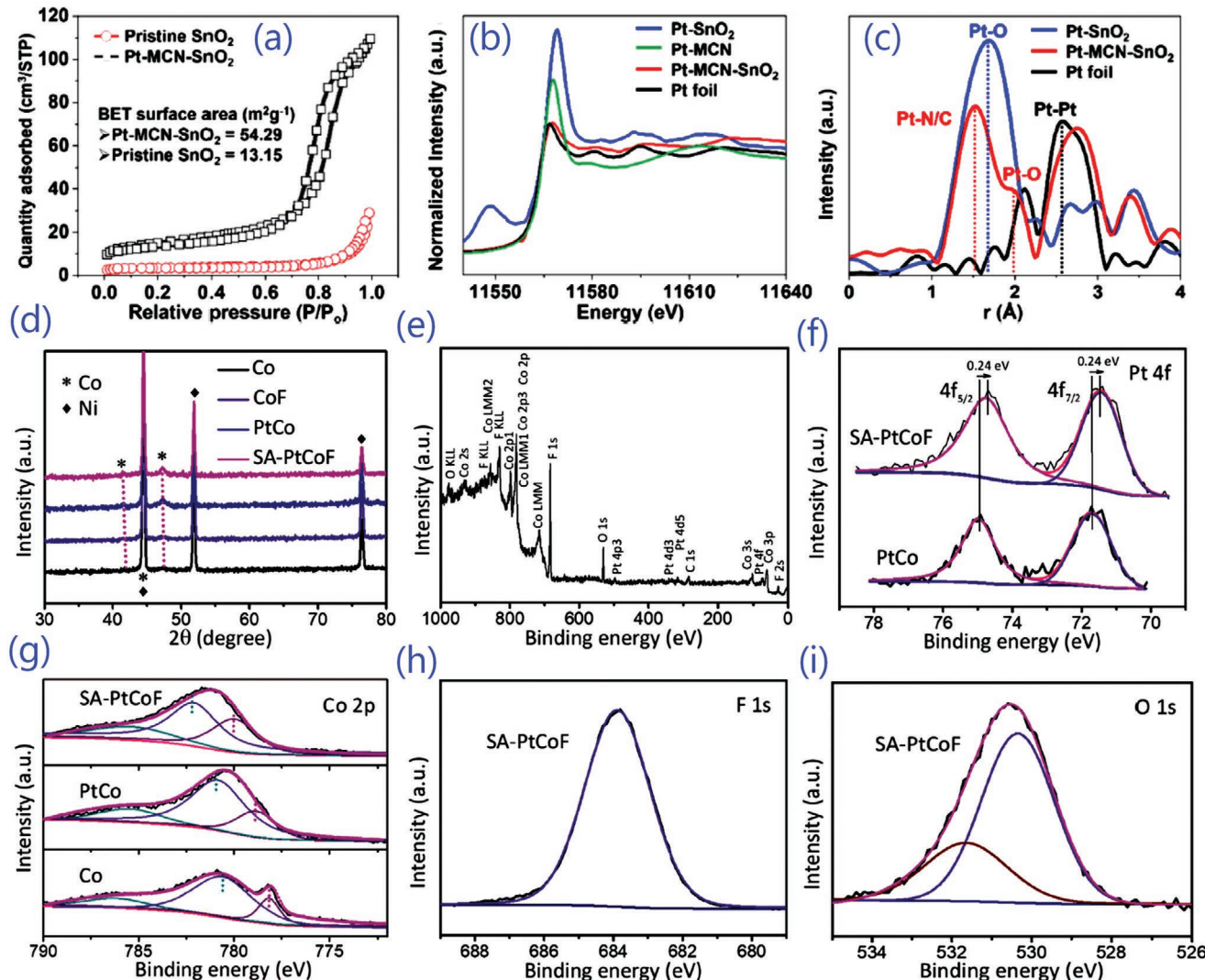


Figure 15. Pt-MCN-SnO₂ and reference a) BET surface areas, b) Pt L_3 -edge XANES spectra, and c) FT k^2 -weighted $\chi(k)$ -function of Pt L_3 -edge EXAFS spectra. Adapted with permission.^[115] Copyright 2020, American Chemical Society. SA-PtCoF, PtCo, Co, and CoF d) XRD patterns and e) XPS spectra. SA-PtCoF high resolution XPS spectra for f) Co 2p, g) Pt 4f, h) F 1s, and i) O 1s. Adapted with permission.^[119] Copyright 2020, Royal Society of Chemistry.

Pt SACs remain stably anchored to MCNs. The second most intense Pt-MCN-SnO₂ peak (≈ 2.76 Å) can be attributed to Pt-Sn bonding, substantiating claims that charge transfer from Sn to Pt reduced the Pt valence state of Pt-MCN-SnO₂. In combination, these results indicate that Pt SACs were primarily trapped at the heterojunctions formed between the interior surfaces of FIT tubes and the exterior surfaces of their encased Pt-MCN-SnO₂, providing them with multiple functionalities encompassing Pt-Sn charge transfer, stable anchoring on supports, and enhanced gas sensing capability.

Multifunctionality improving the activity^[119] of multiple reactions, such as OER and ORR, can be achieved in Pt SACs on alloyed PtCo nanosheet supports with interstitially trapped F (SA-PtCoF). XRD analysis from Figure 15d evaluates SA-PtCoF relative to Co, CoF, and PtCo references, resolving three salient characteristic peaks connected to diffraction along the (100) (41.551°), (002) (44.551°), and (101) (47.451°) planes of hexagonally close-packed Co. Though Pt-based diffraction peaks are

missing due to their low concentration, the structural distortion induced by interstitial F and Pt indirectly shifts all depicted Co XRD peaks downward with respect to unstrained references. Figure 15e displays XPS spectra that preliminarily verify SA-PtCoF contains Co, Pt, F, and surface adsorbed O, all of which are subsequently characterized via element-specific high resolution XPS. Corresponding SA-PtCoF Pt 4f peaks (71.48, 74.72 eV) in Figure 15f can be connected to metal Pt active centers, with binding energies mildly shifted downward relative to PtCo references (by 0.24 eV) to portray strong SAC-support bonding. Downward shifts in such binding energies correlate with similar changes in Pt d-band centers, weakened O adsorption on Pt SACs, and charge transfer across Pt ligand complexes. Also, confining interstitial F within PtCo nanosheets increases measured Pt content (4.37–5.81 wt%) incorporated into SA-PtCoF, implying that trapping F stabilizes Pt SACs on nanosheets supports. Figure 15g depicts Co 2p_{3/2} XPS spectra for SA-PtCoF with three salient peaks attributable to Co⁰ (779.9 eV), Co²⁺

(781.9 eV), and their satellite (785.8 eV), illustrating increased binding energies relative to Co and PtCo. Such upward shifts, which are partially induced by trapped interstitial F, correlate with Co *d*-band modulation that proportionally compensates for corresponding adjacent Pt changes via charge transfer. Figure 15h displays the F 1s XPS spectra of SA-PtCoF with a peak (683.9 eV) representing Co–F bonding, which verifies interstitial F trapping within PtCo matrices. Figure 15i resolves two fitted XPS O 1s peaks (530.4, 531.6 eV) respectively attributable to surface absorbed OH and O, which represent the adsorbed intermediates of both OER and ORR. The combination of Pt-Co charge transfer, SAC-O bond weakening, Pt SAC loading improvement, and the ability to accommodate multiple reaction intermediates ensures the multifunctional, strong catalytic performance of SA-PtCoF in both OER and ORR.

4.7. Bonding, Charge Transfer, and Property Tuning: “Rare-Earth” Metal SACs

Chen et al.^[128] synthesized La SACs on carbon nitride supports from aqueous $\text{La}_2(\text{CO}_3)_3$ (O/La-CN) via the procedure shown in Figure 16a, yielding amorphous photocatalysts comprised of La-N ligand complexes. Spherical AC HAADF-STEM images in Figure 16b–d do not discern metal NPs or clusters in smaller substrate regions, though detectable bright dots (highlighted by green circles) indicate uniformly dispersed La SACs on CN supports. Evaluating O/La-CN electronic structure and coordination environment, Figure 16e depicts La L₃ edge *k*³-weighted EXAFS of compared O/La-CN and La_2O_3 samples in real space, while Figure 16f makes respective comparisons via XANES spectra. EXAFS portrays La-O and La-La ($\approx 4.21 \text{ \AA}$) bonding interactions present in La_2O_3 , but absent in O/La-CN. In contrast, O/La-CN EXAFS spectra prominently feature nearest neighbor La-N (La-N', 2.63 Å, six-fold coordination), La-C (3.85 Å, four-fold coordination), and second nearest neighbor La-N (La-N'', 4.85 Å, four-fold coordination) bonds in their respective first, second, and third coordination shells. Such results confirm that La SACs are isolated, uniformly distributed on CN substrates, and anchored to CN via N ligands. Matching XANES spectra indicate relatively high edge absorption strength correlated with unoccupied *d*-orbital electron delocalization, inferring its La *d* orbitals proportionately donate electrons. The DFT-calculated total density of states (TDOS) comprising the top valence band (VBM) of O/La-CN (Figure 16g) largely consist of N and O orbital character, implying N and O *p*-orbital electron localization around La SACs. Such implications were evidenced by partial density of states (PDOS) analysis in Figure 16h, which resolved N 2p and La 5d orbital peak overlap to confirm *p-d* orbital hybridization. The strength of this La–N orbital hybridization was further substantiated by electronic location function (ELF) plots in Figure 16i, indicating La SACs stably bond to CN supports via their N ligands. Bader charge and differential charge distribution analyses completed in Figure 16j,k quantitatively demonstrate how electrons transfer from La SACs to their N ligands and ultimately C and O substrates, namely by using hybridized La-N orbitals. Therefore, the modulation of charge transfer across hybridized La-N orbitals, or La-N bond strength, was found to ultimately tune catalytically relevant

O/La-CN properties, including conductivity and CO_2 photocatalytic reduction reactant, intermediate, and product formation.

Sc and Y (effective) “rare-earth” SACs on amorphous N-doped carbon supports (Sc₁/NC, Y₁/NC) were developed from ZIF-8 precursors.^[129] Uniformly dispersed Y atoms are highlighted (yellow circles) in HAADF-STEM images shown in Figure 16l. XANES spectra in Figure 16m assess Y SAC local coordination environments, revealing the Y₁/NC adsorption edge position strongly differs from that of Y foil but resembles that of Y_2O_3 . This implies an average Y₁ valence state of around 3+.^[130] Figure 16n resolves Y₁/NC FT-EXAFS spectra with a primary peak mirroring that of the Y_2O_3 Y-O bond (1.8 vs 1.7 Å, respectively).^[131] First-principles DFT simulations supplement these EXAFS results by resolving the most favorable coordination of Y active sites in Y₁/NC,^[132] reviewing two carbon defect types (A and B, Figure 16o) within which single Y SACs were inserted. Type A defects consist of graphite carbon planes with two nearest neighbor C site vacancies, as observed in most M–N–C (M = transition metal) SACs in past literature.^[133] Type B defects are larger, including more adjacent C vacancies to accommodate the larger atomic radii of rare-earth and related metals. In combination with these defect types, different quantities and configurations of N ligands attached to single Y were tested for favorability via their adsorption energies (E_{ads}).

Figure 16p visualizes all tested structures with their respective E_{ads} , marking more favorable structures with proportionally lower (higher negative) energies.^[133] Models with negative E_{ads} – enumerated (from left to right in Figure 16p) as “9”, “4”, “8”, “1”, and “7” and ordered according to their relative energetic favorability – are favorable relative to their constituent substrates and inserted Y atoms, thus they are anticipated to favorably form in experiment notwithstanding thermodynamic conditions. Model “9” (Y–B–N₃, or type B with 3 N ligands) was the most favorable structure tested and thus was analyzed via FT-EXAFS to further study Y₁/NC. Figure 16q displays optimized FT-EXAFS fitting results, with the first peak representing the three Y–N and three Y–C bonds directly connected to the active center. Second and third nearest neighbor Y–C bonding comprises the weak peaks observed from 2.5 to 3.4 Å, while no significant Y–Y metallic bond character is discerned in this analysis. Therefore, EXAFS fitting characterizes sixfold Y SAC coordination, in contrast to common four-fold transition metal ligand complexes such as Fe–N₄. Contrasting with these four-fold coordinated complexes and inert Y/Sc-based NPs, six-fold coordinated Y and Sc SACs were particularly capable of metal atomization during NRR, linking the control of ligand complex coordination to tuned “rare-earth” SAC activity.^[129]

4.8. Ligand Coordinated Complexes: Co-based SACs

Wu et al.^[41] synthesized Co SACs forming Co–N₄ ligand complexes on N-doped Hollow Carbon Spheres (CoSA/N-HCS). Figure 17a depicts CoSA/N-HCS XANES spectra referenced to Co foil, CoO, and Co_3O_4 , resolving an overall Co atom valence state between 0 and 2+ in studied samples. Figure 17b displays matching *k*³-weighted extended FT-EXAFS spectra with solely a primary peak (1.65 Å), which can be connected to the atomic Co coordination shell. Given no secondary peaks implying Co–Co

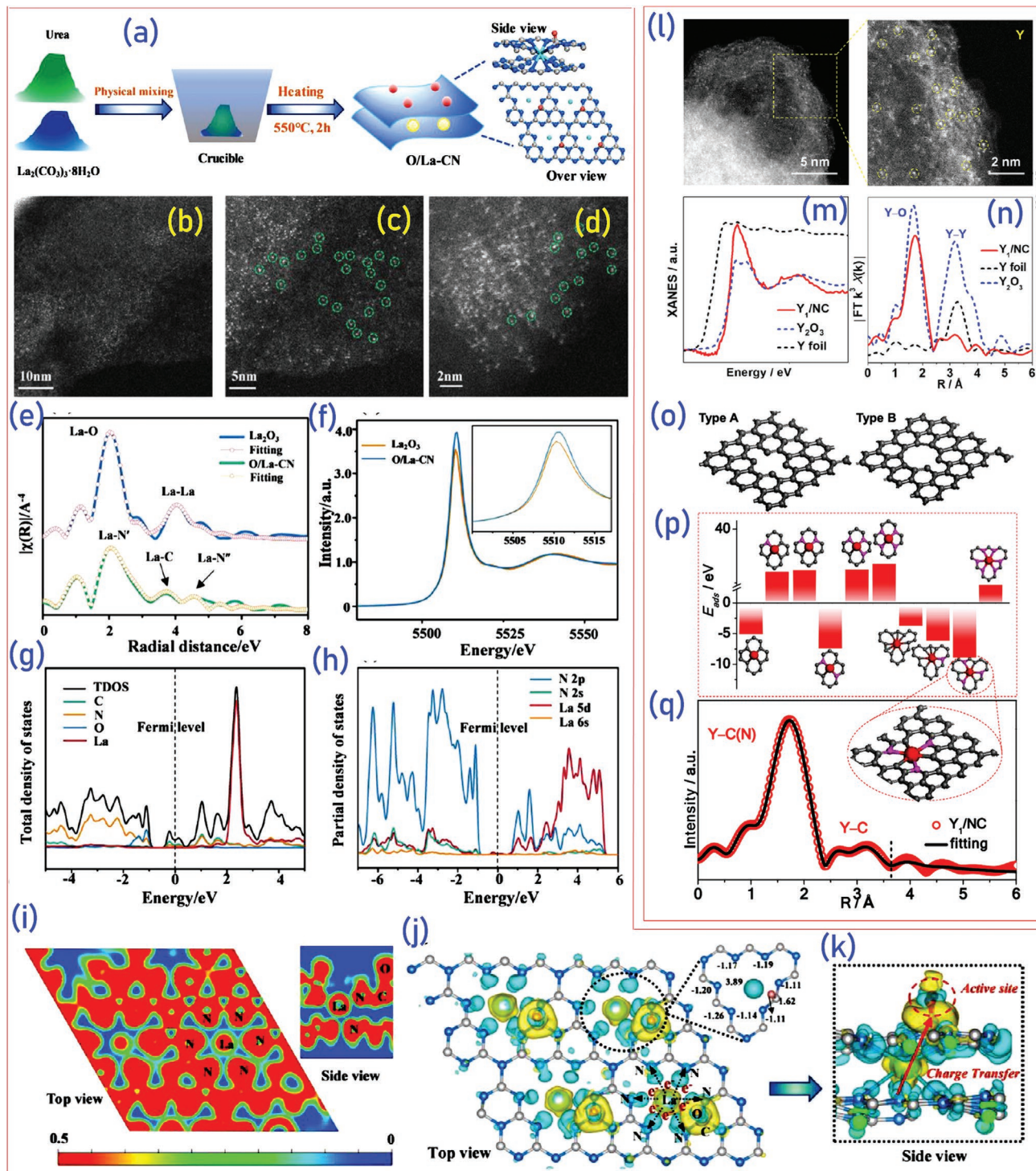


Figure 16. a) Heuristic depiction of O/La-CN SAC synthesis procedure with b-d) spherical AC HAADF-STEM images of catalyst. e) Spectra of k^2 -weighted FT-EXAFS for La_2O_3 and O/La-CN in real space with matching f) normalized XANES spectra at the La L₃-edge. g) Total simulated density of states and compositional orbital distributions of each element with corresponding h) atomic projected partial density of states for N 2s, N 2p, La 6s, and La 5d orbitals of simulated O/La-CN. i) Accompanying electronic location function with j) top and k) side views of differential charge densities (blue/yellow densities = charge accumulation/loss). Inset image depicts calculated atomic Bader charges (positive/negative values = charge accumulation/loss). Atomic models represent C (grey), N (blue), O (red), and La (green) atoms. Adapted with permission.^[128] Copyright 2020, American Chemical Society. l) HAADF-STEM images, m) Y K-edge XANES spectra, and n) k^2 -weighted FT-EXAFS spectra images of Y_1/NC referenced to related materials. o) Simulated type A (left) and B (right) substrates with p) relaxed structures containing Y SAC active sites and matching adsorption energies. q) FT-EXAFS fitting of Y_1/NC in real space with marked fitting limit (3.6 Å, dashed line), applying the most favorable Y-B-N₃ model in (p) (red outline). Visualized simulated models depict C (grey), N (pink), and Y (red) atoms. Adapted with permission.^[129] Copyright 2020, American Chemical Society.

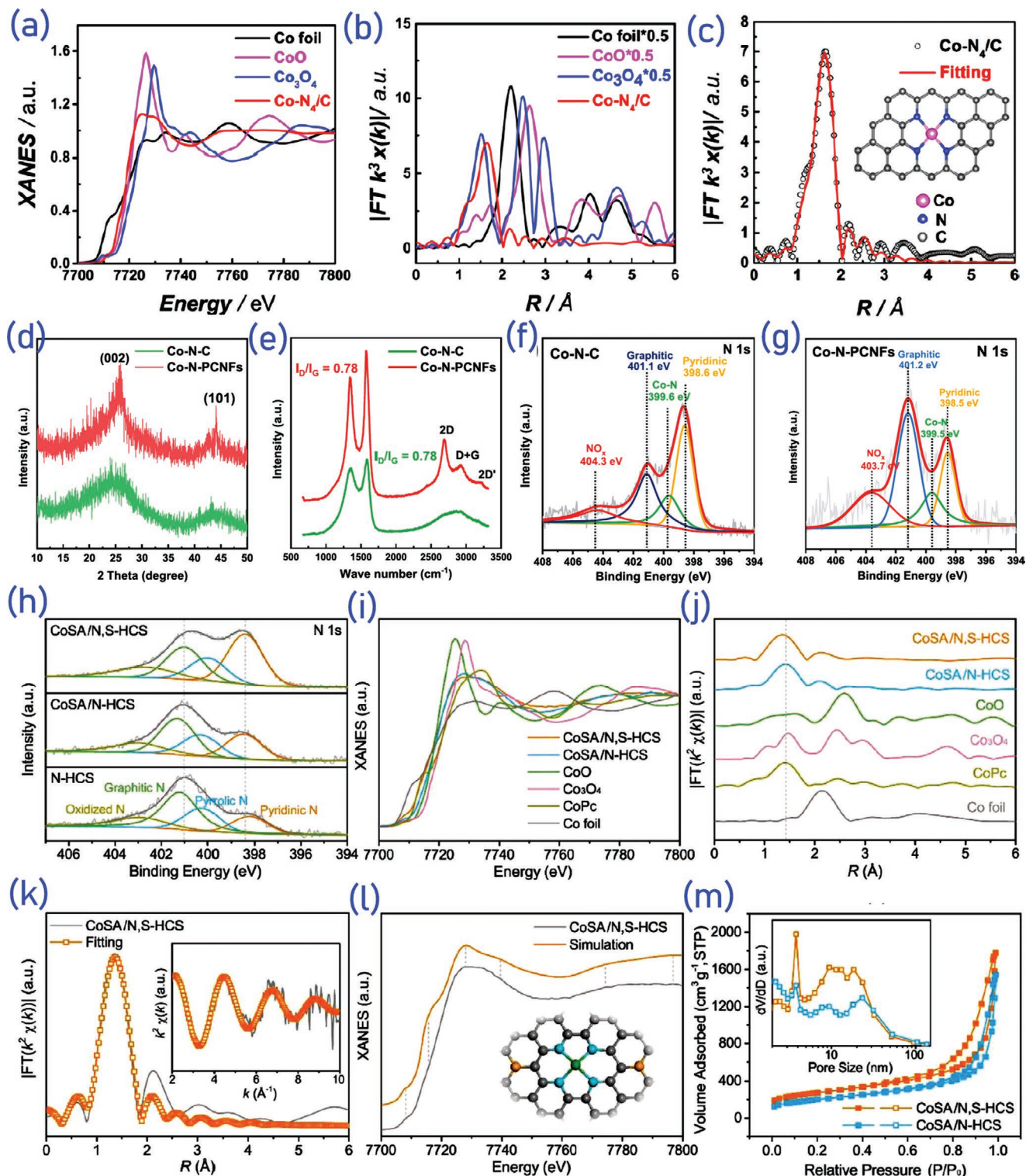


Figure 17. a) XANES spectra with matching b) FT k^3 -weighted Co K-edge spectra of Co-N₄/C, Co foil, CoO, and Co₃O₄ in real space. c) Least-squares EXAFS fitting of Co-N₄/C with schematic depiction of ligand complexes in the carbon framework (inset). Adapted with permission.^[41] Copyright 2020, American Chemical Society. d) XRD, e) Raman, and f,g) XPS N 1s analyses of Co-N-C and Co-N-PCNF catalysts. Adapted with permission.^[105] Copyright 2020, Wiley-VCH Verlag GmbH & Co. KGaA, Weinheim. h) XPS N 1s high-resolution spectra of N-HCS, CoSA/N-HCS, and CoSA/N,S-HCS. i) XANES (normalized) and j) k^2 -weighted Fourier transformed Co K-edge EXAFS spectra of CoSA/N-HCS and CoSA/N,S-HCS, with references. k) Matching EXAFS fits CoSA/N,S-HCS in R space, with inset displaying fit in (reciprocal) k-space. l) Simulated Co K-edge XANES of CoSA/N,S-HCS, with inset visualizing a CoSA/N,S-HCS atomic interface model. m) CoSA/N-HCS and CoSA/N,S-HCS N₂ adsorption-desorption isotherms, with inset depicting matching pore size distributions. Adapted with permission.^[103] Copyright 2020, Wiley-VCH Verlag GmbH & Co. KGaA, Weinheim.

bonding were present ($\approx 2.17 \text{ \AA}$), anchored Co atom aggregation was evidently absent. Figure 17c portrays fitted least squares EXAFS, resolving an overall Co active site coordination number (4) and a mean Co–N bond length (1.98 \AA). Such structural results confirm the coordination environment and chemical state of these Co–N₄ ligand complexes can be consistently calculated across literature.^[134] High performance Co–N–C based cathodes were synthesized by He et al.^[105] via electrospinning, forming ligand complexes anchored to interconnected, hierarchical, porous, 3D carbon nanofiber networks. XRD patterns in Figure 17d portray two peaks linked to (002) and (101) planes with either amorphous C or PCNF supporting Co–N ligand complexes, inferring significant graphitic carbon domains in both samples. The particular peak sharpness of Co–N–PCNF catalysts correlates with improved graphitization, as is confirmed via Raman spectra in Figure 17e. Co–N–PCNF peaks at approximately 1587 and 1337 cm^{-1} respectively correspond to G and D graphite diffraction bands, while comparisons between the D/G diffraction peak intensity ratios of Co–N–C versus Co–N–PCNF (0.88 vs 0.78) further imply greater graphitization in Co–N–PCNF. More extensive graphitic structural ordering in Co–N–PCNF catalysts is also indicated by sharp peaks within the $2500\text{--}3500 \text{ cm}^{-1}$ region of Figure 17e. PVP/PAN and Zn/Co ratio optimization strongly influences graphite formation in Co–N–PCNF samples, particularly PAN proportion due to the sacrificial function and lower carbon yield of PVP polymer during Co–N–PCNF formation. Figures 17f,g respectively depict N 1s peak XPS measurements of Co–N–C (amorphous supports) and Co–N–PCNF samples, highlighting pyridinic N (398.5 eV), graphitic N (401.2 eV), oxidized N (403.5 eV), and Co–N (399.5 eV) – or N coordinated with SAC Co site – bonding. Relative peak intensities indicate Co–N–PCNF has relatively higher graphitic N versus pyridinic N content relative to Co–N–C catalysts, while Figure 17d also indicates no crystalline Co–Co bonding affecting further SAC graphitization. Holding other variations constant, the coincidence of increased PAN proportion and N graphitization in Co–N–PCNF versus Co–N–C samples implied the former induced the latter. Thus, the careful selection of PVP/PAN and Zn/Co proportions enables the localized graphitization of N, as well as C coordinated with such N, but not entire Co–N₄ ligand complexes or hierarchical porous supports, as this would substantially reduce catalyst stability.

Zhang et al.^[103] prepared multifunctional SACs via anchoring uniformly distributed Co atoms on N and S co-doped hollow carbon spheres (CoSA/N,S-HCS), regulating Co active center electronic structure through short-range N coordination and long-range S interactions. Figure 17h deconvolutes high-resolution N 1s XPS spectra into four peaks representing different N bond types, labelled as pyridinic, pyrrolic, graphitic, and oxidized interactions. Over compared S co-doped (N,S-HCS) and solely N-doped (N-HCS) samples, the strongest pyridinic N 1s peak of N,S-HCS is shifted upward ($\approx 0.3 \text{ eV}$) relative to a N-HCS reference, inferring N,S-HCS Co atoms are more strongly bonded to pyridinic N. In contrast, the graphitic N peak of N,S-HCS is shifted down by $\approx 0.3 \text{ eV}$ versus that of N-HCS, implying compensatory electronic transfer from S. XANES spectra in Figure 17i reveal the Co adsorption N,S-HCS K-edge is situated between those of CoO and Co foil, evidencing a corresponding Co valence state between 0 and 2+. This N,S-

HCS absorption edge is also shifted down by $\approx 1 \text{ eV}$ relative to its N-HCS (sulfur-free) reference, further substantiating the claim that p-type doped S donate electrons.^[135] Figure 17j shows how k^2 -weighted Fourier Transformed (FT) EXAFS spectra of CoSA/N,S-HCS have just one prominent peak (1.36 \AA) mirroring the Co–N first coordination shell,^[137] while a smaller peak ($\approx 2.11 \text{ \AA}$) in both N-HCS and N,S-HCS samples resembles that of Co–Co bonding ($\approx 2.15 \text{ \AA}$). The prominent N,S-HCS peak is shifted downward by 0.05 \AA relative to the matching N-HCS peak (1.41 \AA), which appears to result from S dopants. Though structurally correlated with difficulty, the small peak is observed in other Co SACs^[136] and can be attributed to adjacent uniformly dispersed Co atoms. Figure 17k features quantitative EXAFS fitting at the Co K-edge, extracting structural parameters to imply CoSA/N,S-HCS Co atoms are four-fold coordinated with exclusively N, forming Co–N₄ ligand complexes with no Co–S bonding. Matching Co K-edge XANES simulations in Figure 17l further reconciled experimental N,S-HCS and calculated Co–N₄–S₃ spectra, consistent with the relative adsorption energy favorability of DFT structures featuring N–S bonding. N₂ adsorption–desorption isotherms in Figure 17m portray how N,S-HCS samples have larger pore volumes and specific surface areas ($2.4 \text{ cm}^3 \text{ g}^{-1}$, $957.1 \text{ m}^2 \text{ g}^{-1}$) than matching N-HCS samples ($1.9 \text{ cm}^3 \text{ g}^{-1}$, $712.1 \text{ m}^2 \text{ g}^{-1}$). Abundant active sites are exposed by the hollow porous structure of N,S-HCS, facilitating efficient mass transport in electrochemical reactions involving the Co–N₄–S₃ ligand complexes of these Co-based SACs.^[137]

4.9. Mixing Support Composition and Structure: Ru-Based SACs

Hu et al.^[111] prepared Ru SACs anchored to Amorphous/Crystalline FeCoNi (Ru SAs/AC-FeCoNi) for OER. Figure 12a displays Ru K-edge XANES spectra confirming the invariance of SAC chemical environment throughout OER, implying a constant Ru oxidation state. Figure 18b depicts a proposed OER pathway for catalyst surfaces affirming Ru atoms as OER active sites, which was studied via spin-polarized DFT calculations to justify the strength of studied Ru SAs/AC-FeCoNi OER performance.^[138] M–O^{*} intermediate formation from M–OH^{*} is the rate-limiting step of OER, thus the relative smallness of such a Ru SAs/AC-FeCoNi energy barrier (0.40 eV) versus corresponding Ru SAs/CFeCoNi (0.46 eV) and AC-FeCoNi (0.51 eV) barriers at equilibrium potential can explain higher Ru SAs/AC-FeCoNi OER activity (Figure 18c). These calculation results corroborate experimental activity trends, reconciling simulation energetics and mechanisms to better understand experimental outcomes. Synthesizing Ru SAC CoFe bimetallic alloy supports encapsulated in graphitic carbon (G), Lee et al.^[113] aspired to minimize overpotentials for O generating reaction steps in OER. The Co and Fe K-edge XANES spectra of CoFe₂/G and Ru_{SAs}CoFe₂/G mirrored that of Ru metal foil, implying CoFe supports are strongly metallic. Figure 18d depicts related fitted Ru FT EXAFS measurements, revealing Ru_{SAs}CoFe₂/G has a strong, nearest neighbor Ru–Co/Fe bond peak ($\approx 2.17 \text{ \AA}$) without the nearest neighbor Ru–Ru peaks observed in Ru foil ($\approx 2.4 \text{ \AA}$) and RuO₂ ($\approx 3.1 \text{ \AA}$). Beyond affirming the isolated local environment of active centers in these Ru SACs, these FT EXAFS results also demonstrated a non-negligible peak ($\approx 1.6 \text{ \AA}$)

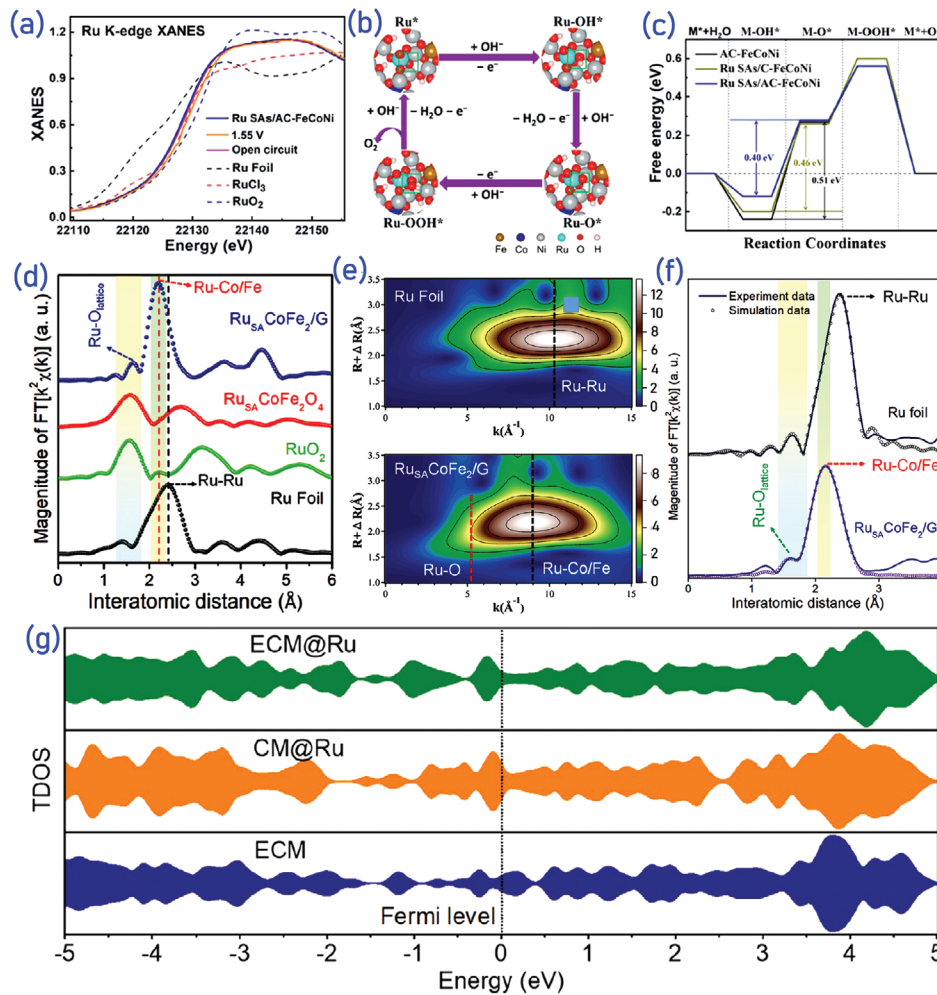


Figure 18. Ru SAs/AC-FeCoNi a) Ru K-edge XANES spectra and b) OER pathway simulated via DFT+U. c) Gibbs free energy calculations at equilibrium potential for Ru SAs/AC-FeCoNi, AC-FeCoNi, and Ru SAs/C-FeCoNi. Adapted with permission.^[111] Copyright 2020, Wiley-VCH Verlag GmbH & Co. KGaA, Weinheim. Ru K-edge d) FT EXAFS spectra for Ru foil, Ru_{SA}CoFe₂/G, Ru_{SA}CoFe₂O₄, and RuO₂, with matching e) WT EXAFS of both Ru foil and Ru_{SA}CoFe₂/G and f) EXAFS fitting curves for Ru_{SA}CoFe₂/G and Ru foil in R space. Adapted with permission.^[113] Copyright 2020, Royal Society of Chemistry. g) TDOS simulated for ECM@Ru, CM@Ru, and ECM. Adapted with permission.^[139] Copyright 2020, Wiley-VCH Verlag GmbH & Co. KGaA, Weinheim.

consistent with Ru–O_{lattice} bonding, further substantiating the absence of Ru metal NPs or related structure formation. To explicitly identify elements with similar coordination relative to Ru SAC environments, Figure 18e applied wavelet transform (WT) EXAFS to confirm Ru–Ru bonding – and thus Ru clusters and NPs – was absent from Ru_{SA}CoFe₂/G. Referencing Ru–Ru bonding to Ru foil, Ru_{SA}CoFe₂/G observed a maximum spectrum intensity ($\approx 9.1 \text{ \AA}^{-1}$) linked to Ru–Co/Fe bonding, while a slight Ru–O WT signal (5.2 \AA^{-1}) agreed with Ru–O_{lattice} FT EXAFS results. Ru K-edge EXAFS fitting shown in Figure 18f resolved Ru atomic coordination with Co (6.5), Fe (6.4), and O_{lattice} (0.2) atoms to further confirm Ru SAC isolation, primary bonding to Co–Fe alloys, and the pre-adsorption of surface O. Thus, combining advanced electronic structure experimental characterization methods can not only describe local SAC chemical environments structurally, but also provide information on their compositions and the implied mechanistic significance (lattice vs surface) of studied structures.

Zhang et al.^[139] synthesized isolated Ru SACs in an edge-rich carbon matrix (ECM@Ru) for electrocatalytic HER. Such SACs were compared to separate ECM and edge-free Ru SACs (CM@Ru) in controlled experiments. Initial DFT Gibbs free energy calculations found H* adsorption on ECM@Ru (-0.09 eV) and CM@Ru (-0.29 eV) to be more favorable than on ECM ($+1.41 \text{ eV}$), implying that mechanisms involving both H* adsorption and desorption effectively require Ru SACs to occur and that Ru–H* bonding is responsible for such improved favorability. Further DFT calculations resolved the total density of states (TDOS) of simulated ECM@Ru, ECM, and CM@Ru in Figure 18g, particularly focusing on the valence band maxima (VBM) and conduction band minima (CBM) of their electronic structures to verify their HER Ru active sites and discern their electron donating and accepting mechanisms.^[140] Ru-decorated (ECM@Ru, CM@Ru) versus Ru-free (ECM, CM) carbon matrix substrates produced distinct TDOS and PDOS profiles, with Ru-decorated systems featuring denser TDOS and

Ru PDOS near the Fermi level.^[105] In contrast, Ru-free systems exhibited higher C 2p and N 2p CBM and VBM peaks, implying Ru-decorated systems observe strong binding and electronic state hybridization between Ru and H*.^[141] Given such hybridization, the effective charge transfer between Ru and H* would enable more favorable H* adsorption energetics, facilitating a mechanism that requires Ru-H* interaction and yields higher electronic conductivity.

5. Applications to Evolution/Reduction Reactions and Batteries

SACs have gained extensive recent attention and are very promising for industrial, environmental, and energy conversion applications driven by metal catalysts. SACs also demonstrate properties that differ from those of more typical analogous nanoparticle catalysts, manifesting their promise for catalytic candidacy. To aide in resolving environmental and energy concerns, molecular H₂ can be sustainably produced via electrochemical water splitting during HER, metal-air battery cathodes and fuel cells can implement ORR, and sequential H and electron transfer mechanisms from water splitting half-reactions and rechargeable metal-air batteries can be harnessed via OER. Moreover, applying CO₂RR can reduce CO₂ emissions and mitigate global energy concerns. SACs have demonstrated outstanding activity and selectivity during CO₂RR, namely when converting CO₂ into CO, formic acid, C₂ products, and other chemicals. SACs have also been successfully implemented as NRR electrocatalysts for NH₃ production and N₂ fixation. Further, SACs have been utilized as excellent cathode materials for ZABs and Li batteries for next generation energy storage systems. For all of the justifications given above, this section will discuss recent developments towards improving catalytic activity and stability of metal-based SACs in different applications.

5.1. Hydrogen Evolution Reaction: Tuning Activity, Current Density, and Stability

Zang et al.^[142] yielded single atom Ni supported on N-doped graphitic carbon (*g*-C₃N₄), yielding catalysts (Ni-SA/NC) for HER applications in alkaline freshwater compared with analogous Ni NP (Ni-NP/NC) and solely substrate (NC) controls. HER performance (current density = 10 mA cm⁻²) was first characterized in 1 M KOH freshwater (pH = 13.8) through LSV curves via Figure 19a, revealing Ni-SA/NC observes a lower HER overpotential (102 mV) than Ni-NP/NC (120 mV) and NC (215 mV). More specific to industrial applications, Ni-SA/NC also needs significantly lower overpotentials to reach larger current densities (346 mV at 200 mA cm⁻², 421 mV at 300 mA cm⁻²) than conventional Pt/C (403 mV at 200 mA cm⁻², 580 mV at 300 mA cm⁻²) catalysts (Figure 19b). Figure 19c resolves the Tafel slopes of Ni-SA/NC (120 mV dec⁻¹), Ni-NP/NC (188 mV dec⁻¹), and NC (139 mV dec⁻¹), additionally validating the more favorable HER activity of Ni-SA/NC. Ni-SA/NC mass activities of 19.4 and 105 A g⁻¹ at respective overpotentials of 100 and 200 mA cm⁻² were also higher than compared reference

catalysts. Through DFT investigations of reaction mechanisms depicting OH adsorption, these tuned high current densities and resultant HER activities were attributable to the proportions of Ni-N₃-O₂ defective oxidized and Ni-N₄ ligand complex active sites accessible on Ni-SA/NC catalysts.

Ru single atom alloy (Ru SAA) catalysts prepared by Chen et al.^[143] were applied to HER, emphasizing catalytic performance maximization in alkaline 1 M KOH. Figure 19d illustrates that RuAu_{0.2}, resolved to be the most active Au composition tested via HER, observes a turnover frequency (TOF = 2.18 s⁻¹ at overpotential = 50 mV) higher than Pt/C (3.0×) and Ru/C (3.6×). Figure 19e depicts long-term RuAu_{0.2} electrocatalytic stability with cycling, finding its overpotential negligibly increases (\approx 2 mV) after 1000 HER cycles relative to Pt/C (\approx 10 mV). Chronoamperometry testing in Figure 19f further validated RuAu_{0.2} chemical stability over 10 h of continuous testing, achieving small catalytic current density decreases (\approx 8%) and maintaining 100% Faradaic yield to confirm correlation between produced current and HER activity. Overall, the synergistic functions of Ru – which captures and splits H₂O – and Au – which adsorbs H and promotes H₂ formation – enable alloy composition engineering to optimally tune exhibited catalytic activities, current densities, and stabilities in RuAu SAAs (Table 1).

Zhang et al.^[139] prepared edge-rich (ECM@Ru) and edge-free (CM@Ru) carbon matrices decorated with Ru SACs, calculating their mass activities as the ratios of current density (specifying overpotential) and loaded mass catalyst. At overpotentials of 50 and 100 mV, mass activities exhibited by ECM@Ru are respectively \approx 6.4× and \approx 9.6× higher than those of Pt/C-20% and 2.7× and 4.1× higher than those of CM@Ru (Figure 19g). Better ECM@Ru HER performance is further justified by evaluating double-layer capacitance (C_{dl}) during cyclic voltammetry as a surrogate for electrochemically active surface area (ECSA),^[144] achieving distinctly higher C_{dl} for ECM@Ru (1.08 mF cm⁻²) than CM@Ru (0.27 mF cm⁻²) in Figure 19h. Electrochemical impedance spectroscopy (EIS) measurements generating Nyquist plots (Figure 19i) explain charge transfer kinetics, with fitted results calculating lower charge transfer resistance in ECM@Ru than CM@Ru. Figure 19h,i respectively imply that enhanced ECSA forms more ECM defects containing HER active sites, and that carbon matrix edges are responsible for electron transfer during HER.^[145] Thus, ECM@Ru electrocatalyst activity tuning can be governed by controlling carbon matrix support structure. Zhu et al.^[146] developed Single Atom Pt decorated, variably layered VS₂ NSs grown on carbon paper (Pt/VS₂/CP) for HER performance, with Pt concentration controlled by chloroplatinic acid concentration (*x*-Pt, in mM) during synthesis. Figure 19j depicts how Pt SACs affect Pt/VS₂/CP HER activity by comparing Pt/VS₂/CP LSV curves with those of pristine carbon paper (CP), VS₂/CP, 20% Pt/C, and Pt/VS₂/CP, immediately corroborating previous literature by finding that pristine CP is nearly inactive.^[147] Though 20% Pt/C exhibits much higher activity than VS₂/CP, adding modest Pt concentrations (up to 1-Pt/VS₂/CP) continuously improves Pt/VS₂/CP activity towards that of Pt/C, albeit with diminishing marginal returns from 1-Pt/VS₂/CP to 10-Pt/VS₂/CP due to Pt SAC aggregation and clustering. Correspondingly, adding 0.1, 0.5, and 1-Pt concentrations to VS₂/CP respectively reduces overpotential from 257 to 122, 94, and 77 mV (current density

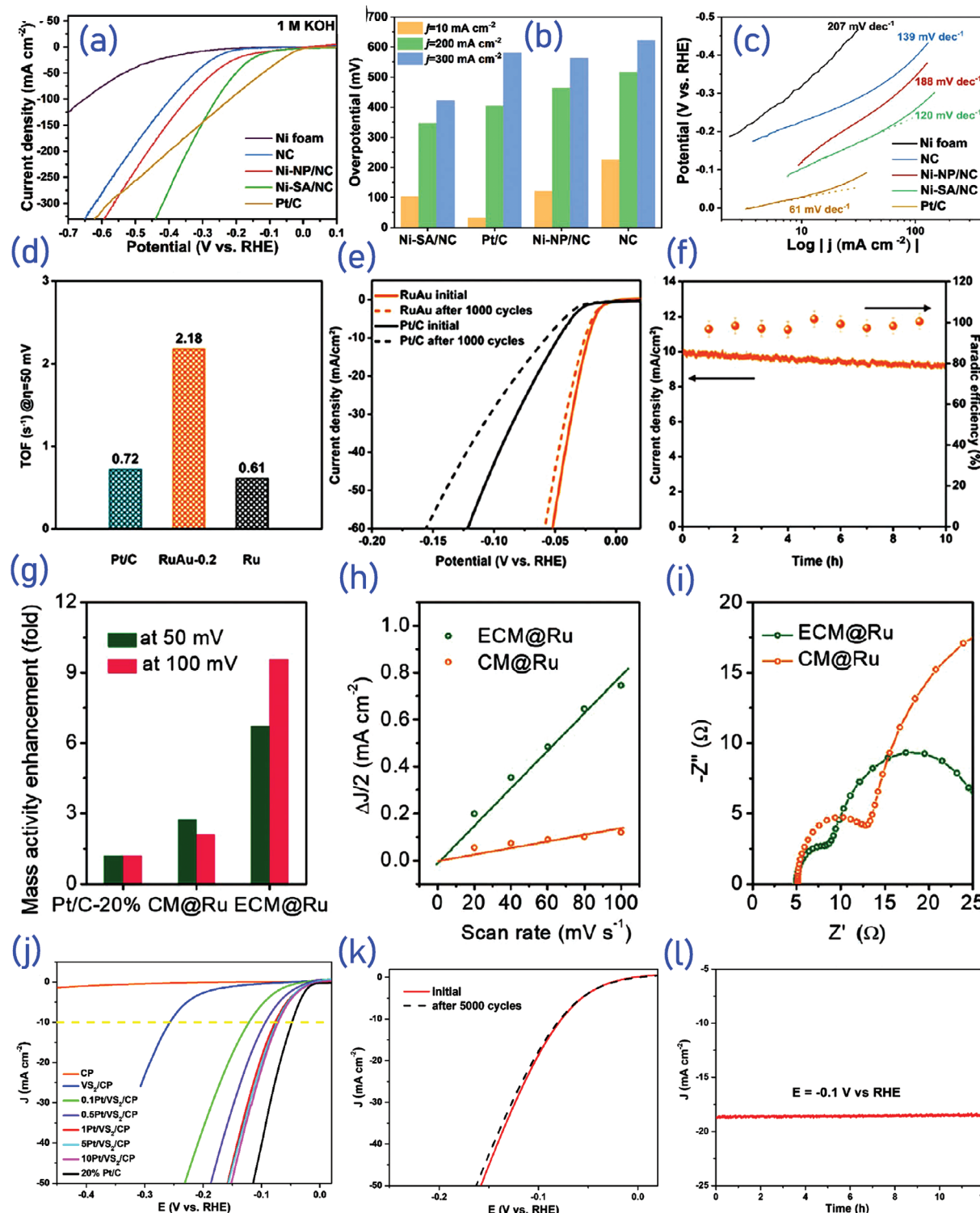


Figure 19. a) LSV curves, b) overpotential comparisons, and c) Tafel plots of Ni-SA/NC, NC, and Ni-NP/NC in N₂-saturated KOH freshwater (1 M) electrolytes (25 °C, 5 mV s⁻¹ scan rate) during HER. Adapted with permission.^[142] Copyright 2020, Wiley-VCH Verlag GmbH & Co. KGaA, Weinheim. d) TOF measurements (overpotential = 50 mV), e) durability tests, and f) chronoamperometric curves (10 mV overpotential, left) and efficiency (FE, right) of RuAu-0.2, Pt/C, and Ru (1 M KOH) during HER. Adapted with permission.^[143] Copyright 2019, Wiley-VCH Verlag GmbH & Co. KGaA, Weinheim. g) Mass activities at different overpotentials, h) capacitive $\Delta J/2$ versus scan rate, and i) Nyquist plots of ECM@Ru and CM@Ru in H₂SO₄ (0.5 M) during HER. Adapted with permission.^[139] Copyright 2020, Wiley-VCH Verlag GmbH & Co. KGaA, Weinheim. j) CP, VS₂/CP, Pt/VS₂/CP (0.1-, 0.5-, 1-, 5-, and 10-), and 20% Pt/C LSV curves. k,l) Long-term 1-Pt/VS₂/CP stability test with k) polarization curves (-0.65–0.05 V vs RHE, 5000 cycles) and l) time-dependent current density curve (-0.1 V vs RHE, 12 h) during HER. Adapted with permission.^[146] Copyright 2020, American Chemical Society.

Table 1. HER performances of SACs based on recent literature.

Electrocatalyst	Overpotentials at 10 mA/cm ² (Activities)	Stabilities	Medium	Reference
K ₂ PtCl ₆ @NC-M	11 mV	Insignificant decrease after 40 h	0.5 M H ₂ SO ₄	[148]
Edge-rich-Co single atoms	59 mV	No detectable loss even after 480 h	1.0 M KOH	[149]
W-SAC	85 mV	No appreciable activity degradation after 10 000 CV cycles	0.1 M KOH	[150]
Ni ₅ P ₄ -Ru	54 mV	Stability maintained even after a consecutive test over 5 days	1.0 M KOH	[59]
SA Pt-decorated VS ₂	77 mV	Quite stable after 12 h	0.5 M H ₂ SO ₄	[146]
Mo SAs/ML-MoS ₂	107 mV	Excellent stability	0.5 M H ₂ SO ₄	[151]
ECM@Ru	63 mV	No obvious change even after 20 h	0.5 M H ₂ SO ₄	[139]
Pt ₁ /N-C	19 mV	No detectable loss even after 20 h	0.5 M H ₂ SO ₄	[152]
Co@CoSA/N-CNT/CC	78 mV	Excellent stability, >50 h	0.5 M H ₂ SO ₄	[153]
RuAu SAA	24 mV	After 10 h testing, catalytic stability slightly drops by 8%.	1 M KOH	[143]

of 10 mA cm⁻²), though contributing 5 and 10 nm Pt only further lowers overpotential to 75 and 73 mV. Figure 19k,l finds stable, long-term 1-Pt/VS₂/CP polarization only reduces slightly over 5000 sweeps, with mirrored stable current density (overpotential = 100 mV) over 12 h (Table 1). Pt-VS₂ binding strength was ultimately claimed responsible for tuning multifunctional Pt/VS₂/CP catalyst activity and durability, as Pt reduced the H adsorption energetics and VS₂ NSs provided the stable supports needed to tune current density and stability. HER performances of different SACs are summarized in Table 1.

5.2. Carbon Dioxide Reduction Reaction: Tuning Active Sites, Charge, and Selectivity

Xiong et al.^[154] synthesized weight proportioned (*x*) Ni Single Atom catalysts on defect-rich ZrO₂ supports (Ni-SA-*x*/ZrO₂) via a sol-gel method, comparing them to pristine (*p*-ZrO₂) and defective (*d*-ZrO₂) zirconia. Figure 20a demonstrates that though *d*-ZrO₂ CO formation rates (2.0 μmol g⁻¹·h) outperform those of *p*-ZrO₂ (0.3 μmol g⁻¹·h), Ni SACs maximize photocatalytic activity via Ni-SA-5/ZrO₂ (11.8 μmol g⁻¹·h), which has proportionally greater CO production than Ni-SA-2/ZrO₂ (1.8×) and NiO-5/ZrO₂ (3.5×) references. Ni atomic aggregation decreased CO formation for more highly concentrated Ni-SA-8/ZrO₂ with respect to Ni-SA-5/ZrO₂, while O₂ contributions to all formation measurements were precluded by N₂ presence. Figure 20b indicates CO formation selectivity is stronger for Ni-SA-5/ZrO₂ (92.5%) than Ni-SA-2/ZrO₂ (78.7%), Ni-SA-8/ZrO₂ (77.4%), NiO-5/ZrO₂ (67.7%), *d*-ZrO₂ (66.6%), and *p*-ZrO₂ (36.4%), while Ni-SA-5/ZrO₂ also does not need sacrificial agents or sensitizers during reaction. Pure Ar atmosphere controlled experiments observed no CO evolution, verifying CO₂ reactants were responsible for CO products. Therefore, SAC activity can be optimized against the trade-off between active site concentration and aggregation when producing CO during CO₂RR.

Liu et al.^[129] synthesized “rare-earth”, N-doped Carbon supported Sc (Sc₁/NC) and Y (Y₁/NC) SACs for CO₂RR, designing SACs under the trade-off between multifunctionally tuned activity and stability measures. Figure 20c depicts Y₁/NC and Sc₁/NC LSV curves during CO₂RR, confirming current densities are higher in CO₂-saturated than Ar-saturated electrolytes, Y₂O₃

and Sc₂O₃ are not active, and solely H₂ and CO are produced during reaction. Applying these resolved conditions, Figure 20d resolves Faradaic Efficiency (FE) maxima for Y₁/NC (88.3%, -0.58 V vs RHE) and Sc₁/NC (81.3%, -0.68 V vs RHE) CO production at higher voltages. However, Figure 20e shows elevated CO production partial current densities (*j*_{CO}) are produced at lower voltages (-0.78 V vs RHE), as competitive HER interferes with CO₂RR at higher voltages. Continuous CO₂RR completed at an activity optimum (-0.68 V vs RHE) for 12 h revealed negligible current density decay and LSV curve changes in Figure 20f, confirming Sc₁/NC and Y₁/NC stability and efficiency are achieved at similar optima. Nevertheless, competing demands for stability and efficiency versus current density and activity (Table 2) still produce a trade-off for these tuned SACs.

Feng et al.^[155] embedded Mn-N₃ SACs in *g*-C₃N₄ on Carbon Nanotubes (Mn-C₃N₄/CNT), testing Mn-N₃ active site CO₂RR performance in CO₂-saturated 0.5 M KHCO₃ against Mn₃O₄/CNT and carbon cloth (C₃N₄/CNT) controls. Figure 20g displays higher LSV onset potentials and current densities for Mn-C₃N₄/CNT than tested controls, consistent with complementary partial CO current density comparisons in Figure 20h contrasting Mn-C₃N₄/CNT (*j*_{CO} = 14.0 mA cm⁻² at -0.55 V, maximum *j*_{CO} = 22.4 mA cm⁻² at -0.75 V) against C₃N₄/CNT and Mn₃O₄/CNT (*j*_{CO} < 5 mA cm⁻²). Figure 20i confirmed the stability of Mn-C₃N₄/CNT during 20 h of CO₂RR, yielding marginal decreases in CO production efficiency (FE_{CO}) and current density. Ultimately, lowered COOH* intermediate adsorption energetics due to Mn-N₃ active center exposure was found responsible for optimizing current density with applied potential, and was ultimately correlated to interfacial charge transfer improvements that could be modulated with substrate choice. Ni et al.^[156] synthesized Defect-rich N-doped Graphene-like porous carbon housing Single Atom Fe SACs (DNG-SAFe), determining how intrinsic defects anchor Fe-N₄ active sites versus relatively intrinsic defect-free analogues (NG-SAFe) during CO₂RR. Potentiostatic electrolysis in an H-type cell filled with CO₂-saturated 0.1 M KHCO₃ yielded only gaseous H₂ and CO, with DNG-SAFe selectively producing CO (FE_{CO} = 90% over -0.75 and -0.85 V) versus NG-SAFe (FE_{CO} = 40% at the same potentials) in Figure 20j. Figure 20k confirms long-term stability (20 h, -0.75 V vs RHE) of DNG-SAFe current density (17.0 mA cm⁻²) and efficiency (FE_{CO} = 87–94%).

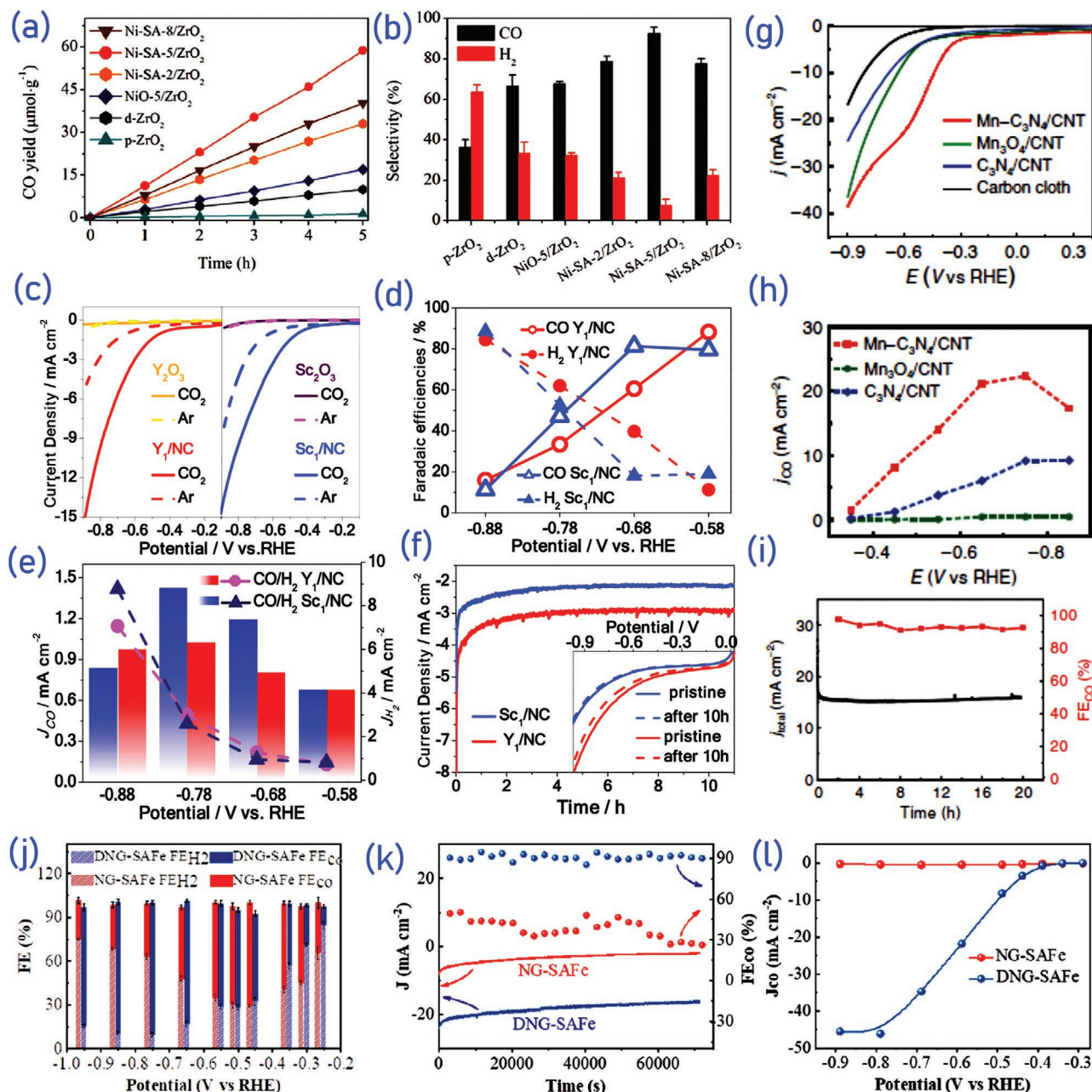


Figure 20. a) CO yield versus reaction time and b) H₂/CO selectivity of Ni-SA-8/ZrO₂, Ni-SA-5/ZrO₂, Ni-SA-2/ZrO₂, NiO-5/ZrO₂, d-ZrO₂, and p-ZrO₂ with 0.08 MPa humidified CO₂, full spectrum irradiation, and 10 mg catalyst during 5 h photocatalytic CO₂ reduction. Adapted with permission.^[154] Copyright 2020, Wiley-VCH Verlag GmbH & Co. KGaA, Weinheim. c) LSV curves, d) CO (empty) and H₂ (filled) efficiencies (FE) over varied potentials, e) H₂ (line + symbol) and CO (column) generation related partial current densities, and f) time-dependent currents (-0.68 V vs RHE, 12 h) with paired LSV curves of Y₁/NC, Y₂O₃, Sc₁/NC, and Sc₂O₃ in CO₂-saturated KHCO₃ (0.5 M) during CO₂RR. Adapted with permission.^[129] Copyright 2020, American Chemical Society. g) LSV curves, h) j_{CO} over varied applied potentials, and i) long-term durability tests (-0.55 V vs RHE, 20 h) of Mn-C₃N₄/CNT, C₃N₄/CNT, and Mn₃O₄/CNT in CO₂-saturated KHCO₃ electrolyte (pH = 7.33, temperature = 25 ± 3 °C, no stirring) during CO₂RR. Adapted with permission.^[155] Copyright 2020, Springer Nature. j) Efficiencies (FE) of H₂ and CO over varied applied potentials, k) long-term stability tests (-0.75 V vs RHE), and l) j_{CO} over varied applied potentials for NG-SAFE and DNG-SAFE in KHCO₃ (0.1 M). Adapted with permission.^[156] Copyright 2020, Wiley-VCH Verlag GmbH & Co. KGaA, Weinheim.

Through Figure 20l, DNG-SAFE and NG-SAFE CO₂RR performances were additionally tested in isolated 1 M KHCO₃ to emulate desaturating CO₂ reduction within Zn–CO₂. Yielded DNG-SAFE partial CO current densities (j_{CO} = 46.2 mA cm⁻² at -0.79 V) were high relative to controls, consistent with their

measured current densities and FE_{CO} (Table 2) but unexpected by the accelerated OER anticipated in defective carbon supports.^[157] Improved selective CO generation during CO₂RR, in addition to averted HER and OER product formation, was attributed to the coupled interactions between Fe-N₄ active

Table 2. CO₂RR performances of SACs based on recent literature.

Electrocatalyst	Maximum FE [%]	Onset Potential [V vs RHE]	Medium (CO ₂ -saturated)	Reference
Atomically dispersed In-N-C	80	−0.5	0.5 M KHCO ₃	[158]
Atomic Sn δ ⁺ sites	74.3	−0.18	0.5 M KHCO ₃	[159]
Ni(−Cl)−N ₃ O−TPP	80	−0.55	0.5 M KHCO ₃	[160]
Cu SACs/NG	81	−0.33	0.1 M KHCO ₃	[161]
Atomically dispersed Y ₁ /NC and Sc ₁ /NC	88.3 and 81.3	—	0.5 M KHCO ₃	[129]
Fe−N ₄ on graphene	94	—	0.5 M KHCO ₃	[162]
Ni@N ₃	90	−0.4	0.1 M KHCO ₃	[163]
Pd-NC SACs	55	—	0.5 M NaHCO ₃	[164]
Atomic Fe dispersed on NG	80	—	0.1 M KHCO ₃	[165]
SA-Zn/MNC	85	—	1 M KHCO ₃	[61]

centers and intrinsic defect sites, which simultaneously enabled COOH* adsorption and CO* desorption to tune both selectivity and activity CO₂RR performances of different SACs are summarized in Table 2.

5.3. Photocatalytic CO₂ Reduction Reactions: Stable Adaptation to Chemical Environments

Current initiatives towards reducing CO₂ emissions, specifically by encouraging widespread implementation of photocatalysis in the CO₂ reduction reaction (CO₂RR), primarily involve improving catalytic activity, and tuning product selectivity. Similar to analogous electrochemical literature, photocatalytic CO₂RR research aspires to reduce the energetic barriers of CO₂ reduction mechanisms and control the relative activation barriers governing selective product yields. However, recent CO₂RR photocatalysis research has yet to achieve either goal, considering rate-limiting CO₂ dissociation, and competing water-splitting reactions. Given their high concentrations of active sites and modular design, SACs can prospectively improve photocatalytic CO₂RR rates, efficiencies, and selectivities. More specifically, control of the coordination environments of metal active centers enables modular catalyst design via ligand, SAC concentration, and support selection, tuning catalyst charge transfer and preferentially encouraging adsorption and desorption reaction kinetics at pertinent CO₂RR stages.

Chen et al.^[128] synthesized rare-earth La SACs on graphitic carbon nitride (g-C₃N₄) substrates using aqueous La₂(CO₃)₃ (O/La-CN) for CO₂ photocatalytic reduction. Such reactions applied simulated solar light to a CO₂ solvent (acetonitrile/water mixture) and an electron donor (triethanolamine, TEOA), yielding CO, H₂, and CH₄ primary products. Figure 21a,b indicates that during a 5 h photocatalytic reaction on O/La-CN in pure CO₂, predominantly CO (selectivity = 80.3%, rate = 92 μmol g^{−1}·h) and CH₄ (rate = 5.6 μmol g^{−1}·h) are produced with negligible H₂. Performing the same reaction on pure CN supports yields CO at a comparatively low rate (6.8 μmol g^{−1}·h), while O/La-CN selectivity and production rates are higher during CO₂ reduction under similar conditions. Figure 21c depicts multiple experiments in which reaction conditions are controlled. For example, mixing a CO₂ solvent and an electron donor without a light source or photocatalyst yields negligible amounts of CH₄,

which were traced to CO₂ injected into the atmosphere. When substituting environmental CO₂ for Ar gas, H₂ was produced while CO and CH₄ were absent. In combination, these experiments indicate C1 product formation during CO₂ photocatalytic reduction originates from CO₂ gas injection. Also building upon g-C₃N₄ substrates, Cheng et al.^[166] coordinates Ni SACs on porous, multi-layered CN in an unsaturated concentration (Ni₅-CN) optimized for photocatalytic yield via a self-limiting edge confinement synthesis procedure. Figure 21d depicts the photocatalytic CO₂RR yields of Ni₅-CN against experimental controls varying Ni SAC concentration (CN, Ni₁-CN, Ni₁₀-CN), as well as metal center charge and coordination via physically mixed Ni powders (Ni_p+CN) and NiCl₂ (NiCl₂+CN). Specifically, photocatalytic yields of CO and CH₄ for Ni₅-CN (CO: 8.6 μmol g^{−1}, CH₄: 0.5 μmol g^{−1}) strongly outperform those of CN (CO: 1.1 μmol g^{−1}·h, CH₄: 0.1 μmol g^{−1}·h), Ni_p+CN (CO: 2.7 μmol g^{−1}·h, CH₄: 0), and NiCl₂+CN (CO: 3.3 μmol g^{−1}·h, CH₄: 0) during 1 h of CO₂RR. Figure 21e,f confirms that the always dominant CO and usually prevailing CH₄ production of Ni₅-CN persists most saliently when directly impacted by photocatalytic reactions (0–2.5 h), but such production desists afterwards (2.5–4.5 h). Such a result implies photocatalyst deactivation due to surface saturation, which could be resolved by refining the balance between adsorption and desorption kinetics via further modular design of studied Ni SAC ligand complexes.

While evaluating crystalline g-C₃N₄ nanorods supporting Cu SAC photocatalysts (Cu-CCN) with no additional catalytic components, Li et al.^[41] notes strongly efficient CO₂ reduction with high CO selectivity. Figure 21g verifies Cu-CCN yields more CO from photocatalytic NRR (3.086 μmol g^{−1}·h) than corresponding separate crystalline C₃N₄ nanorod (CCN, 1.68 μmol g^{−1}·h) and BCN (bulk g-C₃N₄, 0.895 μmol g^{−1}·h) experimental controls after 1 h, consistent with corresponding results (Figure 21h) resolved over 4.5 h. In contrast, Figure 21i indicates CCN maximizes CH₄ production both in magnitude and relative improvement after 1 h of NRR under illumination. In conjunction, these results imply that only CCN is not impacted by a catalyst deactivation mechanism solely impacting CH₄ production. Given CO₂ was initially adsorbed on all photocatalyst surfaces and most highly concentrated on Cu-CCN before NRR and irradiation, lowered CH₄ or other CO₂ reduction product yields would likely result from rate-limiting energetic barriers involving intermediate

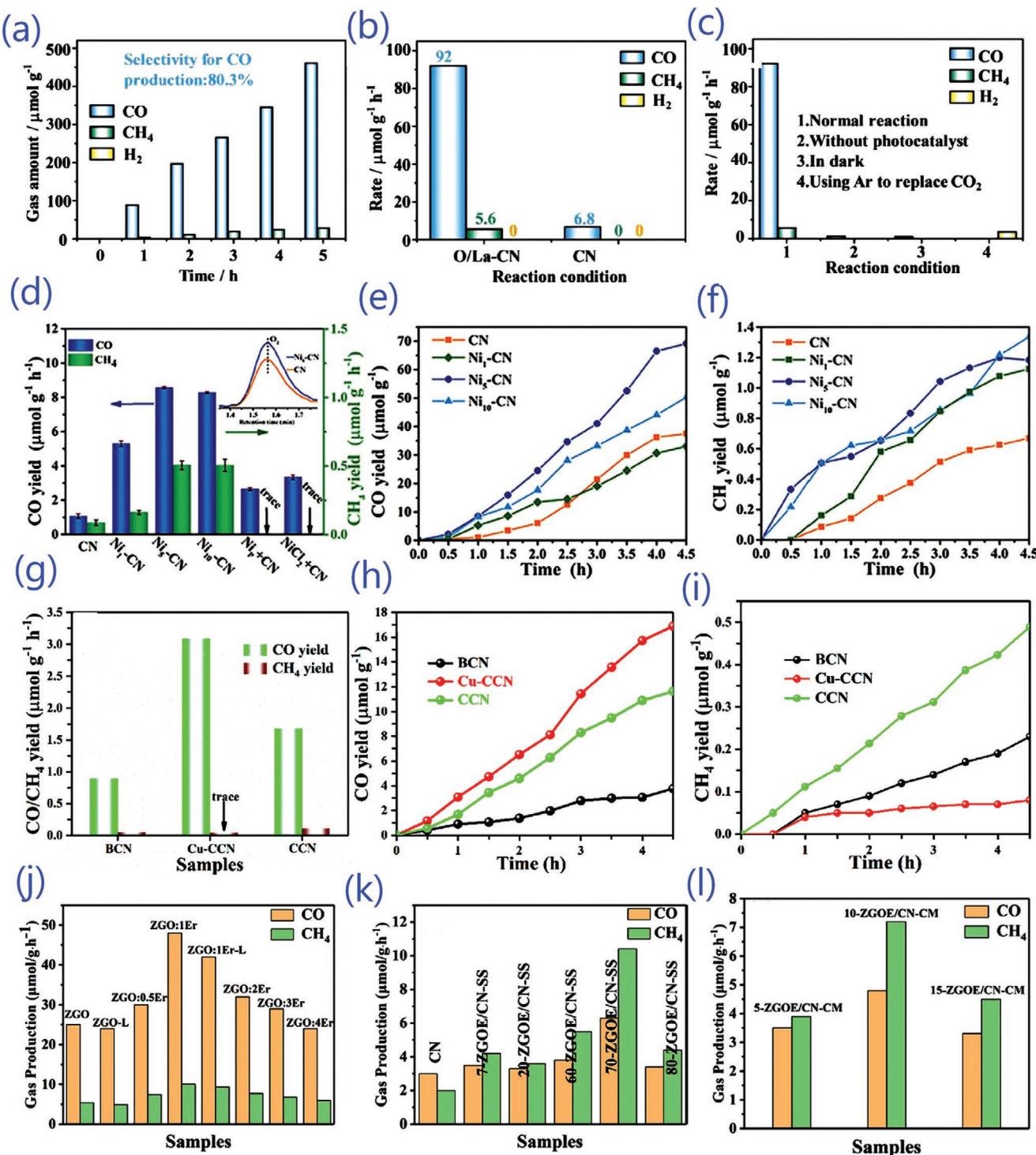


Figure 21. Gaseous concentrations and rates of a) photocatalytic CO_2 reduction and b) photoreduction products, retested c) using multiple experimental controls. Adapted with permission.^[128] Copyright 2020, American Chemical Society. Photocatalytic CO_2 reduction via visible light irradiation, showing yields of d) CO/CH_4 over 1 h, e) CO and f) CH_4 over 4.5 h. $\text{Ni}_s\text{-CN}$ results are referenced to CN, CN with nickel powder ($\text{Ni}_p\text{-CN}$), CN with NiCl_2 ($\text{NiCl}_2\text{+CN}$), $\text{Ni}_r\text{-CN}$, and $\text{Ni}_{10}\text{-CN}$ yields. Adapted with permission.^[166] Copyright 2020, Wiley-VCH Verlag GmbH & Co. KGaA, Weinheim. Cu-CCN, CCN, and BCN product yields during photocatalytic CO_2 reduction and irradiation, displaying those of g) CO/CH_4 over 1 h, h) CO and i) CH_4 over 4.5 h. Adapted with permission.^[47] Copyright 2020, American Chemical Society. CO and CH_4 production of j) ZGO:xEr (UV light), k) CN and ZGOE/CN-SS (visible light), and l) ZGOE/CN-CM (visible light). Adapted with permission.^[167] Copyright 2021, Wiley-VCH Verlag GmbH & Co. KGaA, Weinheim.

states. For Cu-CCN and CCN photocatalysts, adsorbed CO₂ readily became HCO₃⁻ upon adsorption, though HCO₃⁻ could only be sufficiently consumed for CO generation by Cu-CCN after 1 h of irradiation. HCOO⁻ intermediates result from such HCO₃⁻ consumption and strongly favor CO desorption kinetics versus those of CH₄, preferentially producing even more CO. Therefore, the relative energetic favorability of CO desorption on CCN based photocatalysts, combined with the relative mechanistic accessibility of necessary reaction intermediates only in Cu-CCN, is responsible for improving both CO catalytic reactivity and selectivity. In evaluating how to tune photocatalytic charge transfer during CO₂ reduction, Er³⁺ SACs within Zn₂GeO₄/g-C₃N₄ (ZGO/CN) based heterojunctions were studied by Han et al.,^[167] namely with controls varying Er³⁺ SAC concentration and substituting ZGO/CN composite components with different support architectures. Figure 21j depicts how Er concentration impacts photocatalytic CO and CH₄ generation in unsupported ZGO:*x*Er during UV irradiated CO₂ reduction over 6 h, yielding modest CO (25 μmol g⁻¹·h) and CH₄ (5.4 μmol g⁻¹·h) in pure ZGO (*x* = 0) and maximized CO (48 μmol g⁻¹·h) and CH₄ (10 μmol g⁻¹·h) in 1 mol% Er³⁺ ZGO (ZGO:1Er). Figure 21k,l portrays photocatalytic yields – namely using the optimized catalyst (ZGOE, or ZGO:1Er) under visible light for 6 h – while varying support architectures, evaluating in situ (ZGOE/CN-SS) and chemisorption (ZGOE/CN-CM) photocatalyst synthesis procedures in conjunction with different ZGOE versus support molar ratios (*x*-ZGOE/CN). CO and CH₄ production were maximized for 70-ZGOE/CN-SS (6.3 and 10.4 μmol g⁻¹·h, respectively) and 10-ZGOE/CN-CM (4.8 and 7.2 μmol g⁻¹·h, respectively), indicating that photocatalytic activity is severely improved with ZGOE addition – relative to pure g-C₃N₄ (3 and 2 μmol g⁻¹·h, respectively) – but that support synthesis procedure and Er³⁺ concentration induce complicated effects on this relationship. Synthesis method was found to impact bonding at ZGOE/CN heterojunctions, which in turn affected Er³⁺ coordination environments at such junctions. Given Er³⁺ 4f orbital overlap with ZGO and CN is responsible for constructing the charge bridges inducing photocatalytic current and ultimately producing CO and CH₄, CO₂RR activity and selectivity can be effectively tuned by changing the synthesis approach dependent coordination environments and concentrations of Er³⁺.

5.4. Nitrogen Reduction Reactions: Promising Strategy for NH₃ Production

Ultimately, one of the most prevalent applications of NRR – which yields NH₃ from N₂ – is the efficient, renewable, and large-scale production of fertilizer. The Haber-Bosch process, currently one of the most common methods implemented for such ammonia production, requires extreme thermodynamic operating conditions, inefficiently consumes energy, and is relatively environmentally unsafe. In contrast, photocatalytic and electrocatalytic NRR applying metal SACs are performed under relatively mild reaction conditions, require comparably small energy inputs, and innately facilitate ergonomic, renewable reactor designs. Therefore, aspirations to replace applications of the Haber-Bosch process with matching NRR implementations are both desirable and feasible.

Effectively “rare-earth” Y and Sc SACs supported by N-doped amorphous carbon (Y₁/NC, Sc₁/NC) were synthesized by Liu et al.^[129] to catalyze the electrochemical reduction of N under mild conditions. A six-fold coordination, comprised of bonds to C and N, has been deduced for Sc and Y atoms stabilized within carbon defects in past literature.^[168] Sc₁/NC and Y₁/NC NRR performances were evaluated in a 0.1 M HCl and deionized water solution with an airtight electrolytic H-cell at standard temperature and pressure.^[169] Figure 22a displays Y₁/NC and Sc₁/NC LSV curves developed from both N₂ and Ar saturated electrolytes over matching voltage ranges, indicating current density is distinctly higher in N₂ versus Ar saturated solutions, while depicting NRR activity for both Y₁/NC and Sc₁/NC SACs. In contrast, Y₂O₃ and Sc₂O₃ NPs exhibit identical LSV curves in N₂ and Ar gaseous environments, demonstrating N₂ concentration does not impact the conductivities of these NPs and thus implying an absence of NRR activity. However, relatively low NH₃ concentrations produced from N₂ and H₂O during NRR may spuriously remain undetected, as Y₁/NC and Sc₁/NC contain N that can inhibit meaningful detection.^[170] Therefore, NH₃ accumulation in the H-cell was measured after 2 h in controlled experiments. Figure 22b,c resolves the highest NH₃ production rates for Y₁/NC (23.2 μg cm⁻²·h) and Sc₁/NC (20.4 μg cm⁻²·h) at an applied potential (-0.1 V), showing that Y SACs are generally more active than Sc SACs over applied potentials. Cu single atom (Cu SA), porous nitrogen-doped carbon (NC) supported NRR electrocatalysts (NC-Cu SAs) were synthesized by Zang et al.^[171] NC-Cu SA NRR activity was confirmed by LSV curves (Figure 22d) during electrochemical reduction in both N₂-saturated and Ar-saturated 0.1 M KOH, namely by resolving current density differences between both electrolyte solutions at potentials between -0.3 and -0.7 V. Figure 22e depicts averaged NH₃ yields and FEs over varied applied potentials, indicating overlapping maxima for each – respectively 53.3±1.86 μg_{NH3}/mg_{cat}·h and 13.8% – at -0.35 V. The stability of both NC-Cu SA properties over 12 h of continuous operation is displayed in Figure 22f, portraying minimal current, NH₃ yield (from 53.3 to 46.4 μg_{NH3}/mg_{cat}·h), and FE (13.8–11.1%) decreases after eight consecutive cycles. These results correspond to maintaining 94% of NH₃ yield and 91% of efficiency. Such stable activity was ultimately attributed to the favorable and balanced bonding of less concentrated Cu-N₂ ligand complexes to multiple intermediates, as more prevalent Cu-N₄/N₃C complexes had Cu-N binding that was too weak for effective N₂ activation during NRR. Therefore, the trade-off between adsorption-desorption kinetics of NRR intermediates is modulated by NC-Cu SA ligand complex coordination environment.

Dispersing Ru SACs over graphitic carbon nitride supports to form Ru SAs/g-C₃N₄, Yu et al.^[172] compared their NRR performance to those of Cu freestanding foam (CF), g-C₃N₄ supported CF (CF-g-C₃N₄), and CF supporting Ru NPs (CF-Ru NPs). Such controlled comparisons were evaluated for experimental error by reacting all electrocatalysts in both Ar and N₂ saturated environments, then subtracting baseline NH₃ concentrations from Ar experiments for corresponding N₂ measurements. After resolving no significant NH₃ production or NRR activity for CF and CF-g-C₃N₄ through this approach, CF-Ru SAs/g-C₃N₄ were found to be unanimously more efficient than CF-Ru NPs

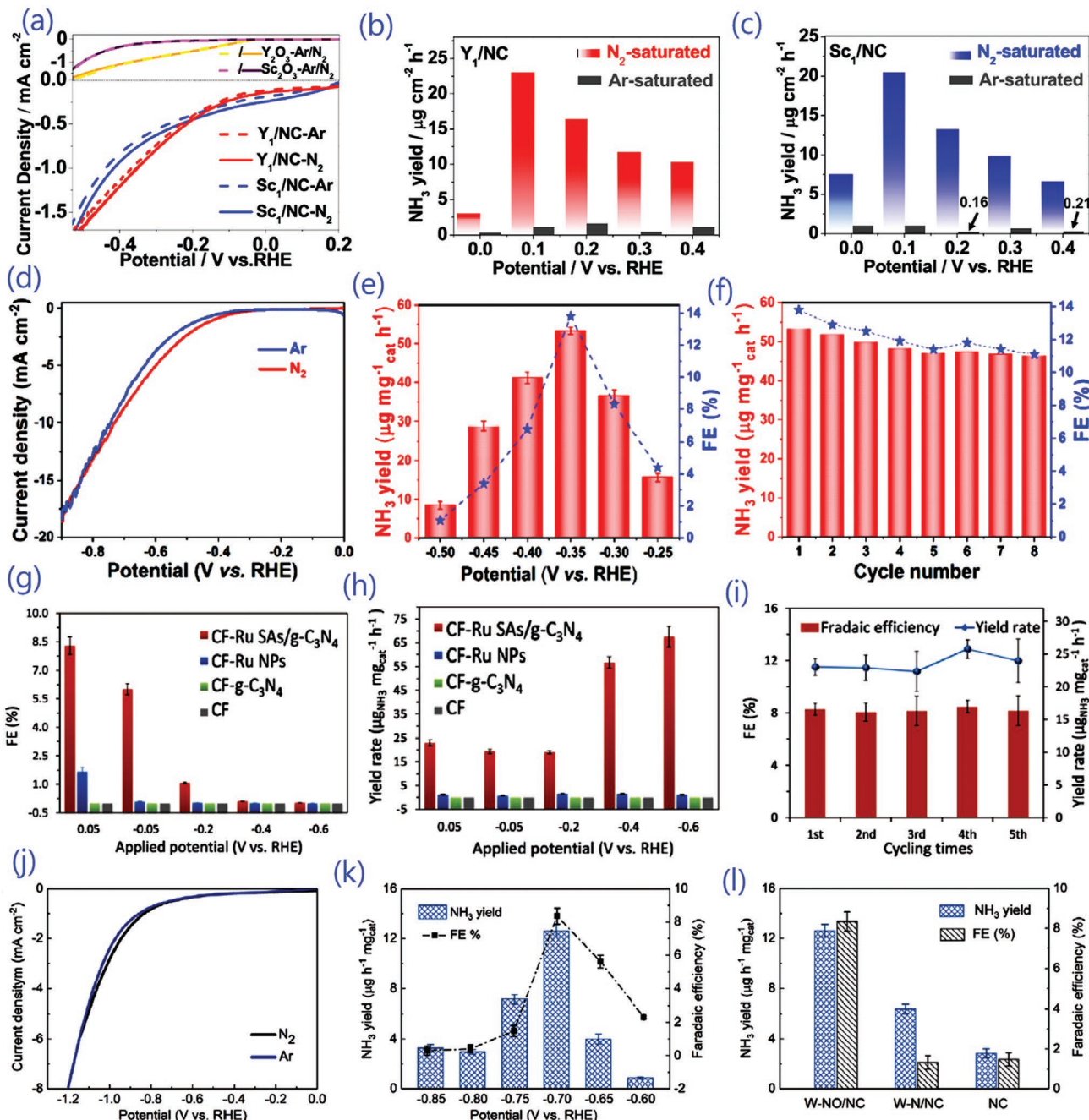


Figure 22. Sc₁/NC and Y₁/NC NRR characterization via a) LSV curves of Sc₁/NC, Y₁/NC, Sc₂O₃, and Y₂O₃, and in N₂ and Ar saturated HCl electrolytes (0.1 M). b) Y₁/NC and c) Sc₁/NC NH₃ yields at different potentials. Adapted with permission.^[129] Copyright 2020, American Chemical Society. NRR NC-Cu SA electrochemical performance, displaying d) LSV curves in N₂ and Ar saturated electrolytes, with NH₃ yield rates and faradaic efficiencies (FE) over different e) potentials and f) cycle numbers (0.1 M KOH). Adapted with permission.^[171] Copyright 2019, American Chemical Society. FEs and NH₃ yield rates at g,h) different potentials (0.05 to -0.60 V vs RHE) and i) over five consecutive cycles. Adapted with permission.^[172] Copyright 2020, Wiley-VCH Verlag GmbH & Co. KGaA, Weinheim. W-NO/NC j) LSV curves in N₂ and Ar saturated electrolytes (0.5 M LiClO₄, scan rate: 2 mV s⁻¹), with matching NH₃ yields and FE k) over all studied potentials and l) referenced to W-N/NC and NC at -0.70 V. Adapted with permission.^[173] Copyright 2021, Wiley-VCH Verlag GmbH & Co. KGaA, Weinheim.

(Figure 22g), with the former (8.3%) having 4.9× the FE of the latter (1.7%) at an applied potential of 0.05 eV versus RHE. Figure 22h resolves a corresponding catalyst weight normalized NH₃ yield of 23.0 μg/mg_{cat}·h, while a maximized CF-Ru SAs/g-C₃N₄ product generation of 67.5 μg/mg_{cat}·h was reached

at -0.6 V at a much lower overpotential. This misalignment of these optimized catalyst properties may be related to multiple physical justifications, which include adsorbate solubility, differences between which structural configurations have the most favorable adsorption thermodynamics and diffusion

kinetics under varied reaction conditions, and rate-limiting intermediate configurations with lower ligand complex and support *d-p* orbital overlap. Arguments involving mechanistic switches or kinetic discrepancies are further substantiated by the transition from NRR to HER dominance as applied potential became more negative. When CF-Ru SAs/g-C₃N₄ surfaces are saturated with H during HER, diffusion involving N₂ intermediates can be impeded, limiting NRR electrocatalytic activity. CF-Ru SAs/g-C₃N₄ stability during electrocatalytic NRR was tested over five consecutive electrolytic cycles at 0.05 V versus RHE, as Figure 22*i* verifies relatively constant NH₃ yields and FEs over this duration. Longer durability tests (12 h) scanned at constant potentials of 0.05 and -0.4 V versus RHE further corroborated long-term CF-Ru SAs/g-C₃N₄ stability.

Combined consideration of metal active center and ligand compositions can – as shown for W SACs coordinated to O and N (W-NO/NC) with high metal loadings (10 wt%) in Gu et al.^[173] – design coordination complexes with favorable electrochemical properties that ultimately result from controlling bonding and orbital overlap. Figure 22*j* confirms W-NO/NC NRR activity in a 0.5 M LiClO₄ electrolyte solution and an H-type two-compartment cell, namely by showing W-NO/NC current density is higher in N₂ than Ar saturated environments. Quantifying the magnitude of such activity, Figure 22*k* depicts corresponding NH₃ yields and Faradaic Efficiencies (FE) versus potential, resolving an optimized W-NO/NC NH₃ yield (12.62 µg/mg_{cat}·h) and corresponding FE (8.35%) at -0.70 V. With respect to W-N/NC and NC controls, W-NO/NC was shown (Figure 22*l*) to more selectively yield NH₃, implying the combined coordination of N and O around W SACs primarily contributes to NH₃ generation and thus NRR activity. When comparing W-N₂O₂ and W-N₄ ligand complexes, N-based intermediates were found to more weakly attach to – and thus more favorably desorb from – SACs with heterogeneous ligands. This was substantiated by relative differences in the character of W-N₂O₂ complex orbitals, encompassing localization of charge around W, higher complex polarizability, and less occupied W-N *d-p* bonding orbital overlap. Thus, the combined electronic structure properties of W, N, and O control the bonding responsible for balancing

NRR adsorption-desorption kinetics, which in turn tune corresponding catalytic activity and NH₃ selectivity.

5.5. Oxygen Reduction/Evolution Reactions: Synergistic Effects and Catalyst Optimization

Layered Ni-N₄/GHSs/Fe-N₄ electrocatalytic ORR activity^[101] was investigated via CV curves resolved in O₂ and N₂-saturated KOH solution (0.1 M), and were referenced against corresponding GHSs/Fe-N₄ and Ni-N₄/GHSs activities in Figure 23a. Relative to the smooth CV curves achieved using N₂-saturated electrolytes, O₂-saturated solutions yielded distinct cathodic peaks that confirmed their ORR activities. Such peaks indicate Ni-N₄/GHSs/Fe-N₄ and GHSs/Fe-N₄ have nearly equal ORR activity significantly superseding that of Ni-N₄/GHSs, implying Fe-N₄ – rather than Ni-N₄ – sites predominantly contribute to ORR activity. Figure 23b displays LSV curves, which were resolved via rotating disk electrodes (RDE), that depict similar ORR activity trends via Ni-N₄/GHSs/Fe-N₄ polarization curves with high onset ($E_{\text{onset}} = 0.93$ V) and half-wave ($E_{1/2} = 0.83$ V) potentials (Table 3). Notwithstanding their proportional impacts, Fe-N₄ and Ni-N₄ both significantly contributed to this strong Ni-N₄/GHSs/Fe-N₄ activity, as evidenced by the improved ORR activity measures (E_{onset} and $E_{1/2}$) of GHSs/Fe-N₄ and Ni-N₄/GHSs versus that of isolated GHSs. Considering all of these structurally engineered contributions to catalytic activity together, Ni-N₄/GHSs/Fe-N₄ is discernably more active than commercial Pt/C catalysts without such layering ($E_{1/2} = 0.86$ V). Improved graphitization in Co SACs supported on N-doped Porous Carbon Nanofibers (Co-N-PCNF)^[105] engineers their ORR stability in acid solutions, as shown in accelerated stability tests. Depicting such long-term testing in O₂ saturated 0.5 M H₂SO₄ (0.85 V vs RHE) for 50 h, Figure 23c substantiates the stability of graphitically layered Co-N-PCNF via insignificant $E_{1/2}$ losses and largely retaining (87%) its initial ORR current density under reaction conditions. However, Figure 23d indicates conventional Co-N-C catalysts – which do not have distinct graphitic layers – significantly lose $E_{1/2}$ (\approx 35 mV, Table 3) and retain less current density (83%).

Table 3. ORR performances of SACs based on recent literature.

Electrocatalyst	Half-wave potential [V vs RHE]	Mass activity	Medium [0.1 M]	Reference
Pt/MoN	0.77	0.71 A mg _{Pt} ⁻¹ at 0.9 V	KOH	[176]
FePc-GO	0.89	–	KOH	[177]
Ni ₁ -NC	≈0.92	≈6800 A g ⁻¹ at 0.8 V	NaOH	[178]
Pt ₁ @Pt/NBP	0.867	0.241 A mg _{Pt} ⁻¹	HClO ₄	[179]
Ce SAS/HPNC	0.862	–	HClO ₄	[180]
Co-N ₃ C ₁	0.824	0.77 A mg _{Pt} ⁻¹ at 0.8 V	KOH	[181]
Ce/Fe-NCNW	0.915	–	KOH	[182]
CoSAs-NGST	0.89	–	KOH	[57]
SA-Fe-NHPC	0.93	–	KOH	[96]
Edge-rich Fe-N ₄	0.80	–	HClO ₄	[180]
Ni-N ₄ /GHSs/Fe-N ₄	0.83	–	KOH	[101]
Fe/Ni-N _x /OC	0.938	–	KOH	[183]

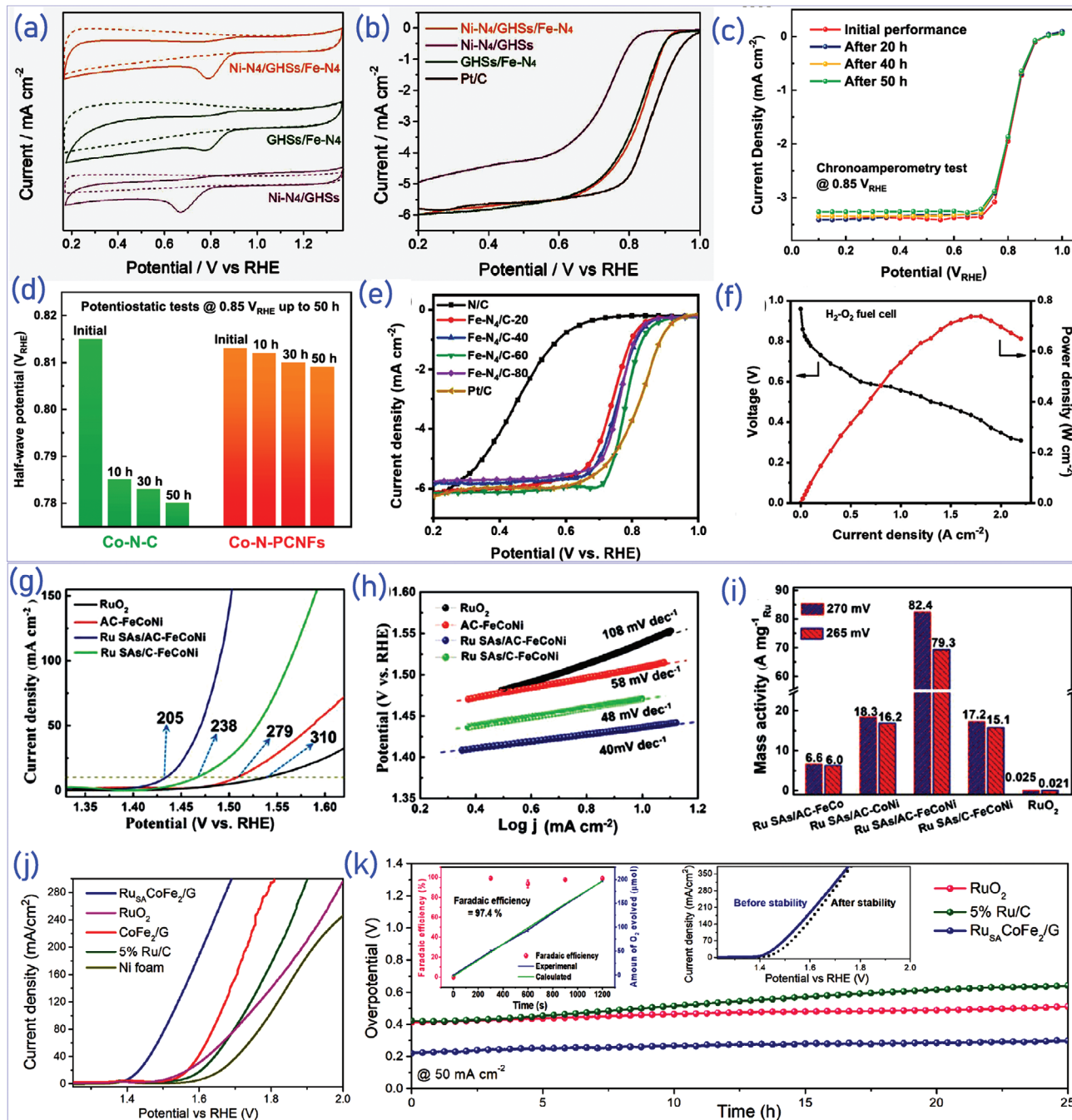


Figure 23. Ni-N₄/GHSs/Fe-N₄ related ORR a) CV and matching b) polarization curves in N₂ or O₂ saturated KOH solution (0.1 M). Adapted with permission.^[101] Copyright 2020, Wiley-VCH Verlag GmbH & Co. KGaA, Weinheim. Co-N-PCNF c) chronoamperometry and d) potentiostatic tests (0.85 V vs RHE). Adapted with permission.^[105] Copyright 2020, Wiley-VCH Verlag GmbH & Co. KGaA, Weinheim. Fe-N₄-C-x e) LSV curves varying x and f) polarization/power density curves achieved with a H₂-O₂ PEMFC (x = 60) in HClO₄ (0.1 M) electrolyte. Adapted with permission.^[174] Copyright 2020, Wiley-VCH Verlag GmbH & Co. KGaA, Weinheim. RuO₂, Ru SAs/C-FeCoNi, Ru SAs/AC-FeCoNi, and AC-FeCoNi g) LSV curves, h) polarization curve Tafel plots, and i) Ru mass activities. Adapted with permission.^[111] Copyright 2020, Wiley-VCH Verlag GmbH & Co. KGaA, Weinheim. RuSACoFe₂/G, RuO₂, and 5% Ru/C j) OER polarization curves and k) chronopotentiometric curves in KOH (1 M) electrolytes (current density = 50 mA cm⁻² for 25 h), with faradaic efficiency and O₂ gas yield from RuSACoFe₂/G (200 mA cm⁻²) in KOH (1 M) electrolytes (left inset of (k)) and LSV curves before and after 25 h of stability testing (right inset of (k)). Adapted with permission.^[113] Copyright 2020, Royal Society of Chemistry.

Wang et al.^[174] developed Fe SACs trapped within the N-modified Divacancies of graphene-like carbon nanosheet Edge (e-ND-Fe) and Center (c-ND-Fe) sites, synthesizing catalysts (Fe-N₄-C-x) with varied initial concentrations of FeCl₃ precur-

sors (x). Figure 23e displays LSV curves indicating that embedding more Fe atoms (higher x of Fe-N₄-C-x) in synthesized supports improves ORR activity relative to solely N-C carbon nanosheet references. Inasmuch as catalyst intrinsic activity is

proportional to kinetic current density (J_k).^[175] Fe–N₄–C-60 has the best tested catalytic activity over 0.7–1.0 V (vs RHE) and supersedes Pt–C (Table 3). The conclusions of these tests were repeated upon normalizing current density relative to specific area to account for divacancy pore volume, spatially resolving e-ND-Fe as having higher activity than c-ND-Fe, and calculating corresponding Fe–N₄–C-60 mass activity (12.3 A mg⁻¹, Fe consumed) and TOF (7.1 s⁻¹). The confirmed high performance of Fe–N₄–C-60 was also tested under more realistic operating conditions as cathodes in a 4 cm² Proton Exchange Membrane Fuel Cell (PEMFC). Applying O₂ as an oxidant, Figure 23f shows Fe–N₄–C-60 based cells exhibit a high maximum power density ($P_{max} = 0.74$ W cm⁻²), validating the possibility of high performance, Pt-free electrocatalysts with spatial and compositional engineering ORR performances of different SACs are summarized in Table 3.

Hu et al.^[111] synthesized Ru SACs (Ru SAs) on hybridized (AC) amorphous (A) and crystalline (C) FeCoNi layered double hydroxide (LDH) hollow nanobox supports, selectively removing structural and compositional features from this treated catalyst to evaluate their effects on OER activity. Comparisons of Ru SAs/AC-FeCoNi, AC-FeCoNi, Ru SAs/C-FeCoNi, and RuO₂ LSV curves depicted in Figure 23g confirm Ru SAs/AC-FeCoNi has the smallest onset potential, as well as a respective ordering of catalysts by onset potential (from low to high). Figure 23h resolves respective overpotentials and Tafel slopes for Ru SAs/AC-FeCoNi (overpotential = 205 mV at 10 mA cm⁻², Tafel slope = 40 mV dec⁻¹), Ru SAs/C-FeCoNi (238 mV, 48 mV dec⁻¹), AC-FeCoNi (279 mV, 58 mV dec⁻¹), and RuO₂ (310 mV, 108 mV dec⁻¹), further expanding the previous claim of relative activity in studied catalysts (Table 4). Ru SAs/AC-FeCoNi electron transfer resistance was also smaller than that of AC-FeCoNi, implying its quicker electron transfer rate. Figure 23i additionally displays high Ru SAs/AC-FeCoNi mass activities at 265 mV (79.3 A mg⁻¹) and 270 mV (82.4 A mg⁻¹) relative to consumed Ru. Overall, FeCoNi supports, amorphous carbon components of such supports, and Ru SACs all contribute to catalytic activity, though the impacts of such engineered structural and compositional features on activity tuning are distinct and ordered according to their magnitudes (small to large).

A similar – albeit more abstract – feature decomposition approach was implemented in Lee et al.^[113] on treated Ru SACs (Ru_{SA}) adsorbed on Co-Fe bimetallic alloys (CoFe₂) encapsulated by graphitic carbon (G), namely versus RuO₂, CoFe₂/G, 5% Ru/C, and Ni foam controls. LSV polarization curves in Figure 23j resolve overpotentials for RuSACoFe₂/G (180 mV), RuO₂ (298 mV), CoFe₂/G (313 mV), and 5% Ru/C (344 mV) during OER (current density = 10 mA cm⁻²), indicating RuSACoFe₂/G is the most active tested catalyst. Beyond better OER activity, catalyst long-term durability was tested via chronopotentiometry (current density = 50 mA cm⁻²) for ≈25 h, revealing strong RuSACoFe₂/G – but weak commercial RuO₂ and 5% Ru/C – overpotential stability during OER (Figure 23k). The insets of Figure 23k not only confirm stability via the overlap of LSV curves measured before and after testing, but also display a high RuSACoFe₂/G faradaic efficiency (97.4%) implying nearly completely efficient SAC-adsorbate charge transfer during OER. Overall, these results consistently indicate that, though Ru complex coordination impacts catalytic performance more than support interactions for these catalysts, the synergistic effects of such engineered structures are primarily responsible for improved catalytic performance OER performances of different SACs are summarized in Table 4.

5.6. Zn-Air Batteries: Multifunctionality and Power Density

Among many energy conversion techniques, rechargeable ZABs – driven by the discharging and charging processes of ORR and OER – are regarded as promising candidates for the next generation of electrical vehicles. Their catalytic activities can be enhanced by i) improving their intrinsic activities and ii) increasing their quantities of available active sites. Optimizing the electronic properties of active single atom sites is a key to fine tuning their catalytic properties, thereby improving their performance in ZABs. Constructing nanostructures with hierarchical porous interconnections, large surface areas, uniform nanocages, and rich N species to enhance substrate structure functionalities are other effective approaches for improving the catalytic performance of ZABs, as such approaches benefit active site accessibility and mass transport properties.

Table 4. OER performances of SACs based on recent literature.

Electrocatalyst	Overpotentials at 10 mA cm ⁻² (Activities)	Stabilities	Medium	Reference
Ru SAs/AC-FeCoNi	205 mV	Negligible deactivation for 48 h	1 M KOH	[113]
Ni-Ru@RuO _x -HL	184 mV	9 mV potential change after 30 h stability test	0.5 M H ₂ SO ₄	[32]
Ir-NiO	215 mV	Durable for 10 h	1 M KOH	[110]
SAC-NiSO ₄ -GF	300 mV	Negligible deactivation after 20 h	1 M KOH	[184]
Co-P SAC MWCNT	290 mV	Negligible degradation of stability after 10 h	1 M KOH	[185]
IrCoO _x ANSs	152 ± 5.2 mV	Stable after 10 h	1 M KOH	[186]
NiP _c -GO	320 mV	Negligible change in stability after 3000 CV cycles	1 M KOH	[183]
Ir–NiCo ₂ O ₄ NSs	240 mV	Long-term stability of 70 h	0.5 M H ₂ SO ₄	[106]
Ag ₁ /IrO _x SAC	224 mV	Slight increase (=15 mV) in the overpotential after 3000 cycles	0.5 M H ₂ SO ₄	[33]
CoSAs-NGST	560 mV	Electrocatalyst retains 86.2% of the cathodic current after 20 000 s	0.1 M KOH	[57]

The trifunctional CoSA/N,S-HCS catalysts produced in Zhang et al.^[103] were adapted to ZABs powering a water-splitting process comprised of respective charge (OER) and discharge (ORR) cycles (Figure 24a). Figure 24b,c plots the charge and discharge polarization curves of this process with matching discharge cycle power density. Figure 24d resolves the corresponding large specific discharge capacity ($781.1 \text{ mA}\cdot\text{h g}^{-1}$ at 10 mA cm^{-2}) and energy density ($941.1 \text{ W}\cdot\text{h kg}^{-1}$ consumed Zn) of such ZABs, which outperform Pt/C+RuO₂ based batteries ($712.7 \text{ mA}\cdot\text{h g}^{-1}$, $846.7 \text{ W}\cdot\text{h kg}^{-1}$) and can power a 33 yellow LED array for several hours when paired and placed in series (Figure 24d, inset). Over continuous, galvanostatic, alternating 10 min charge and discharge cycles and at a current density of 10 mA cm^{-2} , battery efficiency and long-term rechargeability are tested for both studied batteries. Figure 24e indicates the initial voltage gap and high round-trip efficiency of ZABs (0.82 V, 59.6%) supersede those of Pt/C+RuO₂ based batteries (0.85 V, 58.7%), while their respective long-term performances negligibly decrease after 1000 cycles ($\approx 333 \text{ h}$) and diminish via voltage gap increases (from 0.85 to 1.04 V) after 60 cycles of operation. Therefore, ZABs developed with CoSA/N,S-HCS can accommodate iterative OER and ORR processes via charge and discharge polarization cycles better than their conventional Pt-based analogues, namely in connection with their well-dispersed, well-coordinated ligand complexes and S-facilitated electron charge transfer.

Gong et al.^[92] developed ZABs using hierarchically porous Fe/N-CNRs and Fe-N₄ active sites for ORR electrocatalysis. Fe/N-CNR SACs served as primary ZAB cathodes compared to reference Pt/C-based electrodes (Figure 24f). As shown in Figure 24g, Fe/N-CNR ZABs reached a maximum power density of 181.8 mW cm^{-2} , exceeding that of ZABs with Pt/C cathodes (137.5 mW cm^{-2}). Specific capacities (energy densities in parentheses), normalized to the Zn mass consumed during electrochemical reactions, were respectively $771.77 \text{ mA}\cdot\text{h g}^{-1}$ (gravimetric energy density: $998.67 \text{ W}\cdot\text{h kg}^{-1}$) and $742.42 \text{ mA}\cdot\text{h g}^{-1}$ (energy density: $950.60 \text{ W}\cdot\text{h kg}^{-1}$) at 10 mA cm^{-2} for ZABs with Fe/N-CNR and Pt/C cathodes (Figure 24h). Beyond these apparent advantages, SAC-based ZABs have proven to be capable of replacing matching Pt/C systems by practically powering LED devices, being rechargeable via replenishing anode and electrode materials, and maintaining strong ORR discharge polarization curves over time.

Mn Single-Atom Sites with N-doped Carbon Supports (Mn-SAS/CN) developed by Han et al.^[28] were applied to ZABs and referenced to ZABs comprised of 20% Pt/C air cathodes. Polarization curves and power density plots in Figure 24i reveal Mn-SAS/CN ZAB performance respectively matched and superseded that of Pt/C ZABs at high voltage and high current density. Mn-SAS/CN ZABs observed a maximum power density (220 mW cm^{-2} at 0.74 V) higher than that of Pt/C ZABs (185 mW cm^{-2} at 0.80 V). Galvanostatic discharge tests visualized in Figure 24j (10 mA cm^{-2}) did not resolve notable voltage drops after $90\,000 \text{ s}$, implying the durability of Mn-SAS/CN cathodes. Figure 24k depicts the recovered voltage and stability of Mn-SAS/CN with continuous electronic discharge until Zn is completely consumed, yielding a corresponding specific capacity (normalized to consumed Zn mass) of $780 \text{ mA}\cdot\text{h g}^{-1}$. Thus, Mn-SAS/CN ZABs are promising candidates for replacing Pt-based ZABs.

Li et al.^[119] synthesized Single Atom Pt catalysts locally stabilized via trapping interstitial F in alloyed PtCo nanosheets (SA-PtCoF) to not only achieve strong bifunctional ORR and OER activity, but also serve as air cathodes in rechargeable ZABs. Galvanostatic charge-discharge profiles for Pt/C@RuO₂ and SA-PtCoF in Figure 24l (current density = 10 mA cm^{-2}) resolve more favorable charge-discharge voltage gaps for SA-PtCoF than Pt/C@RuO₂ over 240 h of cycling, respectively indicating catalyst activation (reduced from 1.03 to 0.9 V) and degradation (increased from 0.69 to 1.03 V). Figure 24m plots polarization and power density profiles confirming the superior maximum power density of SA-PtCoF (125 mW cm^{-2} at 266 mA cm^{-2}) over commercial Pt/C@RuO₂ (55 mW cm^{-2} , 155 mA cm^{-2}), which can be connected to the environmental exposure of Pt SACs on PtCoF.^[187] ZAB galvanostatic discharge curves with SA-PtCoF cathodes (Figure 24n) do not apparently decay until the full consumption of their Zn anodes, implying their significant durability. Their specific capacities were $808 \text{ mA}\cdot\text{h g}^{-1}$ (10 mA cm^{-2}) and $806 \text{ mA}\cdot\text{h g}^{-1}$ (20 mA cm^{-2}), with a matching energy density of $785 \text{ W}\cdot\text{h kg}^{-1}$ (10 mA cm^{-2}). All of these properties supersede those of analogous modern electrodes.^[188,189]

5.7. Rechargeable Li-Batteries: Charge/Discharge Cycling and Mechanisms

Liang et al.^[190] synthesized uniformly dispersed Fe atoms on 2D graphene-like C₂N frameworks as cathodes in lithium-sulfur batteries (S@Fe/C₂N). Figure 25a depicts galvanostatic charge-discharge curves for S@Fe/C₂N and S@C₂N (Fe-free control) electrodes at a constant current rate (0.1 C), representing Li₂S activation overpotentials as initial voltage jumps in charging curves (blue). Fe accelerates Li₂S activation, as C₂N electrodes have higher activation overpotentials than Fe/C₂N electrodes. Discharge (red) and charge (blue) curves have two and one respective apparent plateaus, which correspond to reaction mechanisms. The discharge curve, which correlates with multistep sulfur decomposition reaction coordinates, has a first plateau ($\approx 2.3 \text{ V}$) associated with sulfur reduction ($S_8 \rightarrow S_6^{2-} \rightarrow S_4^{4-}$) and a second plateau ($\approx 2.1 \text{ V}$) representing conversion from reduced sulfur to soluble LiPS and finally lithium sulfide ($S_4^{2-} \rightarrow Li_2S_2 \rightarrow Li_2S$).^[191] Given this discharge-mechanism relationship predicated on reaction kinetics, increases in ratios between the second (Q_2) and first (Q_1) discharge plateaus (Q_2/Q_1) are proportional to electrode catalytic activity improvements.^[192] Figure 25b resolves a higher capacity ratio for S@Fe/C₂N ($Q_2/Q_1 = 2.86$) than S@C₂N ($Q_2/Q_1 = 2.35$) electrodes, confirming Fe-loaded electrodes observe better catalytic activity in polysulfide redox reactions. The polarization potential, or difference between the oxidation and second reduction potentials, of the S@Fe/C₂N ($\Delta E = 142.3 \text{ mV}$) and S@C₂N ($\Delta E = 180.9 \text{ mV}$) electrodes further substantiate this conclusion. Galvanostatic charge-discharge profiles over a current density range (0.1–5 C) displayed in Figure 25c demonstrate the same two discharge and single charge plateaus over all tested domains. Corresponding variable discharge rates were portrayed in Figure 25d, resolving S@Fe/C₂N specific capacities (at incremented current rates) of 1480 (0.1 C), 1250 (0.2 C), 1085 (0.5 C), 955 (1 C), 856.4 (2 C), 774 (3 C), and 683 (5 C) $\text{mA}\cdot\text{h g}^{-1}$ that are strictly

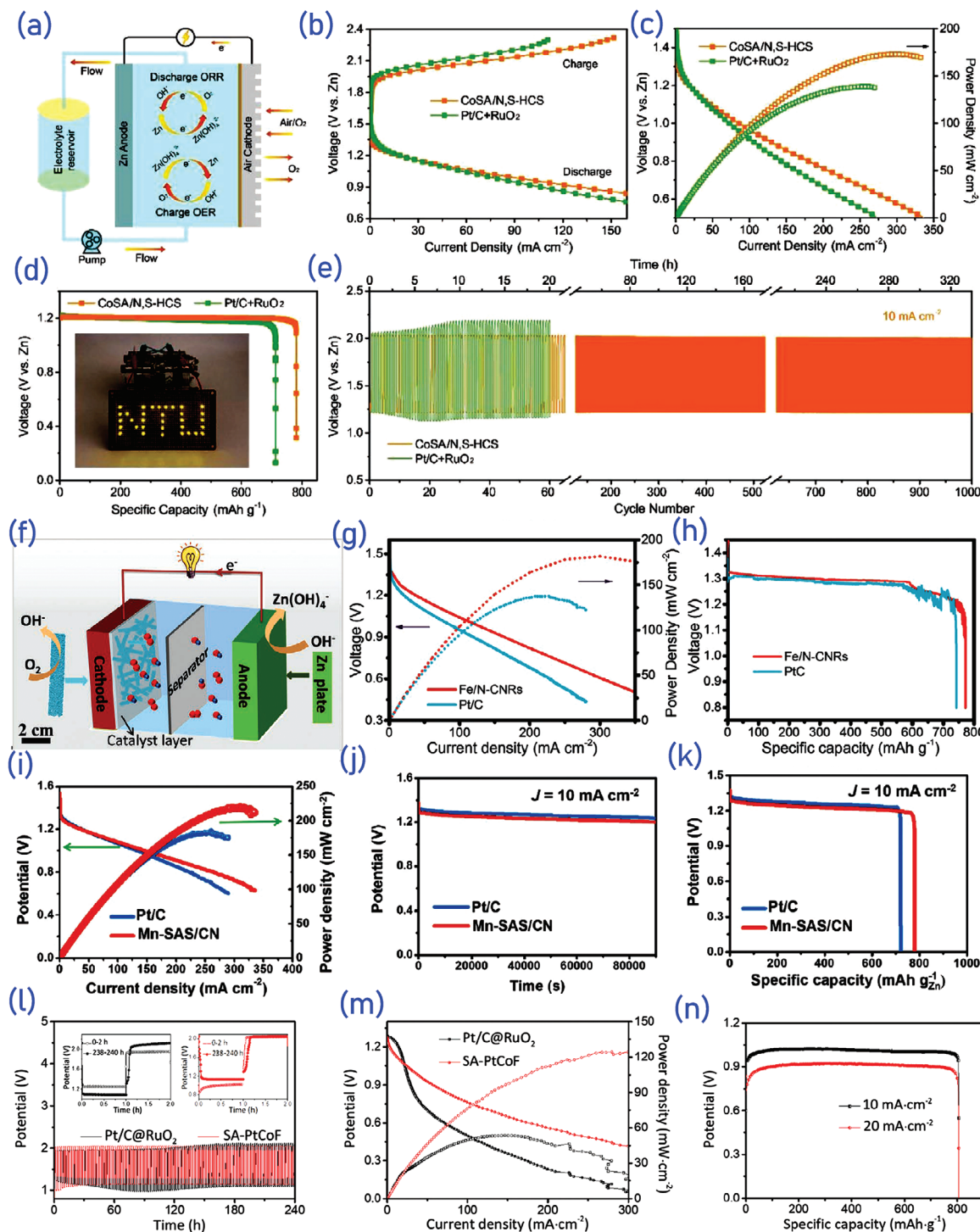


Figure 24. a) Heuristic depiction of a liquid flow ZAB. Pt/C+RuO₂ and CoSA/N,S-HCS ZAB b) discharge-charge polarization curves, c) polarization curves (discharge only) with matching power density plots, d) galvanostatic discharge curves (inset: LEDs powered by 2 ZABs arranged in series), and e) galvanostatic discharge-charge cycling curves. Adapted with permission.^[103] Copyright 2020, Wiley-VCH Verlag GmbH & Co. KGaA, Weinheim. f) Schematic of Fe/N-CNRs and Pt/C ZABs with g) polarization and power density results and h) specific capacities at 10 mA cm⁻² (relative to Zn mass consumed). Adapted with permission.^[92] Copyright 2020, Wiley-VCH Verlag GmbH & Co. KGaA, Weinheim. Mn-SAS/CN and Pt/C cathode i) polarization curves and matching power density plots, j) long-term discharge curves, and k) typical discharge versus specific capacity curves under perpetual discharge until all Zn is consumed (discharge current density = 10 mA cm⁻²), with specific capacity set relative to consumed Zn mass. Adapted with permission.^[28] Copyright 2020, Wiley-VCH Verlag GmbH & Co. KGaA, Weinheim. SA-PtCoF and Pt/C@RuO₂ ZAB l) long-term charge-discharge curves (current density = 10 mA cm⁻², inset shows last and first discharge-charge profiles), m) polarization curves and matching power density plots, and n) long-term discharge versus specific capacity curves while varying current density (specific capacity calculated using Zn mass consumption). Adapted with permission.^[119] Copyright 2020, Royal Society of Chemistry.

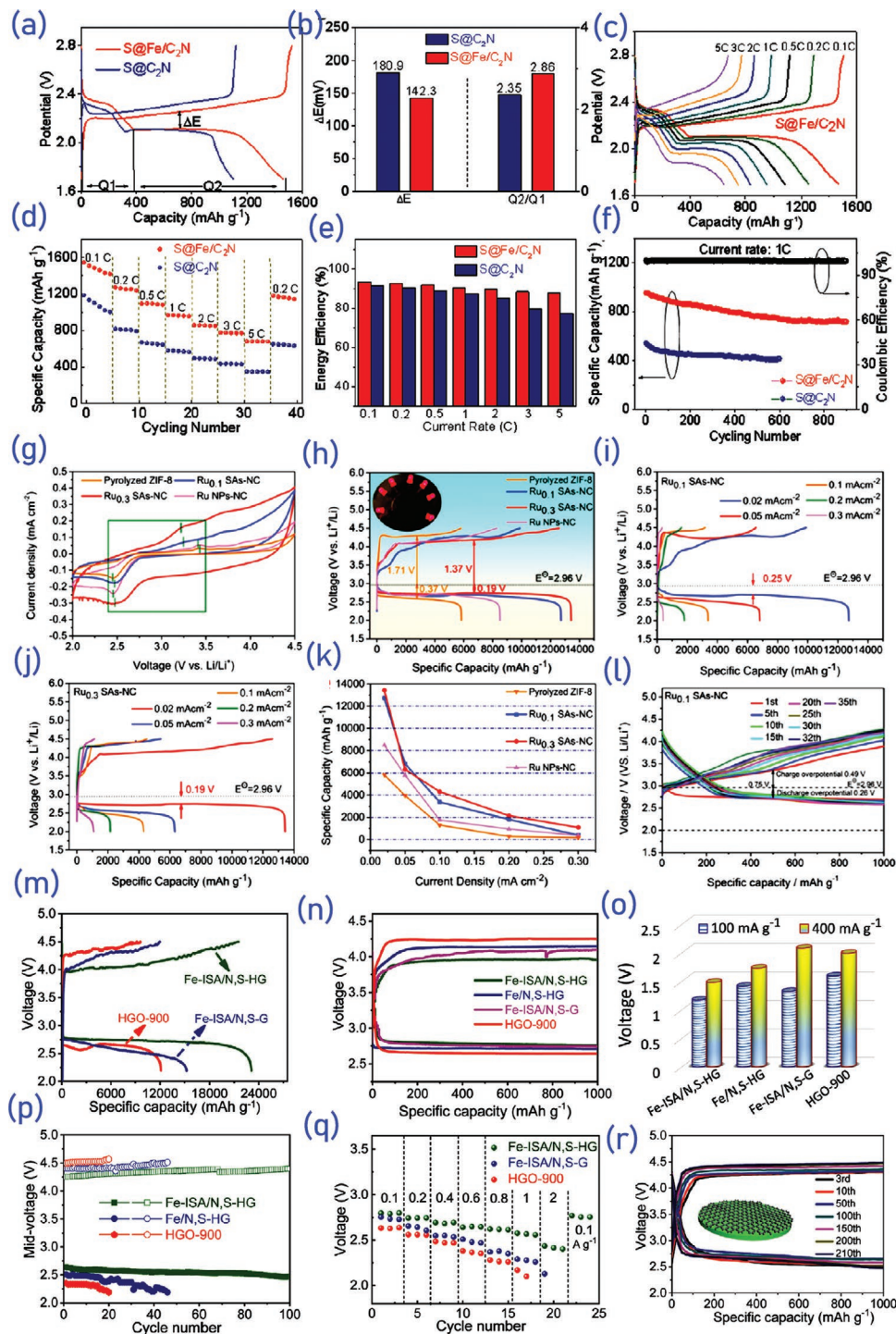


Figure 25. S@Fe/C₂N and S@C₂N electrode a) galvanostatic charge-discharge profiles (0.1 C current rate), b) ΔE and Q_2/Q_1 resulting from (a), c) galvanostatic charge-discharge profiles (various current rates), d) rate capabilities (current rates = 0.1–5 C), e) energy efficiencies (various current rates), and f) capacity retention (1 C). Adapted with permission.^[190] Copyright 2020, Wiley-VCH Verlag GmbH & Co. KGaA, Weinheim. Ru_{0.3} SAs-NC, Ru_{0.1} SAs-NC, Ru NP, and ZIF-8 LOB g) CV curves (2.0–4.5 V, 0.1 mV s⁻¹), h) initial deep discharge–charge curves (current density = 0.02 mA cm⁻²), and i,j) charge-discharge curves over discharge-based specific capacities while varying current density. k) LOB discharge specific capacities over varied current densities and l) discharge-charge curves of Ru_{0.1} SAs-NCs (current density = 0.02 mA cm⁻², fixed capacity = 1000 mA·h g⁻¹, over 2.0–4.5 V). Adapted with permission.^[112] Copyright 2020, American Chemical Society. Fe-ISA/N,S-G, Fe/N,S-HG, HGO-900, and Fe-ISA/N,S-HG Li–CO₂ battery m) full charge–discharge profiles (100 mA g⁻¹), n) initial discharge-charge profiles (100 mA g⁻¹) applying limited discharge-charge capacities (1000 mA·h g⁻¹), o) potential gaps (current densities = 100, 400 mA g⁻¹), p) cycling performances (1 A g⁻¹), q) capacities at different applied current densities, and r) discharge-charge profiles. Adapted with permission.^[194] Copyright 2020, Wiley-VCH Verlag GmbH & Co. KGaA, Weinheim.

higher than those of S@C₂N. Decremental current rates achieved similar average capacities for S@Fe/C₂N electrode (1172 mA·h g⁻¹), implying their strong stability. Calculated S@Fe/C₂N energy efficiencies (93% at 0.1 C) are also higher than those of S@C₂N (Figure 25e), correlated with both the lower polarization potential and exceptional catalytic properties of Fe/C₂N catalysts. Figure 25f depicts S@Fe/C₂N and S@C₂N electrode cycling performances (1 C), determining S@Fe/C₂N electrodes have two-fold higher capacity, better stability, and retain a discharge capacity of 716.5 mA·h g⁻¹ over 900 cycles (Coulombic efficiency = 99.7%, capacity retention = 75.14%).

Hu et al.^[112] synthesized Ru SACs spatially confined, without binding agents, within the MOF pores of N-doped carbon supports (Ru SAs-NC) for high-efficiency lithium oxide battery (LOB) cathode applications. High temperature pyrolysis on carbon cloth ionically substitutes Ru³⁺ into the Zn²⁺ sites of ZIF-8 precursors to form catalysts with various fractions of confined Ru atoms, such as Ru_{0.3} SAs-NC and Ru_{0.1} SAs-NC. Figure 25g presents the CV curves of such SACs compared to pyrolyzed ZIF-8 and Ru NP controls, revealing not only distinct oxidation and reduction peaks of all catalysts but also the higher ORR onset potentials of Ru_{0.1} SAs-NC (\approx 2.85 V) and Ru_{0.3} SAs-NC (\approx 2.88 V). The reduced polarization of Ru SACs during ORR charge-discharge cycles can be attributed to particular reactions, such as the connection of the cathodic peak (\approx 2.55 V) of Ru_{0.3} SAs-NC to O₂ + 2e⁻ + 2Li⁺ \rightarrow Li₂O₂. Two step Li₂O₂ oxidation during OER generates two anodic peaks (\approx 3.70 V, \approx 3.18 V) representing discharge cycle product decomposition, which can be respectively correlated with the reactions Li₂O₂ \rightarrow 2Li⁺ + O₂ + 2e⁻ and LiO₂ \rightarrow Li⁺ + O₂ + e⁻ (3V vs Li/Li⁺).^[193] Given Ru_{0.3} SAs-NC cathodic peak location is slightly higher than the corresponding ZIF-8 peak and the OER anodic scan onset potential is lower than that of the ORR cathodic scan, Ru SACs observe evidently strong catalytic activity over ORR and OER. Thus, Ru are ORR and OER active sites in Ru SAs-NCs, substantially improving catalytic performance with relative Ru³⁺-Zn²⁺ substitution. This is manifested through the higher ORR peaks, OER peaks, and related integrated areas seen in Ru_{0.3} SAs-NC electrodes than in other compared structures, implying their proportionally greater ability to produce Li₂O₂.^[112] Deep discharge-charge and limited capacity cycles evaluated in previously discussed LOBs via Figure 25h portray discharge-charge curves within a voltage window of 2.0–4.5 V and at a current density of 0.02 mA cm⁻², revealing Ru_{0.3} SAs-NC battery cathodes observe much higher capacities (13424 mA·h g⁻¹) than referenced Ru_{0.1} SAs-NC (12724 mA·h g⁻¹), Ru NPs-NC (8511 mA·h g⁻¹), and pyrolyzed ZIF-8 (5822 mA·h g⁻¹) structures. Ru_{0.3} SAs-NC also exhibits a lower overpotential than ZIF-8, further confirming Ru substitution is responsible for improving ORR and OER activities. Figure 25i,j displays the rate capabilities of studied catalysts at current densities of 0.05, 0.1, 0.2, and 0.3 mA cm⁻², respectively resolving capacities of 6814, 3379, 1809, and 400 mA·h g⁻¹ for Ru_{0.1} SAs-NCs. Respective Ru_{0.3} SAs-NC capacities of 6311, 4309, 2154, and 1089 mA·h g⁻¹ verify that incrementing current density generally increases the averaged charge-discharge voltage differences of studied LOBs. Moreover, Figure 25k depicts the superior discharge capacity of Ru_{0.3} SAs-NC LOBs over Ru_{0.1} SAs-NC and Ru NPs-NC electrodes, further demonstrating how

Ru SACs augment LOB performance with improved Ru site concentration. Figure 25l shows Ru_{0.3} SAs-NC voltage profiles, limited to a capacity of 1000 mA·h g⁻¹ during iterative charge-discharge cycles, exhibit better cycle life, polarized discharge overpotential, and recharge overpotential than tested controls, enabled partially by Ru-N₄ ligand complexes and their mixture with Li₂O₂ products.

Hu et al.^[194] Implanted Single Fe Atoms into three dimensionally interconnected, porous, N,S co-doped Holey Graphene (Fe-ISA/N,S-HG) supports, yielding efficient catalysts for CO₂RR and corresponding evolution reactions applied to rechargeable Li-CO₂ batteries. Fe-ISA/N,S-HG cathodes placed in Li-CO₂ batteries develop charge-discharge profiles (Figure 25m, current density = 100 mA g⁻¹) with discharge (23174 mA·h g⁻¹) and charge (21520 mA·h g⁻¹, cathode material consumed) capacities that supersede those of analogously tested Fe-ISA/N,S-G (graphene supports without holey structures) architectures (discharge: 15279.9, charge: 12007.0 mA·h g⁻¹) and HGO-900 (slightly holey oxidized graphene supports annealed at 900 °C) cathodes (discharge: 12136.8, charge: 9496.7 mAh g⁻¹). Figure 25m also shows Fe-ISA/N,S-HG not only resolve formidable discharge capacity measurements spanning area (4.9 mA·h cm⁻²) and volume (405.5 mA·h cm⁻³), but also observe better Coulombic efficiencies (92.9%) than referenced Fe-ISA/N,S-G (78.6%) and HGO-900 (78.2%) systems during correlated Li₂CO₃ decomposition and battery charging processes. Figure 25n,o further reveals Fe-ISA/N,S-HG has a comparably smaller potential gap (1.17 V), high discharge potential (2.78 V), and low charge potential (3.95 V) than other reviewed cathodes, indicating its bifunctional catalytic activity in Li₂CO₃ formation (discharge) and decomposition (charge) reactions. Reevaluation of such results over long-term cycling (Figure 25p) and high current densities (1 A g⁻¹) validates comparably strong Fe-ISA/N,S-HG stability, yielding narrow charge-discharge potential gaps (1.61 V) with high retention (80.1%) after 100 cycles (cut-off capacity = 1000 mA·h g⁻¹). Such results can be attributed to strong Fe-ISA/N,S-HG cathode activity during iterative catalytic formation and decomposition of Li₂CO₃, additionally implying effective stability (cut-off capacity = 1000 mA·h g⁻¹) over longer cycling periods (>100 cycles) and more intense operating conditions (1 A g⁻¹). Figure 25q compares cathode rate capabilities during discharge potential reversal when reducing current density from higher values to 100 mA g⁻¹, revealing Fe-ISA/N,S-G, Fe/N,S-HG (no acid leaching treatment to remove Fe-S species), and HGO-900 controls could only start from as high as \approx 800–1000 mA g⁻¹ until experiencing irreversible decay. In contrast, Fe-ISA/N,S-HG with both implanted Fe and holey structures enabled ionic diffusion, reducing ionic and Ohmic resistances to produce enduring high catalytic activity.^[195] Holey architectures supporting Fe SACs improve Li-CO₂ battery performance by augmenting gas/electrolyte diffusion, forming more active sites for co-doped N,S and Fe-N ligand complexes, and granting more available surface area for Li₂CO₃ formation. Though CO₂ can help form stable solid electrolyte interface layers^[196] and CO₂ dissolved in such electrolytes can corrode Li anodes over long-term cycling, Figure 25r indicates Fe-ISA/N,S-HG cathodes in Li-CO₂ batteries can last 210 charge-discharge cycles when coating Li anodes with protective reduced graphene oxide in tetrahydrofuran.^[194,197]

6. Single-Site Heterogeneous Catalysts

Single-site heterogeneous catalysts, or Heterogeneous Single-Atom Catalysts (HSACs), feature heterogeneous SAC molecular structures, and are analogized to SACs with homogeneous molecular structures via the same comparison reconciling heteroleptic and homoleptic organometallic ligand complexes.^[198,199] More specifically, each HSAC features multiple unique ligands while being sufficiently isolated (from other HSACs) due to uniform distribution on substrates, enabling inherent precise modulation of surface metal atomic structure. Given this potential to intrinsically and precisely control surface reactions, HSAC design serves as a paradigm towards balancing high catalytic activities, selectivities, and durabilities tailored to specific industrial applications. HSACs that are simultaneously strongly anchored to supports, uniformly dispersed over those supports, and effectively characterized are useful in heterogeneous catalysis applications for several reasons. With respect to their inherent characteristics, HSACs maximize atom utilization, facilitate high surface coverage, and are structurally uniform, thus likely yielding strong selectivities and turnover frequencies (TOFs). Relative to characterization, HSAC active sites are comprised of dispersed metal atoms with local coordination environments that are readily probed via techniques such as TEM, EXAFS, and XANES. Deriving structure-activity relationships at such sites for catalyst design is eased by readily available characterization methods. Practically, HSACs can be separated and recycled during operation without affecting catalytic performance, which is particularly useful for heterogeneous reactions involving liquid phases.^[200] Isolated HSAC active metal sites are directly attached to their substrates, and are further anchored to supports via the surface-bonded atoms comprising their ligands. The compositions of such surface atoms – including nitrogen, oxygen, and sulfur – tune HSAC electronic structure and activity by modulating metal-ligand bonding, which is precisely controllable due to the high metal utilization afforded to isolated metal active centers. HSACs thus gain their namesake from the ability to feature heterogeneously composed ligand atoms bonded to surfaces, as well as the similarly varied effects of such heterogeneous metal-ligand and ligand-support bonding on catalytic properties. Nevertheless, the ability to systematically engineer ligand atom compositions to transition between homogenous and heterogeneous SACs provides a methodology for designing such HSACs. Such design principles encompass maximizing catalytic activity and high temperature stability, as well as optimizing the trade-off between such properties via synergistic effects.^[201] Previously defined HSAC properties^[54] can be extensively tuned by modifying metal-support, metal-ligand, and other types of bonding. Salient considerations affecting the engineering of such HSAC bonds are described as follows:

- i) Engineering defects in catalyst supports is critical to successfully controlling metal active center bonding. Not only does anchoring such metal atoms to surfaces necessarily stabilize them for surface reactions, but the relative strength of metal-surface binding tunes catalyst activities for different atomic mechanisms occurring over the extent of a full reaction process. When activation barriers for specific mechanisms do

not limit such reaction processes due to thermodynamic conditions or other considerations, the relative favorability of a final structure yielded from a reaction process – with respect to the stabilities of corresponding initial and intermediate structures – is well-correlated with metal-support bond strength.

- ii) Isolated metal atoms – which are simultaneously active centers in ligand complexes and stabilized on supports – observe both covalent and ionic bonding character, such that their distinct metal-support and metal-ligand interactions can modulate specific features of their electronic structures. Such modulation is quantifiable via relationships involving site specific charge states and metal center coordination environments, both of which are impacted by metal-support bonding. When reducing metal NP size towards the asymptotic limit of the single atom, the atomic and electronic structures of metal active centers significantly change due to quantum confinement effects, the desaturation of active center coordination environments, and variations in neighboring atom bond strengths. Over the multiple mechanisms constituting catalytic processes, single atom active centers change coordination while interacting with reactants and intermediates, dynamically modifying metal-support chemical bond strengths and thus catalyst stability throughout reaction processes.
- iii) Combining mixed compositions of metal centers to form dimer – or generalized multimer – chains of connected ligand complexes provides both new mechanistic paths for surface reactions and mixed adsorbate site configurations. The electronic structures of primary metal active sites can be extensively modulated by synergistic interactions with secondary metals via non-nearest neighbor bonding through shared ligands. Such electronic structure tuning is more effective than that allotted by solely engineering metal-support or metal-ligand bonding. Further, improving the number of possible combinations of ligands attached to metal centers not only improves HSAC multifunctionality, but also refines the gradation of distinct property values available to tuning. For example, typical nanoparticles have multiple discrete and energetically distinct metal sites – such as those on terraces, facet edges, and facet vertices – available to organic ligand adsorption, which are capable of producing commensurately discrete changes in properties upon adsorbate bonding. In contrast, multimer HSACs with large numbers of possible ligand combinations – and thus distinct adsorption configurations – can approach producing continuous property values, which can be useful for fine-tuning product selectivity and activity in multi-mechanism reaction processes. Given advances in synthesis procedures, characterization methods, and reaction mechanism elucidations towards developing SACs, evolving the HSAC capabilities of extensive electronic structure modification, multifunctionality, and property value fine-tuning should primarily require engineering multimer chain length size. Therefore, the expansion of multimer HSAC chain lengths bridges the trade-off between the well-controlled selective product formation of isolated SACs and the ensemble averaged property values observed in bulk materials, namely when approaching the asymptotic limit of macroscale chain lengths. Pertinently applied multiscale engineering would balance this trade-off between individual atomic scale chemical reactions and macroscale

phenomenological observations, yielding multimers that produce multiple, highly tunable property values during reactions while approaching macroscale sizes and bulk (continuum) property results.

7. Outlook, Challenge, and Future Work

7.1. Outlook and Conclusion

Electrocatalysis will be critical to providing renewable solutions that not only overcome energy and power generation problems, but also eliminate environmental pollution and related negative externalities. Towards the resolution of these issues, SACs are highly promising. This review closely discusses the current status of SACs based on the most recent literature, evaluating the potential for SAC application in future energy technologies. Possible mechanisms for SAC activity are introduced and characterized, aiding a broad readership in designing and developing highly active metal SACs. Thus, single atom M–N–C electrocatalysts (M = transition metal atom) afford extraordinary electrocatalytic performance due to their ultrahigh intrinsic reactivity, maximized atom efficiency, and favorable electronic conduction and ion transport with the hierarchical carbon structures of their substrates. Further, SAC catalytic activity and selectivity not only depend on metal atom characteristics, but also on the properties of the solid supports on which SACs are dispersed. Surface science methods reveal CO adsorption strengths of single metal active centers which vary from those of corresponding supported clusters and metal surfaces. Charge transfer from SACs to supports changes metal atom *d*-states and hence strengthens or weakens metal–CO bond strength, while CO-induced structural distortions reduce adsorption energies. Therefore, choosing a substrate that ensures strong interactions with isolated SACs is essential to achieving desired catalysts, while using supports that are strongly conductive, electrochemically active, and hydrophilic is important for anchoring isolated single atoms in water-based reactions.

Various metal SAC compositions – including Co, Ni, Fe, Au, Ag, Cu, Mo, Pt, Pd, Y, Sc, La, Ru, Rh, and Ir – and their effects on ORR, OER, HER, CO₂RR, NRR, and both ZAB and Li batteries have been discussed. For example, Pt SACs in VS₂ nanosheets delivered excellent mass activity during HER, while corresponding theoretical investigations demonstrate that H absorption behavior and charge-transfer kinetics can be optimized via Pt decoration to improve HER. In addition, coupling between single atom Fe–N₄ complexes and intrinsic carbon substrate defects was shown to improve experimental Fe SAC catalytic activity during CO₂RR, namely when combined with quick electronic transfer and multitudinous exposed active sites. Complementary DFT calculations suggest that defect engineering induces more active sites, faster electron transfer, and higher defect site intrinsic activity, which work together to develop exceptional CO₂RR performance. Further, single Janus catalysts (layered Ni-N₄/GHSs/Fe-N₄) performing both ORR and OER can simplify metal–air battery setups relative to two air cathode compartment designs. In another example, single Fe centers implanted into 3D intertwined and porous

N, S co-doped holey graphene architectures are implemented as highly efficient catalysts in rechargeable Li–CO₂ batteries. In yet another case, DFT calculations reveal OER performance is prominently incurred by interfacial electron exchange and electron transfer from atomic Ir incorporation near the intrinsic oxygen vacancies of NiCo₂O₄ surfaces. In each of these cases, the relationship between SAC and support was critical to developing multifunctional catalyst behaviors, especially when involving useful charge transfer relationships. “Rare-earth” (R = Y, Sc, La) based ligand complexes differ from the transition metal based SACs, as the large atomic radii of Sc and Y tend to be anchored to large carbon defects via six-fold coordination comprised of R–N and R–C bonds. Thus, Sc₁/NC and Y₁/NC SACs possess strong catalytic activities during NRR and CO₂RR due to local electronic structure modulation from N and C bonding. Such catalytic functions not only demonstrate SAC efficacy, but also promote “rare-earth” catalyst applications in electrochemical reactions. Moreover, La single atoms on carbon nitride supports feature La–N charge-transfer bridges that are responsible for photocatalytic CO₂ reduction activity enhancement, as they are the key active centers for CO₂ activation, rapid COOH* formation, and CO desorption. Thus, “rare-earth” SACs, with metal atoms featuring characteristically sparse valence band structures and higher coordination numbers, have distinct bonding and charge transfer properties associated with their orbital configurations.

Ionic substitution methods and spatial confinement aided by MOFs were employed to yield Ru single atoms anchored to N-doped porous carbon for electrocatalysis. Isolated Ru sites with pre-adsorbed interfacial oxygen, which are adsorbed on cobalt–iron bimetallic alloys encapsulated by graphitic carbon, efficiently stabilize OOH* intermediates. The lowering of such OOH* energy barriers, which constitute the rate-determining step of OER in batteries comprised of such catalysts, boosts the intrinsic activity of such batteries. Further, Ni SACs on N-doped carbon supports facilitate NO oxidation, accomplishing real-time NO sensing in live cellular environments. In addition, Pt SACs stabilized on controllable 1D carbon nitride/SnO₂ substrates trap single atoms at the heterojunctions of such nano-heterostructure supports. Further, Pt SACs designed for ZABs can be stabilized in alloyed PtCo nanosheets with trapped interstitial F, inducing lattice distortions in supportive PtCoF matrices that weaken Pt–Co bonds and resultantly drive Pt atomization. Therefore, structural confinement and defect engineering during synthesis, which induce metastable states beyond stable bonding between SACs and supports, can impact catalytic activity and enable otherwise unfavorable structural formation.

Based on recent literature, the combination of theoretical and experimental investigations studying SACs will demonstrably provide breakthrough research on future energy technologies. Through computational studies, new fundamental insights have been explored in greater detail to determine the atomic origins of catalytic property differences. Further, the most favorable configurations of SAC-support systems, and the reaction mechanisms connecting them are validated more accurately by understanding the related atomic origins of reaction mechanisms, providing perspective on which attributes of atomic structure, bonding character, and composition are most

responsible for engineering catalytic properties. This review aspires to first construct such a fundamental atomistic theoretical framework, so as to elucidate results from subsequently evaluated SAC experimental studies and highlight the common attributes engineering SAC properties across broad ranges of energy applications. Almost all metal based composition types can be applied as SACs, though the benchmark for recent advances in SAC based research is saliently determined by SAC-support interactions. In conjunction with controlling composition, tailored well-ordered nanostructures are thus responsible for engineering catalytic properties. For this reason, how advanced characterization technologies are used to optimize SACs and validate their simulated atomic scale structures is explored in this review. Such characterization not only inextricably connects experimental and theoretical methodologies in recent studies, but also ensures this connection is maintained throughout the current review and during future research investigating SAC property engineering. Relative to practical catalytic applications, the stability and durability of recent SAC-support nanostructures has incrementally increased over time, implying the perpetually improving usefulness of such SAC systems in future energy technologies. Given all previous considerations, the research direction most apparently capable of propagating SAC implementation in such industrial applications not only sustains attention to aforementioned atomistic theoretical models and larger scale morphologies, but also fosters multiscale simulation and related characterization studies bridging gaps between current experimental and computational approaches. Theories, methodologies, and results capable of comprehensively reconciling atomistic theories with large-scale catalytic SAC implementations provide the most promising avenues for prominent developments in upcoming electrochemistry research.

Overall, this review assesses how SACs are synthesized, what structures are developed during such syntheses, the properties such structures enhance or tune, and the applications to which such properties are optimized. Over studied cases, idiosyncratic SAC advantages are responsible for overall strong catalytic performance, attracting both the focus of scientific communities and large-scale commercial applications in fuel cells and batteries. Various metal SACs were demonstrably synthesized for breakthroughs encompassing electrocatalysis and energy technologies. With continued research efforts, SACs will be able to guide future initiatives towards rationally designing effective, functional, and stable electrode materials based on atomic scale information, developing materials that could initiate breakthroughs in future renewable energy technologies.

7.2. Challenge and Future Work

SACs are currently gaining more widespread attention due to the demand to maximize the metal utilization of catalysts with better stability, as well as the aspiration to create well-defined and uniform active sites with superior catalytic performance for multipurpose potential applications. Despite advantageous developments progressing SAC usage in catalytic applications, several persistent issues involving SACs require focus to overcome in the near future. SAC aggregation is still a significant

problem during electrocatalysis due to high SAC surface free energy, which greatly influences available catalytic reaction mechanisms and catalytic performance. Although current research on SACs has reported high metal loadings, synthesizing SACs with high metal loadings in all nanostructures is still challenging. SACs with low metal loadings suffer from low exposure of their available active sites, restricting their potential applications greatly. Additionally, SACs serving as oxygen reduction catalysts face imposing long-term stability and activity difficulties in acidic media, strongly reducing their potential use in PEMFCs. To overcome these issues, more research is required, as designing appropriate metal precursors and substrates that aide in understanding the strong interactions between active metal centers and supports under practical conditions is still challenging. Further, choosing ideal single-site materials and supports is crucial to tuning the coordination environments of SAC metal centers to achieve superior catalytic activity and durability. Synthesizing effective SAC nanostructures through procedural strategies is a challenging task, given the need to properly explore the modulation of supports required to engineer vacancies and structural defects. In addition, M–N₄ and M–N₂ SAC configurations are considered highly active and favorable structures relative to many M–N coordination environments. Nevertheless, future exploration of even more suitable and effective structural configurations through theoretical simulations and experimental investigations is highly useful, as resulting discoveries can inform the engineering of reaction mechanisms and the relationships between structures and properties. Further, the effects of heteroatom doping in support materials should be monitored to explore their significant impacts towards enhancing catalytic activity and stability. In addition, HAADF-STEM and XAS studies are effective techniques for recent advanced characterization of real active sites. Nevertheless, these techniques have some limitations; they are incapable of discerning dynamical changes – such as changes of structures and components – of active sites during electrocatalysis. Also, they are unable to provide deeper insights into complicated catalytic mechanisms on SACs to some extent. In this regard, the implementation of more advanced *in situ* and *operando* characterization techniques (TEM, XRD, FTIR, and XAS) should be better established. Such methods are very impactful and informative for deeply analyzing the structural details of active sites and the dynamical processes constituting electrocatalytic reactions, all of which can directly contribute to understanding process–structure–property relationships. Although, these advanced *in situ* and *operando* methodologies are still in inchoate stages of development, urging their rapid improvement for assessing electrocatalytic reactions under practical experimental conditions.

Chemical environments encompassing metal active sites are only incompletely described by experimental techniques such as XANES, XPS, and FTIR, as the determination of nanocatalyst atomic charges in experiments is currently difficult. Therefore, Bader charge analysis is performed within a DFT framework to resolve atomic charges. Though helpful in elucidating some trends with catalytically relevant *d*-band properties and adsorption energies, metal site Bader charges typically only observe strong correlations within well-defined material sets, as SACs promote activity through the synergistic interaction

of their metal sites and supports. Rather, a more comprehensive consideration of dynamical structural changes, electron orbital theory, and previously described properties is needed to predictively characterize SAC activity. Such synergistic interaction is particularly effectively exemplified by the coupling of partial carbon support graphitization around Co-N-PCNF metal centers with increases in charge transfer and ORR catalytic activity. Further, the trade-off between metal-adsorbate, metal-support, and related bonding strengths is represented in corresponding optimization of adsorption energetics, charge transfer, and related properties. The balance between these bonding strengths simultaneously regulates the atomic dispersions, activities, and bond charge transfer events of the ligand complexes constituting SACs. Therefore, methodologies satisfying the challenge of developing effective SACs enable high densities of uniform active centers – which do not interact with one another – to form, yield active centers that stably anchor to supports over long-term applications, and promote timely adsorption and desorption of catalytic intermediates during reactions. Ultimately, this pursuit of reducing effective catalyst sizes to stable single atom layers will be describable via a more generalized application of Sabatier's principle. This application would not only balance the reaction intermediate bonding strengths observed in volcano plots, but also simultaneously the relative bond strengths of active centers to proximal support ligands and the corresponding binding strengths of proximal ligands to broader support hierarchical networks.

Acknowledgements

K.M. and S.M. contributed equally to this work. The authors acknowledge the financial support from the National Research Foundation of Korea (NRF) funded by Ministry of Science and ICT (MSIT) (NRF-2019M3D1A1079303, NRF-2016R1A5A1009592, and NRF-2021R1A2C3004019).

Conflict of Interest

The authors declare no conflict of interest.

Keywords

atomic coordination, electronic structure, evolution reactions, Li-batteries, morphological aspects, reduction reactions, single atom catalysts

Received: May 29, 2021

Revised: August 3, 2021

Published online: August 28, 2021

- [1] Q. Wang, Y. Yang, F. Sun, G. Chen, J. Wang, L. Peng, W.-T. Chen, L. Shang, J. Zhao, D. Sun-Waterhouse, T. Zhang, G. I. N. Waterhouse, *Adv. Energy Mater.* **2021**, *11*, 2100219.
- [2] Q. Zhai, Y. Liu, R. Wang, Y. Wang, Q. Lyu, S. Gong, J. Wang, G. P. Simon, W. Cheng, *Adv. Energy Mater.* **2020**, *10*, 1903512.
- [3] J. Liang, Z. Zhao, N. Li, X. Wang, S. Li, X. Liu, T. Wang, G. Lu, D. Wang, B.-J. Hwang, Y. Huang, D. Su, Q. Li, *Adv. Energy Mater.* **2020**, *10*, 2000179.

- [4] P. Wang, Y. Ren, R. Wang, P. Zhang, M. Ding, C. Li, D. Zhao, Z. Qian, Z. Zhang, L. Zhang, L. Yin, *Nat. C* **2020**, *11*, 1576.
- [5] T. Liu, L. Yu, J. Liu, J. Lu, X. Bi, A. Dai, M. Li, M. Li, Z. Hu, L. Ma, D. Luo, J. Zheng, T. Wu, Y. Ren, J. Wen, F. Pan, K. Amine, *Nat. Energy* **2021**, *6*, 277.
- [6] K. Maiti, J. Balamurugan, J. Gautam, N. H. Kim, J. H. Lee, *ACS Appl. Mater. Interfaces* **2018**, *10*, 32220.
- [7] B. Dunn, H. Kamath, J.-M. Tarascon, *Science* **2011**, *334*, 928.
- [8] X. Zeng, M. Li, D. A. El-Hady, W. Alshitarai, A. S. Al-Bogami, J. Lu, K. Amine, *Adv. Energy Mater.* **2019**, *9*, 1900161.
- [9] T. M. Gur, *Energy Environ. Sci.* **2018**, *11*, 2696.
- [10] C. Wang, K. Wang, Y. Feng, C. Li, X. Zhou, L. Gan, Y. Feng, H. Zhou, B. Zhang, X. Qu, H. Li, J. Li, A. Li, Y. Sun, S. Zhang, G. Yang, Y. Guo, S. Yang, T. Zhou, F. Dong, K. Zheng, L. Wang, J. Huang, Z. Zhang, X. Han, *Adv. Mater.* **2021**, *13*, 2003327.
- [11] K. Maiti, K. Kim, K.-J. Noh, J. W. Han, *Chem. Eng. J.* **2021**, *423*, 130233.
- [12] Z.-P. Wu, D. T. Caracciolo, Y. Maswadeh, J. Wen, Z. Kong, S. Shan, J. A. Vargas, S. Yan, E. Hopkins, K. Park, A. Sharma, Y. Ren, V. Petkov, L. Wang, C.-J. Zhong, *Nat. Comm.* **2021**, *12*, 859.
- [13] K. Kodama, T. Nagai, A. Kuwaki, R. Jinnouchi, Y. Morimoto, *Nat. Nanotech.* **2021**, *16*, 140.
- [14] S. T. Thompson, D. Papageorgopoulos, *Nat. Catal.* **2019**, *2*, 558.
- [15] X. X. Wang, M. T. Swihart, G. Wu, *Nat. Catal.* **2019**, *2*, 578.
- [16] Z. P. Cano, D. Banham, S. Ye, A. Hintennach, J. Lu, M. Fowler, Z. Chen, *Nat. Energy* **2018**, *3*, 279.
- [17] W. Li, E. M. Erickson, A. Manthiram, *Nat. Energy* **2020**, *5*, 26.
- [18] H. J. Kim, D. Shin, H. Jeong, M. G. Jang, H. Lee, J. W. Han, *ACS Catal.* **2020**, *10*, 14877.
- [19] K. Kim, B. Koo, Y.-R. Jo, S. Lee, J. K. Kim, B.-J. Kim, W. C. Jung, J. W. Han, *Energy Environ. Sci.* **2020**, *13*, 3404.
- [20] K. Kim, S. Joo, R. Huang, H. J. Kim, G. Kim, J. W. Han, *Energy Environ. Sci.* **2021**, *14*, 873.
- [21] C. Liu, W. Zhou, J. Zhang, Z. Chen, S. Liu, Y. Zhang, J. Yang, L. Xu, W. Hu, Y. Chen, Y. Deng, *Adv. Energy Mater.* **2020**, *10*, 2001397.
- [22] D. A. Cullen, K. C. Neyerlin, R. K. Ahluwalia, R. Mukundan, K. L. More, R. L. Borup, A. Z. Weber, D. J. Myers, A. Kusoglu, *Nat. Energy* **2021**, *6*, 462.
- [23] N.-Y. Park, H.-H. Ryu, G.-T. Park, T.-C. Noh, Y.-K. Sun, *Adv. Energy Mater.* **2021**, *11*, 2003767.
- [24] J. Liu, J. Bak, J. Roh, K.-S. Lee, A. Cho, J. W. Han, E. A. Cho, *ACS Catal.* **2021**, *11*, 466.
- [25] H. Jeong, G. Lee, B.-S. Kim, J. Bae, J. W. Han, H. Lee, *J. Am. Chem. Soc.* **2018**, *140*, 9558.
- [26] Y. Mun, S. Lee, K. Kim, S. Kim, S. Lee, J. W. Han, J. Lee, *J. Am. Chem. Soc.* **2019**, *141*, 6254.
- [27] H. Jeong, D. Shin, B.-S. Kim, J. Bae, S. Shin, C. Choe, J. W. Han, H. Lee, *Angew. Chem., Int. Ed.* **2020**, *59*, 20691.
- [28] X. Han, T. Zhang, W. Chen, B. Dong, G. Meng, L. Zheng, C. Yang, X. Sun, Z. Zhuang, D. Wang, A. Han, J. Liu, *Adv. Energy Mater.* **2021**, *11*, 2002753.
- [29] J. Kim, C.-W. Roh, S. K. Sahoo, S. Yang, J. Bae, J. W. Han, H. Lee, *Adv. Energy Mater.* **2018**, *8*, 1701476.
- [30] J. Yang, W. Li, D. Wang, Y. Li, *Adv. Mater.* **2020**, *32*, 2003300.
- [31] T. Zhang, Z. Chen, A. G. Walsh, Y. Li, P. Zhang, *Adv. Mater.* **2020**, *32*, 2002910.
- [32] A. M. Harzandi, S. Shadman, A. S. Nissimagoudar, D. Y. Kim, H.-D. Lim, J. H. Lee, M. G. Kim, H. Y. Jeong, Y. Kim, K. S. Kim, *Adv. Energy Mater.* **2021**, *11*, 2003448.
- [33] F.-F. Zhang, C.-Q. Cheng, J.-Q. Wang, L. Shang, Y. Feng, Y. Zhang, J. Mao, Q.-J. Guo, Y.-M. Xie, C.-K. Dong, Y.-H. Cheng, H. Liu, X.-W. Du, *ACS Energy Lett.* **2021**, *6*, 1588.
- [34] H. Niu, Z. Zhang, X. Wang, X. Wan, C. Shao, Y. Guo, *Adv. Funct. Mater.* **2021**, *31*, 2008533.

- [35] T. W. van Deelen, C. H. Mejía, K. P. de Jong, *Nat. Catal.* **2019**, *2*, 955.
- [36] K. Maiti, N. H. Kim, J. H. Lee, *Chem. Eng. J.* **2021**, *410*, 128358.
- [37] L. Peng, L. Shang, T. Zhang, G. I. N. Waterhouse, *Adv. Energy Mater.* **2020**, *10*, 2003018.
- [38] Y. Wang, J.-L. Li, W.-X. Shi, Z.-M. Zhang, G. S. , R. Si, M. Liu, H.-C. Zhou, S. Yao, C.-H. An, T.-B. Lu, *Adv. Energy Mater.* **2020**, *10*, 2002138.
- [39] S. Mitchell, J. P. Ramírez, *Nat. Commun.* **2020**, *11*, 4302.
- [40] Y. Li, B. Li, D. Zhang, L. Cheng, Q. Xiang, *ACS Nano* **2020**, *14*, 10552.
- [41] F. Wu, C. Pan, C.-T. He, Y. Han, W. Ma, H. Wei, W. Ji, W. Chen, J. Mao, P. Yu, D. Wang, L. Mao, Y. Li, *J. Am. Chem. Soc.* **2020**, *142*, 16861.
- [42] X. Li, W. Bi, L. Zhang, S. Tao, W. Chu, Q. Zhang, Y. Luo, C. Wu, Y. Xie, *Adv. Mater.* **2016**, *28*, 2427.
- [43] J. Lin, A. Wang, B. Qiao, X. Liu, X. Yang, X. Wang, J. Liang, J. Li, J. Liu, T. Zhang, *J. Am. Chem. Soc.* **2013**, *135*, 15314.
- [44] Y. Pan, S. Liu, K. Sun, X. Chen, B. Wang, K. Wu, X. Cao, W. C. Cheong, R. Shen, A. Han, *Angew. Chem., Int. Ed.* **2018**, *57*, 8614.
- [45] L. Yang, L. Shi, D. Wang, Y. Lv, D. Cao, *Nano Energy* **2018**, *50*, 691.
- [46] A. Manthiram, Y. Fu, Y.-S. Su, *Acc. Chem. Res.* **2012**, *46*, 1125.
- [47] C.-Y. Liu, S. Zhang, D. Martinez, M. Li, T. P. Senftle, *npj Comput. Mater.* **2020**, *6*, 102.
- [48] Y. Chen, S. Ji, S. Zhao, W. Chen, J. Dong, W.-C. Cheong, R. Shen, X. Wen, L. Zheng, A. I. Rykov, S. Cai, H. Tang, Z. Zhuang, C. Chen, Q. Peng, D. Wang, Y. Li, *Nat. Comm.* **2018**, *9*, 5422.
- [49] C. Gao, J. Low, R. Long, T. Kong, J. Zhu, Y. Xiong, *Chem. Rev.* **2020**, *120*, 11900.
- [50] Y. Zhu, J. Sokolowski, X. Song, Y. He, Y. Mei, G. Wu, *Adv. Energy Mater.* **2019**, *10*, 1902844.
- [51] J. Hulva, M. Meier, R. Bliem, Z. Jakub, F. Kraushofer, M. Schmid, U. Diebold, C. Franchini, G. S. Parkinson, *Science* **2021**, *371*, 375.
- [52] B. Hammer, Y. Morikawa, J. K. Norskov, *Phys. Rev. Lett.* **1996**, *76*, 2141.
- [53] K. Ding, A. Gulec, A. M. Johnson, N. M. Schweitzer, G. D. Stucky, L. D. Marks, P. C. Stair, *Science* **2015**, *350*, 189.
- [54] H. Zhang, G. Liu, L. Shi, J. Ye, *Adv. Energy Mater.* **2018**, *8*, 1701343.
- [55] F. Luo, A. Roy, L. Silvioli, D. A. Cullen, A. Zitolo, M. T. Sougrati, I. C. Oguz, T. Mineva, D. Teschner, S. Wagner, J. Wen, F. Dionigi, U. I. Kramm, J. Rossmeisl, F. Jaouen, P. Strasser, *Nat. Mater.* **2020**, *19*, 1215.
- [56] Q. Liu, Y. Li, L. Zheng, J. Shang, X. Liu, R. Yu, J. Shui, *Adv. Energy Mater.* **2020**, *10*, 2000689.
- [57] J. Ban, X. Wen, H. Xu, Z. Wang, X. Liu, G. Cao, G. Shao, J. Hu, *Adv. Funct. Mater.* **2021**, *31*, 2010472.
- [58] H. Zhang, Y. Liu, T. Chen, J. Zhang, J. Zhang, X. W. (David) Lou, *Adv. Mater.* **2019**, *31*, 1904548.
- [59] Q. He, D. Tian, H. Jiang, D. Cao, S. Wei, D. Liu, P. Song, Y. Lin, L. Song, *Adv. Mater.* **2020**, *32*, 1906972.
- [60] X. Wang, Y. Zhang, H. Si, Q. Zhang, J. Wu, L. Gao, X. Wei, Y. Sun, Q. Liao, Z. Zhang, K. Ammarah, L. Gu, Z. Kang, Y. Zhang, *J. Am. Chem. Soc.* **2020**, *142*, 4298.
- [61] L. Han, S. Song, M. Liu, S. Yao, Z. Liang, H. Cheng, Z. Ren, W. Liu, R. Lin, G. Qi, X. Liu, Q. Wu, J. Luo, H. L. Xin, *J. Am. Chem. Soc.* **2020**, *142*, 12563.
- [62] N. Zhang, X. Zhang, L. Tao, P. Jiang, C. Ye, R. Lin, Z. Huang, A. Li, D. Pang, H. Yan, Y. Wang, P. Xu, S. An, Q. Zhang, L. Liu, S. Du, X. Han, D. Wang, Y. Li, *Angew. Chem., Int. Ed.* **2021**, *60*, 6170.
- [63] X. Liu, Y. Jiao, Y. Zheng, M. Jaroniec, S.-Z. Qiao, *J. Am. Chem. Soc.* **2019**, *141*, 9664.
- [64] D. Jiao, Y. Liu, Q. Cai, J. Zhao, *J. Mater. Chem. A* **2021**, *9*, 1240.
- [65] Y. Yao, Z. Huang, P. Xie, L. Wu, L. Ma, T. Li, Z. Pang, M. Jiao, Z. Liang, J. Gao, Y. He, D. J. Kline, M. R. Zachariah, C. Wang, J. Lu, T. Wu, T. Li, C. Wang, R. Shahbazian-Yassar, L. Hu, *Nat. Nanotechnol.* **2019**, *14*, 851.
- [66] S. Ding, H.-A. Chen, O. Mekasuwandumrong, M. J. Hulse, X. Fu, Q. He, J. Panpranot, C.-M. Yang, N. Yan, *Appl. Catal. B: Environ.* **2021**, *281*, 119471.
- [67] Y. Zhao, H. Zhou, X. Zhu, Y. Qu, C. Xiong, Z. Xue, Q. Zhang, X. Liu, F. Zhou, X. Mou, W. Wang, M. Chen, Y. Xiong, X. Lin, Y. Lin, W. Chen, H.-J. Wang, Z. Jiang, L. Zheng, T. Yao, J. Dong, S. Wei, W. Huang, L. Gu, J. Luo, Y. Li, Y. Wu, *Nat. Catal.* **2021**, *4*, 134.
- [68] S. A. Akhade, J. R. Kitchin, *J. Chem. Phys.* **2012**, *137*, 084703.
- [69] S. Chrétien, H. Metiu, *Catal. Lett.* **2006**, *107*, 143.
- [70] G. S. Pala, H. Metiu, *J. Phys. Chem. C* **2007**, *111*, 8617.
- [71] H. Cui, Z. Liu, P. Jia, *Appl. Surf. Sci.* **2021**, *537*, 147881.
- [72] A. Wang, J. Li, T. Zhang, *Nat. Rev. Chem.* **2018**, *2*, 65.
- [73] J. Liu, *ACS Catal.* **2016**, *7*, 34.
- [74] X. Cui, W. Li, P. Ryabchuk, K. Junge, M. Beller, *Nat. Catal.* **2018**, *1*, 385.
- [75] B. C. Gates, M. Flytzani-Stephanopoulos, D. A. Dixon, A. Katz, *Catal. Sci. Technol.* **2017**, *7*, 4259.
- [76] G. S. Parkinson, Z. Novotny, G. Argentero, M. Schmid, J. Pavalec, R. Kosak, P. Blaha, U. Diebold, *Nat. Mater.* **2013**, *12*, 724.
- [77] A. Stroppa, G. Kresse, *New J. Phys.* **2008**, *10*, 063020.
- [78] M. T. M. Koper, R. A. van Santen, S. A. Wasileski, M. J. Weaver, *J. Chem. Phys.* **2000**, *113*, 4392.
- [79] Z. Jakub, J. Hulva, F. Mirabella, F. Kraushofer, M. Meier, R. Bliem, U. Diebold, G. S. Parkinson, *J. Phys. Chem. C* **2019**, *123*, 15038.
- [80] G. Pacchioni, C. Di Valentín, D. Dominguez-Ariza, F. Illas, T. Bredow, T. Klüner, V. Staemmler, *J. Phys. Condens. Matter* **2004**, *16*, S2497.
- [81] Z. Jakub, J. Hulva, M. Meier, R. Bliem, F. Kraushofer, M. Setvin, M. Schmid, U. Diebold, C. Franchini, G. S. Parkinson, *Angew. Chem., Int. Ed.* **2019**, *58*, 13961.
- [82] M. T. Curnan, C. M. Andolina, M. Li, Q. Zhu, H. Chi, W. A. Saidi, J. C. Yang, *J. Phys. Chem. C* **2019**, *123*, 452.
- [83] H. Chi, M. T. Curnan, M. Li, C. M. Andolina, W. A. Saidi, G. Veser, J. C. Yang, *Phys. Chem. Chem. Phys.* **2020**, *22*, 2738.
- [84] F. Li, Y. Li, X. C. Zeng, Z. Chen, *ACS Catal.* **2014**, *5*, 544.
- [85] W. Zhong, Y. Qiu, H. Shen, X. Wang, J. Yuan, C. Jia, S. Bi, J. Jiang, *J. Am. Chem. Soc.* **2021**, *143*, 4405.
- [86] Z. Fu, B. Yang, R. Wu, *Phys. Rev. Lett.* **2020**, *125*, 156001.
- [87] A. A. Mostofi, J. R. Yates, Y.-S. Lee, I. Souza, D. Vanderbilt, N. Marzari, *Comput. Phys. Commun.* **2008**, *178*, 685.
- [88] X. Zhao, Y. Liu, *J. Am. Chem. Soc.* **2020**, *142*, 5773.
- [89] G. Gan, X. Li, L. Wang, S. Fan, J. Mu, P. Wang, G. Chen, *ACS Nano* **2020**, *14*, 9929.
- [90] S. Li, C. Cheng, H. W. Liang, X. Feng, A. Thomas, *Adv. Mater.* **2017**, *29*, 1700707.
- [91] S. Li, C. Cheng, X. J. Zhao, J. Schmidt, A. Thomas, *Angew. Chem., Int. Ed.* **2018**, *57*, 1856.
- [92] X. Gong, J. Zhu, J. Li, R. Gao, Q. Zhou, Z. Zhang, H. Dou, L. Zhao, X. Sui, J. Cai, Y. Zhang, B. Liu, Y. Hu, A. Yu, S.-h. Sun, Z. Wang, Z. Chen, *Adv. Funct. Mater.* **2021**, *31*, 2008085.
- [93] A. Dhakshinamoorthy, M. Alvaro, H. Chevreau, P. Horcajada, T. Devic, C. Serre, H. Garcia, *Catal. Sci. Technol.* **2012**, *2*, 324.
- [94] S. Choi, W. Cha, H. Ji, W. Kim, H. J. Lee, M. Oh, *Nanoscale* **2016**, *8*, 16743.
- [95] P. Horcajada, F. Salles, S. Wuttke, T. Devic, D. Heurtaux, G. Maurin, A. Vimont, M. Daturi, O. David, E. Magnier, N. Stock, Y. Filinchuk, D. Popov, C. Riekel, G. Ferey, C. Serre, *J. Am. Chem. Soc.* **2011**, *133*, 17839.
- [96] G. Chen, P. Liu, Z. Liao, F. Sun, Y. He, H. Zhong, T. Zhang, E. Zschech, M. Chen, G. Wu, J. Zhang, X. Feng, *Adv. Mater.* **2020**, *32*, 1907399.
- [97] Y. Pan, S. Liu, K. Sun, X. Chen, B. Wang, K. Wu, X. Cao, W.-C. Cheong, R. Shen, A. Han, Z. Chen, L. Zheng, J. Luo, Y. Lin,

- Y. Liu, D. Wang, Q. Peng, Q. Zhang, C. Chen, Y. Li, *Angew. Chem., Int. Ed.* **2018**, *57*, 8614.
- [98] Y. Zhou, X. Tao, G. Chen, R. Lu, D. Wang, M.-X. Chen, E. Jin, J. Yang, H.-W. Liang, Y. Zhao, X. Feng, A. Narita, K. Müllen, *Nat. Comm.* **2020**, *11*, 5892.
- [99] S. Liu, F. Wang, R. Dong, T. Zhang, J. Zhang, Z. Zheng, Y. Mai, X. Feng, *Small* **2017**, *13*, 1604099.
- [100] S. Liu, P. Gordiichuk, Z.-S. Wu, Z. Liu, W. Wei, M. Wagner, N. Mohamed-Noriega, D. Wu, Y. Mai, A. Herrmann, K. Mullen, X. Feng, *Nat. Commun.* **2015**, *6*, 8817.
- [101] J. Chen, H. Li, C. Fan, Q. Meng, Y. Tang, X. Qiu, G. Fu, T. Ma, *Adv. Mater.* **2020**, *32*, 2003134.
- [102] M. Zhou, Y. Jiang, G. Wang, W. Wu, W. Chen, P. Yu, Y. Lin, J. Mao, L. Mao, *Nat. Commun.* **2020**, *11*, 3188.
- [103] Z. Zhang, X. Zhao, S. Xi, L. Zhang, Z. Chen, Z. Zeng, M. Huang, H. Yang, B. Liu, S. J. Pennycook, P. Chen, *Adv. Energy Mater.* **2020**, *10*, 2002896.
- [104] Y. Xue, B. Huang, Y. Yi, Y. Guo, Z. Zuo, Y. Li, Z. Jia, H. Liu, Y. Li, *Nat. Commun.* **2018**, *9*, 1460.
- [105] Y. He, H. Guo, S. Hwang, X. Yang, Z. He, J. Braaten, S. Karakalos, W. Shan, M. Wang, H. Zhou, Z. Feng, K. L. More, G. Wang, D. Su, D. A. Cullen, L. Fei, S. Litster, G. Wu, *Adv. Mater.* **2020**, *32*, 2003577.
- [106] J. Yin, J. Jin, M. Lu, B. Huang, H. Zhang, Y. Peng, P. Xi, C.-H. Yan, *J. Am. Chem. Soc.* **2020**, *142*, 18378.
- [107] J. Bao, X. Zhang, B. Fan, J. Zhang, M. Zhou, W. Yang, X. Hu, H. Wang, B. Pan, Y. Xie, *Angew. Chem., Int. Ed.* **2015**, *54*, 7399.
- [108] Z. Li, Y. Chen, S. Ji, Y. Tang, W. Chen, A. Li, J. Zhao, Y. Xiong, Y. Wu, Y. Gong, T. Yao, W. Liu, L. Zheng, J. Dong, Y. Wang, Z. Zhuang, W. Xing, C.-T. He, C. Peng, W.-C. Cheong, Q. Li, M. Zhang, Z. Chen, N. Fu, X. Gao, W. Zhu, J. Wan, J. Zhang, L. Gu, S. Wei, P. Hu, J. Luo, J. Li, C. Chen, Q. Peng, X. Duan, Y. Huang, X.-M. Chen, D. Wang, Y. Li, *Nat. Chem.* **2020**, *12*, 764.
- [109] D. H. Yoshida, S. Nonoyama, Y. Y. T. Hattori, *Phys. Scr.* **2005**, *2005*, 813.
- [110] Q. Wang, X. Huang, Z. L. Zhao, M. Wang, B. Xiang, J. Li, Z. Feng, H. Xu, M. Gu, *J. Am. Chem. Soc.* **2020**, *142*, 7425.
- [111] Y. Hu, G. Luo, L. Wang, X. Liu, Y. Qu, Y. Zhou, F. Zhou, Z. Li, Y. Li, T. Yao, C. Xiong, B. Yang, Z. Yu, Y. Wu, *Adv. Energy Mater.* **2021**, *11*, 2002816.
- [112] X. Hu, G. Luo, Q. Zhao, D. Wu, T. Yang, J. Wen, R. Wang, C. Xu, N. Hu, *J. Am. Chem. Soc.* **2020**, *142*, 16776.
- [113] J. Lee, A. Kumar, T. Yang, X. Liu, A. R. Jadhav, G. Hwan Park, Y. Hwang, J. Yu, C. T. K. Nguyen, Y. Liu, S. Ajmal, M. G. Kim, H. Lee, *Energy Environ. Sci.* **2020**, *13*, 5152.
- [114] J. Yang, D. Zeng, Q. Zhang, R. Cui, M. Hassan, L. Dong, J. Li, Y. He, *Appl. Catal. B Environ.* **2020**, *279*, 119363.
- [115] H. Shin, W.-G. Jung, D.-H. Kim, J.-S. Jang, Y. H. Kim, W.-T. Koo, J. Bae, C. Park, S.-H. Cho, B. J. Kim, I.-D. Kim, *ACS Nano* **2020**, *14*, 11394.
- [116] J. Y. Kang, J. Jang, W. Koo, J. Seo, Y. Choi, M. Kim, D. Kim, H. Cho, W. Jung, I. Kim, *J. Mater. Chem. A* **2018**, *6*, 10543.
- [117] R. H. Kim, J. S. Jang, D. H. Kim, J. Y. Kang, H. J. Cho, Y. J. Jeong, I. D. Kim, *Adv. Funct. Mater.* **2019**, *29*, 1903128.
- [118] S. J. Kim, S. J. Choi, J. S. Jang, H. J. Cho, W. T. Koo, H. L. Tuller, I. D. Kim, *Adv. Mater.* **2017**, *29*, 1700737.
- [119] Z. Li, W. Niu, Z. Yang, N. Zaman, W. Samarakoon, M. Wang, A. Kara, M. Lucero, M. V. Vyas, H. Cao, H. Zhou, G. E. Sterbinsky, Z. Feng, Y. Du, Y. Yang, *Energy Environ. Sci.* **2020**, *13*, 884.
- [120] H. Zhou, F. Yu, Q. Zhu, J. Sun, F. Qin, L. Yu, J. Bao, Y. Yu, S. Chen, Z. Ren, *Energy Environ. Sci.* **2018**, *11*, 2858.
- [121] Z. Kou, W. Zang, W. Pei, L. Zheng, S. Zhou, S. Zhang, L. Zhang, J. Wang, *J. Mater. Chem. A* **2020**, *8*, 3071.
- [122] P. Li, G. Zhao, P. Cui, N. Cheng, M. Lao, X. Xu, S. X. Dou, W. Sun, *Nano Energy* **2021**, *83*, 105850.
- [123] C. Liu, J. Qian, Y. Ye, H. Zhou, C.-J. Sun, C. Sheehan, Z. Zhang, G. Wan, Y.-S. Liu, J. Guo, S. Li, H. Shin, S. Hwang, T. B. Gurnoe, W. A. Goddard III, S. Zhang, *Nat. Catal.* **2021**, *4*, 36.
- [124] P. Zhou, Q. Zhang, Y. Chao, L. Wang, Y. Li, H. Chen, L. Gu, S. Guo, *Chem* **2021**, *7*, 1033.
- [125] H. Yang, X. Zhang, Y. Yu, Z. Chen, Q. Liu, Y. Li, W.-C. Cheong, D. Qi, Z. Zhuang, Q. Peng, X. Chen, H. Xiao, C. Chen, Y. Li, *Chem. Sci.* **2021**, *12*, 6099.
- [126] A. M. Abdel-Mageed, B. Rungtaweevoranit, M. Parlinska-Wojtan, X. Pei, O. M. Yaghi, R. Jürgen Behm, *J. Am. Chem. Soc.* **2019**, *141*, 5201.
- [127] Y. Zuo, T. Li, N. Zhang, T. Jing, D. Rao, P. Schmuki, Š. Kment, R. Zbořil, Y. Chai, *ACS Nano* **2021**, *15*, 7790.
- [128] P. Chen, B. Lei, X. Dong, H. Wang, J. Sheng, W. Cui, J. Li, Y. Sun, Z. Wang, F. Dong, *ACS Nano* **2020**, *14*, 15841.
- [129] J. Liu, X. Kong, L. Zheng, X. Guo, X. Liu, J. Shui, *ACS Nano* **2020**, *14*, 1093.
- [130] D. H. Pearson, C. C. Ahn, B. Fultz, *Phys. Rev. B: Condens. Matter Mater. Phys.* **1993**, *47*, 8471.
- [131] J. R. Hayes, A. P. Grosvenor, M. Saoudi, *Inorg. Chem.* **2016**, *55*, 1032.
- [132] F. Li, Y. Bu, G. F. Han, H. J. Noh, S. J. Kim, I. Ahmad, Y. Lu, P. Zhang, H. Y. Jeong, Z. Fu, Q. Zhong, J. B. Baek, *Nat. Commun.* **2019**, *10*, 1.
- [133] X. Zeng, J. Shui, X. Liu, Q. Liu, Y. Li, J. Shang, L. Zheng, R. Yu, *Adv. Energy Mater.* **2018**, *8*, 1701345.
- [134] Y. Han, Y. G. Wang, W. Chen, R. Xu, L. Zheng, J. Zhang, J. Luo, R. A. Shen, Y. Zhu, W. C. Cheong, C. Chen, Q. Peng, D. Wang, Y. Li, *J. Am. Chem. Soc.* **2017**, *139*, 17269.
- [135] J. Wang, X. Huang, S. Xi, J. M. Lee, C. Wang, Y. Du, X. Wang, *Angew. Chem., Int. Ed.* **2019**, *58*, 13532.
- [136] P. Wang, Y. Ren, R. Wang, P. Zhang, M. Ding, C. Li, D. Zhao, Z. Qian, Z. Zhang, L. Zhang, L. Yin, *Nat. Commun.* **2020**, *11*, 1576.
- [137] T. Liu, L. Zhang, B. Cheng, J. Yu, *Adv. Energy Mater.* **2019**, *9*, 1803900.
- [138] R. Gao, D. Yan, *Adv. Energy Mater.* **2020**, *10*, 1900954.
- [139] H. Zhang, W. Zhou, X. F. Lu, T. Chen, X. W. (David) Lou, *Adv. Energy Mater.* **2020**, *10*, 2000882.
- [140] J. Greeley, T. F. Jaramillo, J. Bonde, I. Chorkendorff, J. K. Nørskov, *Nat. Mater.* **2006**, *5*, 909.
- [141] J. Wang, Z. Wei, S. Mao, H. Li, Y. Wang, *Energy Environ. Sci.* **2018**, *11*, 800.
- [142] W. Zang, T. Sun, T. Yang, S. Xi, M. Waqar, Z. Kou, Z. Lyu, Y. P. Feng, J. Wang, S. J. Pennycook, *Adv. Mater.* **2021**, *33*, 2003846.
- [143] C.-H. Chen, D. Wu, Z. Li, R. Zhang, C.-G. Kuai, X.-R. Zhao, C.-K. Dong, S.-Z. Qiao, H. Liu, X.-W. Du, *Adv. Energy Mater.* **2019**, *9*, 1803913.
- [144] T. Liu, P. Li, N. Yao, G. Cheng, S. Chen, W. Luo, Y. Yin, *Angew. Chem., Int. Ed.* **2019**, *58*, 4679.
- [145] H. Jiang, J. Gu, X. Zheng, M. Liu, X. Qiu, L. Wang, W. Li, Z. Chen, X. Ji, J. Li, *Energy Environ. Sci.* **2019**, *12*, 322.
- [146] J. Zhu, L. Cai, X. Yin, Z. Wang, L. Zhang, H. Ma, Y. Ke, Y. Du, S. Xi, A. T. S. Wee, Y. Chai, W. Zhang, *ACS Nano* **2020**, *14*, 5600.
- [147] X. Han, X. Wu, Y. Deng, J. Liu, J. Lu, C. Zhong, W. Hu, *Adv. Energy Mater.* **2018**, *8*, 1800935.
- [148] H. Jin, S. Sultan, M. Ha, J. N. Tiwari, M. G. Kim, K. S. Kim, *Adv. Funct. Mater.* **2020**, *30*, 2000531.
- [149] X. Liu, L. Zheng, C. Han, H. Zong, G. Yang, S. Lin, A. Kumar, A. R. Jadhav, N. Q. Tran, Y. Hwang, J. Lee, S. Vasimalla, Z. Chen, S.-G. Kim, H. Lee, *Adv. Funct. Mater.* **2021**, *31*, 2100547.
- [150] W. Chen, J. Pei, C.-T. He, J. Wan, H. Ren, Y. Wang, J. Dong, K. Wu, W.-C. Cheong, J. Mao, X. Zheng, W. Yan, Z. Zhuang, C. Chen, Q. Peng, D. Wang, Y. Li, *Adv. Mater.* **2018**, *30*, 1800396.
- [151] Y. Luo, S. Zhang, H. Pan, S. Xiao, Z. Guo, L. Tang, U. Khan, B.-F. Ding, M. Li, Z. Cai, Y. Zhao, W. Lv, Q. Feng, X. Zou, J. Lin, H.-M. Cheng, B. Liu, *ACS Nano* **2020**, *14*, 767.

- [152] S. Fang, X. Zhu, X. Liu, J. Gu, W. Liu, D. Wang, W. Zhang, Y. Lin, J. Lu, S. Wei, Y. Li, T. Yao, *Nat. Commun.* **2020**, *11*, 1029.
- [153] B. Cao, M. Hu, Y. Cheng, P. Jing, B. Liu, B. Zhou, X. Wang, R. Gao, X. Sun, Y. Du, J. Zhang, *NPG Asia Mater* **2021**, *13*, 1.
- [154] X. Xiong, C. Mao, Z. Yang, Q. Zhang, G. I. N. Waterhouse, L. Gu, T. Zhang, *Adv. Energy Mater.* **2020**, *10*, 2002928.
- [155] J. Feng, H. Gao, L. Zheng, Z. Chen, S. Zeng, C. Jiang, H. Dong, L. Liu, S. Zhang, X. Zhang, *Nat. Commun.* **2020**, *11*, 4341.
- [156] W. Ni, Z. Liu, Y. Zhang, C. Ma, H. Deng, S. Zhang, S. Wang, *Adv. Mater.* **2021**, *33*, 2003238.
- [157] Y. Jia, L. Z. Zhang, A. J. Du, G. P. Gao, J. Chen, X. C. Yan, C. L. Brown, X. D. Yao, *Adv. Mater.* **2016**, *28*, 9532.
- [158] P. Lu, X. Tan, H. Zhao, Q. Xiang, K. Liu, X. Zhao, X. Yin, X. Li, X. Hai, S. Xi, A. T. S. Wee, S. J. Pennycook, X. Yu, M. Yuan, J. Wu, G. Zhang, S. C. Smith, Z. Yin, *ACS Nano* **2021**, *15*, 5671.
- [159] X. Zu, X. Li, W. Liu, Y. Sun, J. Xu, T. Yao, W. Yan, S. Gao, C. Wang, S. Wei, Y. Xie, *Adv. Mater.* **2019**, *31*, 1808135.
- [160] H. Kim, D. Shin, W. Yang, D. H. Won, H.-S. Oh, M. W. Chung, D. Jeong, S. H. Kim, K. H. Chae, J. Y. Ryu, J. Lee, S. J. Cho, J. Seo, H. Kim, C. H. Choi, *J. Am. Chem. Soc.* **2021**, *143*, 925.
- [161] W. Zheng, J. Yang, H. Chen, Y. Hou, Q. Wang, M. Gu, F. He, Y. Xia, Z. Xia, Z. Li, B. Yang, L. L. C. Yuan, Q. He, M. Qiu, X. Feng, *Adv. Funct. Mater.* **2020**, *30*, 1907658.
- [162] F. Pan, B. Li, E. Sarnello, Y. Fei, X. Feng, Y. Gang, X. Xiang, L. Fang, T. Li, Y. H. Hu, G. Wang, Y. Li, *ACS Catal.* **2020**, *10*, 10803.
- [163] Q. Fan, P. Hou, C. Choi, T.-S. Wu, S. Hong, F. Li, Y.-L. Soo, P. Kang, Y. Jung, Z. Sun, *Adv. Energy Mater.* **2020**, *10*, 1903068.
- [164] Q. He, J. H. Lee, D. Liu, Y. Liu, Z. Lin, Z. Xie, S. Hwang, S. Kattel, L. Song, J. G. Chen, *Adv. Funct. Mater.* **2020**, *30*, 2000407.
- [165] C. Zhang, S. Yang, J. Wu, M. Liu, S. Yazdi, M. Ren, J. Sha, J. Zhong, K. Nie, A. S. Jalilov, Z. Li, H. Li, B. I. Yakobson, Q. Wu, E. Ringe, H. Xu, P. M. Ajayan, J. M. Tour, *Adv. Energy Mater.* **2018**, *8*, 1703487.
- [166] L. Cheng, H. Yin, C. Cai, J. Fan, Q. Xiang, *Small* **2020**, *16*, 2002411.
- [167] Z. Han, Y. Zhao, G. Gao, W. Zhang, Y. Qu, H. Zhu, P. Zhu, G. Wang, *Small* **2021**, *17*, 2102089.
- [168] J. Deng, J. A. Iñiguez, C. Liu, *Joule* **2018**, *2*, 846.
- [169] Y. Hao, Y. Guo, L. Chen, M. Shu, X. Wang, T.-A. Bu, W. Gao, N. Zhang, X. Su, X. Feng, J. Zhou, B. Wang, C. Hu, A. Yin, R. Si, Y. Zhang, C. Yan, *Nat. Catal.* **2019**, *2*, 448.
- [170] C. Tang, S. Qiao, *Chem. Soc. Rev.* **2019**, *48*, 3166.
- [171] W. Zang, T. Yang, H. Zou, S. Xi, H. Zhang, X. Liu, Z. Kou, Y. Du, Y. P. Feng, L. Shen, L. Duan, J. Wang, S. J. Pennycook, *ACS Catal.* **2019**, *9*, 10166.
- [172] B. Yu, H. Li, J. White, S. Donne, J. Yi, S. Xi, Y. Fu, G. Henkelman, H. Yu, Z. Chen, T. Ma, *Adv. Funct. Mater.* **2020**, *30*, 1905665.
- [173] Y. Gu, B. Xi, W. Tian, H. Zhang, Q. Fu, S. Xiong, *Adv. Mater.* **2021**, *33*, 2100429.
- [174] X. Wang, Y. Jia, X. Mao, D. Liu, W. He, J. Li, J. Liu, X. Yan, J. Chen, L. Song, A. Du, X. Yao, *Adv. Mater.* **2020**, *32*, 2000966.
- [175] F. Li, Y. Bu, G.-F. Han, H.-J. Noh, S.-J. Kim, I. Ahmad, Y. Lu, P. Zhang, H. Y. Jeong, Z. Fu, Q. Zhong, J.-B. Baek, *Nat. Commun.* **2019**, *10*, 2623.
- [176] S. Li, J. Liu, Z. Yin, P. Ren, L. Lin, Y. Gong, C. Yang, X. Zheng, R. Cao, S. Yao, Y. Deng, X. Liu, L. Gu, W. Zhou, J. Zhu, X. Wen, B. Xu, D. Ma, *ACS Catal.* **2020**, *10*, 907.
- [177] W. Wan, C. A. Triana, J. Lan, J. Li, C. S. Allen, Y. Zhao, M. Iannuzzi, G. R. Patzke, *ACS Nano* **2020**, *14*, 13279.
- [178] H. Su, W. Zhou, H. Zhang, W. Zhou, X. Zhao, Y. Li, M. Liu, W. Cheng, Q. Liu, *J. Am. Chem. Soc.* **2020**, *142*, 12306.
- [179] J. Liu, J. Bak, J. Roh, K.-S. Lee, A. Cho, J. W. Han, E. Cho, *ACS Catal.* **2021**, *11*, 466.
- [180] M. Zhu, C. Zhao, X. Liu, X. Wang, F. Zhou, J. Wang, Y. Hu, Y. Zhao, T. Yao, L.-M. Yang, Y. Wu, *ACS Catal.* **2021**, *11*, 3923.
- [181] X. Hai, X. Zhao, N. Guo, C. Yao, C. Chen, W. Liu, Y. Du, H. Yan, J. Li, Z. Chen, X. Li, Z. Li, H. Xu, P. Lyu, J. Zhang, M. Lin, C. Su, S. J. Pennycook, C. Zhang, S. Xi, J. Lu, *ACS Catal.* **2020**, *10*, 5862.
- [182] J.-C. Li, S. Maurya, Y. S. Kim, T. Li, L. Wang, Q. Shi, D. Liu, S. Feng, Y. Lin, M. Shao, *ACS Catal.* **2020**, *10*, 2452.
- [183] Z. Zhu, H. Yin, Y. Wang, C.-H. Chuang, L. Xing, M. Dong, Y.-R. Lu, G. Casillas-Garcia, Y. Zheng, S. Chen, Y. Dou, P. Liu, Q. Cheng, H. Zhao, *Adv. Mater.* **2020**, *32*, 2004670.
- [184] Z. Liu, S. Li, J. Yang, X. Tan, C. Yu, C. Zhao, X. Han, H. Huang, G. Wan, Y. Liu, K. Tschulik, J. Qiu, *ACS Nano* **2020**, *14*, 11662.
- [185] S. Kang, Y. K. Jeong, S. Mhin, J. H. Ryu, G. Ali, K. Lee, M. Akbar, K. Y. Chung, H.-S. Han, K. M. Kim, *ACS Nano* **2021**, *15*, 4416.
- [186] C. Cai, M. Wang, S. Han, Q. Wang, Q. Zhang, Y. Zhu, X. Yang, D. Wu, X. Zu, G. E. Sterbinsky, Z. Feng, M. Gu, *ACS Catal.* **2021**, *11*, 123.
- [187] W. Niu, S. Pakhira, K. Marcus, Z. Li, J. L. Mendoza-Cortes, Y. Yang, *Adv. Energy Mater.* **2018**, *8*, 1800480.
- [188] J. Pan, Y. Y. Xu, H. Yang, Z. Dong, H. Liu, B. Y. Xia, *Adv. Sci.* **2018**, *5*, 1700691.
- [189] S. S. Shinde, C. H. Lee, A. Sami, D. H. Kim, S. U. Lee, J. H. Lee, *ACS Nano* **2017**, *11*, 347.
- [190] Z. Liang, D. Yang, P. Tang, C. Zhang, J. J. Biendicho, Y. Zhang, J. Llorca, X. Wang, J. Li, M. Heggen, J. David, R. E. Dunin-Borkowski, Y. Zhou, J. R. Morante, A. Cabot, J. Arbiol, *Adv. Energy Mater.* **2021**, *11*, 2003507.
- [191] H. Yuan, H.-J. Peng, B.-Q. Li, J. Xie, L. Kong, M. Zhao, X. Chen, J.-Q. Huang, Q. Zhang, *Adv. Energy Mater.* **2019**, *9*, 1802768.
- [192] C.-Y. Fan, Y.-P. Zheng, X.-H. Zhang, Y.-H. Shi, S.-Y. Liu, H.-C. Wang, X.-L. Wu, H.-Z. Sun, J.-P. Zhang, *Adv. Energy Mater.* **2018**, *8*, 1703638.
- [193] S.-M. Xu, Q.-C. Zhu, J. Long, H.-H. Wang, X.-F. Xie, K.-X. Wang, J.-S. Chen, *Adv. Funct. Mater.* **2016**, *26*, 1365.
- [194] C. Hu, L. Gong, Y. Xiao, Y. Yuan, N. M. Bedford, Z. Xia, L. Ma, T. Wu, Y. Lin, J. W. Connell, R. Shahbazian-Yassar, J. Lu, K. Amine, L. Dai, *Adv. Mater.* **2020**, *32*, 1907436.
- [195] C. Hu, Y. Xiao, Y. Zhao, N. Chen, Z. Zhang, M. Cao, L. Qu, *Nanoscale* **2013**, *5*, 2726.
- [196] F. Qiu, S. Ren, X. Mu, Y. Liu, X. Zhang, P. He, H. Zhou, *Energy Storage Mater.* **2020**, *26*, 443.
- [197] M. H. Bai, K. Y. Xie, K. Yuan, K. Zhang, N. Li, C. Shen, Y. Q. Lai, R. Vajtai, P. Ajayan, B. Wei, *Adv. Mater.* **2018**, *30*, 1801213.
- [198] H. Jeong, S. Shin, H. Lee, *ACS Nano* **2020**, *14*, 14355.
- [199] J. P. Janet, H. J. Kulik, *J. Phys. Chem. A* **2017**, *121*, 8939.
- [200] L. Sun, V. Reddu, A. C. Fisher, X. Wang, *Energy Environ. Sci.* **2020**, *13*, 374.
- [201] C. Gao, J. Low, R. Long, T. Kong, J. Zhu, Y. Xiong, *Chem. Rev.* **2020**, *120*, 12175.



Kakali Maiti is currently working as a postdoctoral associate under the supervision of Prof. Jeong Woo Han at Chemical Engineering Department, Pohang University of Science and Technology (POSTECH), South Korea. She obtained her Ph.D. degree from Jeonbuk National University (JBNU), South Korea in 2018. Her current research interests include the design of highly durable bi-/trimetallic metal nano-architectures for fuel cell and water electrolysis applications. She is also highly experienced in synthesizing doped and undoped 2D graphene nanosheets.



Sandip Maiti is currently working as a research assistant professor at Chemical Engineering Department, Pohang University of Science and Technology (POSTECH), South Korea. He received his Ph.D. degree from Indian Institute of Technology Kharagpur (IIT KGP) in 2014, India and was a postdoctoral associate at POSTECH until 2020. His current research interests include the design of smart nanomaterials for fuel cell, water splitting and battery applications. He is also well-known in the study of piezoelectric and triboelectric nanogenerators.



Matthew T. Curnan is currently a research assistant professor at Chemical Engineering Department, Pohang University of Science and Technology (POSTECH), South Korea. Prior to working at POSTECH, he obtained undergraduate degrees in Chemical and Biomolecular Engineering and Economics at the University of Pennsylvania in 2011, as well as master's and doctoral degrees in materials science and engineering at Carnegie Mellon University in 2015. Relevant to this review, his research encompasses the computational modeling of chemical reactions and electronic structure, the engineering of defects in metal and metal oxide structures, and collaborative work reconciling experiments and simulations.



Hyung Jun Kim received his B.S. degree in chemical engineering from Hoseo University in 2017, and his M.S. degree in chemical engineering from the University of Seoul in 2019. He is currently a Ph.D. student in chemical engineering under the guidance of Prof. Jeong Woo Han at POSTECH. His current research is focused on the rational development of metal oxide catalysts.



Jeong Woo Han is currently an associate professor of Chemical Engineering at Pohang University of Science and Technology (POSTECH), South Korea and a member of the Young Korean Academy of Science and Technology. Before joining POSTECH in 2018, he was an Assistant/Associate Professor at the University of Seoul, South Korea. He obtained his Ph.D. at Georgia Tech in 2010, and was a postdoctoral associate at MIT until 2012. His current research area is the computational modeling of catalysis and energy materials, including automotive catalysis, fuel cell electrodes, liquid organic hydrogen carriers, and single atom catalysis, and so on.